PART I: EFFECTS OF PYRAMIDALIZATION AT NITROGEN IN A SERIES OF DONOR-π-ACCEPTOR DYES

PART II: EFFECTS OF VINYLTRIMETHOXYSILANE ON BONE GROWTH TEMPLATES

by

Matthew A. Robinson

A Thesis Submitted in Partial Fulfillment
of the Requirements for the Degree of
Master of Science in Chemistry

Middle Tennessee State University

2014

Thesis Committee:

Dr. Andrienne C. Friedli, Major Advisor

Dr. Norma K. Dunlap, Committee Member

Dr. Scott T. Handy, Committee Member

ACKNOWDLEGEMENTS

I would like to acknowledge several faculty members and lab mates that made the completion of this thesis possible. A sincere thank you goes to the following: Dr. Norma K. Dunlap and Dr. Scott Handy for being patient and cautious readers during the corrections process; Patrick Greco for synthesizing previous dyes; Ama Quo, Angela Gootee, and Honorio Martinez for their contributions with synthesis and characterization of dyes; Peter Haddix for fluorescence testing; Joyce Miller for her patience and instruction during SEM/TEM training; Mandy Burns and John Shires for making graduate life a little easier; Friends and family for unconditional love, support, and prayers. My final acknowledgement goes to Dr. Andrienne Friedli for her infinite amount of patience, willingness to mentor, and extreme dedication in molding students into better scientists.

ABSTRACT

PART I. EFFECTS OF PYRAMIDALIZATION AT NITROGEN IN A SERIES OF DONOR-π-ACCEPTOR DYES

PART II. EFFECTS OF VINYLTRIMETHOXYSILANE ON BONE GROWTH TEMPLATES

Matthew Robinson

Part I. Several methods have been developed to synthesize and optimize the parameters for organic materials that display nonlinear optical (NLO) properties. To determine the effect of donor group geometry on stability and conjugation in donor-π-acceptor polyenes, compounds **1-8** were synthesized and characterized. Dyes were characterized with UV/Vis, IR, HRMS, and $^{1}H/^{13}C$ NMR spectroscopy. UV and ^{1}H NMR solvatochromism (in a wide range of solvents) was correlated with the π* polarity scale and NMR coupling constants were related to bond length alternation. It was found that dyes containing a thiobarbituric acid acceptor showed better solubility, linear positive UV solvatochromism when plotted against the solvent π* polarity, and exhibited solvatochromic trends in NMR. Dyes containing a tricyanofuran acceptor had poor solubility, increased solvent sensitivity in UV studies, and limited ^{1}H NMR information due to peak overlap. Results were supported with geometry calculations using B3LYP and HF methods.

Part II. A vast amount of research has been conducted to understand the mechanisms of bone degeneration as well as methods to promote bone growth. Mesoporous silicate (m-SiO_2) foams are biocompatible, have comparable pore size to bone, and are conducive to growth of bone-forming cells, osteoblasts. However, they lack the required mechanical strength for application as regenerative scaffolds. To increase crosslinking and flexibility during the foam template coating process, vinyl trimethoxysilane (VTMS) was incorporated into the sol-gel coating. Polyurethane foams were iteratively dip-coated with sol-gel, irradiated with a 450 W UV lamp and then air-dried to give 1-12 layer materials. The foams were calcined at 600 ^{o}C in a Lindberg furnace to remove the organic component, resulting in an inorganic scaffold. The materials were analyzed using SEM images including an analysis of the effect of drying time and VTMS content on pore sizes. Statistically, the data showed minimal differences between samples containing VTMS and those without the cross-linker.

TABLE OF CONTENTS

PAGE

LIST OF FIGURES-PART I

FIGURE **PAGE**

LIST OF FIGURES-PART II

FIGURE **PAGE**

LIST OF TABLES – Part I

TABLE **PAGE**

LIST OF TABLES – Part II

TABLE **PAGE**

PART I. EFFECT OF PYRAMIDALIZATION AT NITROGEN IN A SERIES OF DONOR-π-ACCEPTOR DYES

CHAPTER I

INTRODUCTION

1.1 Nonlinear Optical Materials

Over the past several decades, several methods have been developed to synthesize and optimize the parameters for materials that display nonlinear optical (NLO) properties. NLO materials are versatile, having applications in telecommunications, optical storage, optical information processing, electro-optic modulators, optical switches, digital signal processors, and phased array radar.[1,2] Known NLO materials include inorganic materials (e.g. lithium niobate), liquid crystals, organometallic compounds, organic molecules, and polymers.[3-6] Lithium niobate is used in electro-optical devices.[7] However, the arduous process of creating pure inorganic crystals as well as the associated high cost, has led to a search for more economical options.[7] Organic materials are promising for development of future NLO materials. Organic molecules are flexible, highly cost efficient, and involve rapid synthesis, compared to inorganic crystals.

Prototypical organic molecules that exhibit NLO behavior include donor-π-acceptor (DA) compounds. Such compounds contain a donor portion, a conjugated pi bridge, and an acceptor portion (**Figure 1**). Several studies have been dedicated to determine the appropriate matching of donor/acceptor moieties, the strength of these groups, and the maximum pi bridge length for fine-tuning a promising NLO material.[8-16] Several conclusions have provided insight on the effects of molecular structure on the overall material functionality. One parameter that is utilized to understand structure-

property relationships for donor-π-acceptor polyenes or polymethine dyes is bond length alternation (BLA).

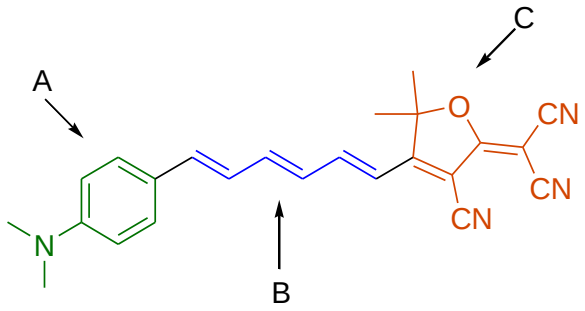

Figure 1. Illustration of Donor-π-Acceptor compound **1**. (A) Donor region (B) pi bridge (C) acceptor region.

When a reduction in BLA is observed, the molecule will shift from a bond-alternate polyene limit (single structure contributing in ground state) to a bond-equivalent cyanine limit (two contributing structures in ground state).[8] Molecules with weak donor/acceptor groups and corresponding high BLA values will result in a decreased NLO response and lead to insufficient charge transfer between the donor and acceptor groups.[8] It was found through studies with donor-acceptor substituted stilbenes and diphenyl polyenes that increased BLA levels throughout the polyene bridge contribute to incomplete separation of charge between the donor and acceptor.[8,9] This incompleteness is due to the loss of aromaticity during induced charge separation. This led to an idea to match donors/acceptors such that while one end is losing aromaticity (i.e. donor group) the opposite side (i.e. acceptor group) will counteract that loss by gaining aromaticity.[8] Ideally, donor-π-acceptor dyes should be designed so that strong donor/acceptor groups

can induce complete charge separation with corresponding low BLA values while maintaining aromaticity.[8] BLA will be discussed in further detail in **Section 1.3**.

1.2 Properties of NLO Materials

One of the first and most important requirements for an NLO material is finding a molecule with high nonlinear optical properties.[7] A specific parameter that is of great interest and consistently being improved is the first hyperpolarizability (β). Molecules that contain large β values are typically polyenes and correspond to better NLO materials. When a DA molecule is excited by light, it causes the molecule to form an induced dipole. This dipole is described by a Taylor series (**equation 1**),

$$\boldsymbol{\mu_i = \alpha_{ij}E_j + \beta_{ijk}E_jE_k + \gamma_{ijkl}E_jE_kE_l + \ldots} \qquad (\mathbf{1})$$

where μ is the induced dipole, E describes the components of the electro-magnetic field, α is the linear polarizability, β is the first hyperpolarizability, and γ is the second hyperpolarizability.[7] The β component from the above Taylor series represents second order nonlinear optical effects (e.g. frequency doubling, frequency mixing, optical rectification, electro-optic effect, etc.).[7] A challenge with this component is that it is defined as a second-order polar tensor and it disappears in a centrosymmetric environment.[7] Thus, most NLO materials are designed to ensure that the molecule is a non-centrosymmetric one-dimensional charge transfer molecule.[7] A relationship exists

between the molecular excitation (i.e. electronic charge transfer excitation) between ground state to excited state and the non-linearity of the material. When a molecule is bombarded with a photon, the incident energy induces the molecule to transition from the ground state to the excited state. This energy gap between the two states is the charge transfer band. As mentioned previously, one characteristic of β is frequency doubling (second harmonic generation). Frequency doubling occurs when incident photons interact with a nonlinear material and the products include photons with twice the frequency, twice the energy, and half the wavelength.

1.3 Bond Length Alternation

An interesting property of DA dyes is their ability to contribute different structural forms in the ground state, both neutral and charge separated. **Figure 2** illustrates a mixture of neutral and charge-separated (zwitterionic) limiting resonance forms.

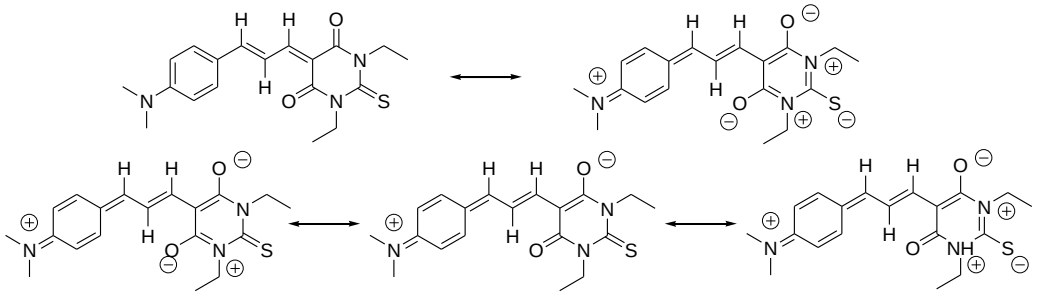

Figure 2. Illustration of neutral and charge separated form for compound **5**.

Based on semi-empirical calculations, it was determined that the hyperpolarizibility tensor component can be can be correlated to physical and electronic for ground state

calculations. As mentioned previously, one structural parameter that has been linked to understanding NLO behavior is BLA.[17] BLA is a very important structural parameter that has found to be useful in describing the electronic structure for the DA dyes as well as the ability to transfer charge across conjugated paths.[18] BLA can be determined through x-ray crystallographic data or by calculating the difference in ^{1}H NMR coupling constants (ΔJ).[1,18] The BLA is defined as the average difference between the length of adjacent carbon-carbon double bonds and carbon-carbon single bonds.[1]

A study was done on the effect of BLA on the NLO second-order coefficient β.[1] In the ground state, if the BLA values correspond to ranges between - 0.11 - 0 Å then the neutral form of the DA dye is predominant. However, when BLA values range between 0 - 0.11 Å, the charge-separated predominates. If the BLA = 0, then both forms contribute equally to the ground state. When BLA is high, then a drop in hyperpolarizability is observed, whereas when BLA = 0, the hyperpolarizability component completely cancels out of the Taylor series. At lower BLA values (BLA = 0.02-0.05 Å), a maximum is observed in hyperpolarizability. The length of the polyene chain as well as an appropriate pairing of the donor/acceptor groups plays a crucial role in maximizing hyperpolarizability. Larger polyene lengths correspond to increased hyperpolarizabilities. Yet increasing length presents difficulties with synthesis. Thus, a molecule with decreased BLA values, an appropriate conjugated bridge length, and suitable combinations of donor/acceptor groups define the necessary properties required for molecules with NLO properties.

1.4 Solvatochromism

Over the past century, the solvent medium that surrounds a molecule was demonstrated to strongly influence the UV-VIS absorptions. The solvent environment can induce a change in the position, intensity, and shape of the absorption bands.[19] These induced changes are known collectively as solvatochromism. There are two types of solvatochromism: positive and negative solvatochromism. In negative solvatochromism, a shift towards shorter wavelengths (hypsochromic shift) is observed. As the polarity of the solvent increases, the molecule or ground state is better stabilized, increasing the band gap, and the absorption band shifts to shorter wavelength values. In positive solvatochromism, a bathochromic shift is observed. As the polarity of the solvent increases, the molecule becomes more stabilized in the excited state, the band gap decreases, and the absorption band shifts to longer wavelengths (**Figure 3**).

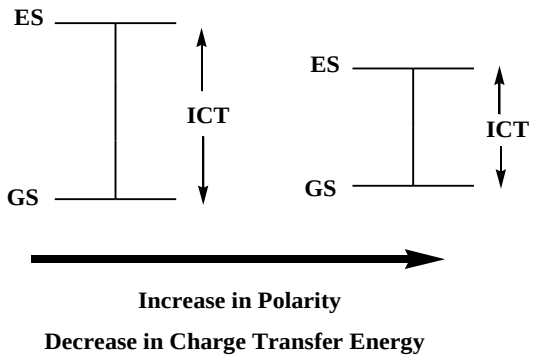

Figure 3. Illustration of positive solvatochromism. ES (excited state); GS (ground state); ICT (intermolecular charge transfer).

Empirical solvent polarity scales were developed in order to quantify solvent effects on physical absorptions. Among the varying empirical solvent polarity scales, the

E_T^N and π* scales were utilized in this study. The E_T^N scale is based on the utilization of water and tetramethylsilane (TMS), ranging from polar to nonpolar.[19] The π* values stem from the solvent-induced shifts of the π→π* absorption band of seven nitroaromatic indicators.[19] The π* scale values are optimized for cyclohexane as the most non-polar (π* = 0.000) and dimethyl sulfoxide (DMSO) the most polar (π* = 1.000).[19]

1.5 Research Goals

The purpose of this study is to synthesize and characterize a series of DA dyes. A geometric analysis will be conducted to predict possible structural trends as well as possible effects of nitrogen atom geometry on the overall dye electronic structure. To understand the electronic properties, BLA values will be calculated from ^{1}H NMR coupling constants. Also, solvatochromic effects will be analyzed for ^{1}H and ^{13}C spectra. Even though β values will not be measured, this study will provide insight into geometrical and physical parameters that affects a series of NLO active molecules.

CHAPTER II

EXPERIMENTAL

To study the effect of amine donor group geometry on conjugation and donor strength**,** six new compounds were synthesized: 2-(3-cyano-4-((1E,3E,5E)-6-(4-(dimethylamino)phenyl)hexa-1,3,5-trienyl)-5,5-dimethylfuran-2(5H)-ylidene)malonitrile (**1**), 2-(3-cyano-5,5-dimethyl-4-((1E,3E,5E)-6-(1-methylindolin-5-yl)hexa-1,3,5-trienyl)furan-2(5H)-ylidene)malononitrile (**2**), 2-(3-cyano-5,5-dimethyl-4-((1E,3E,5E)-6-(1-methyl-1,2,3,4-tetrahydroquinolin-6-yl)hexa-1,3,5-trienyl)furan-2(5H)-ylidene)malononitrile (**3**),6-(4-Julolidin-4-yl)-2,4,6-hexatrienyl-tricyanofuran (**4**), 5-((2E,4E)-5-(4-(dimethylamino)phenyl)penta-2,4-dienylidene)-1,3-diethyl-2-thioxo-dihydropyrimidine-4,6(1H,5H)-dione (**5**), and 5-(4-julolidinyl)-2,4-pentadienyl-*N*,*N*-diethylthiobarbituric acid (**8**). Compounds (2*E*, 4*E*)-(5-(4-N-Methyl indolinyl)-penta-2,4,6-trienyl)-thiobarbituric acid(**6**) and (2*E*, 4*E*)-5-(1-Methyl-1,2,3,4-tetrahydroquinolin-6-yl)penta-2,4-dienyl thiobarbituric acid (**7**) were previously synthesized and properties are used for comparison purposes.[20] It should be further acknowledged that compound **2** was synthesized by Andy Standley, compound **3** by Ama Quao, compound **5** by Andrienne Friedli, and compound **8** by Honorio Gonzalez. **Figure 4** illustrates the eight target dyes that were utilized throughout this study.

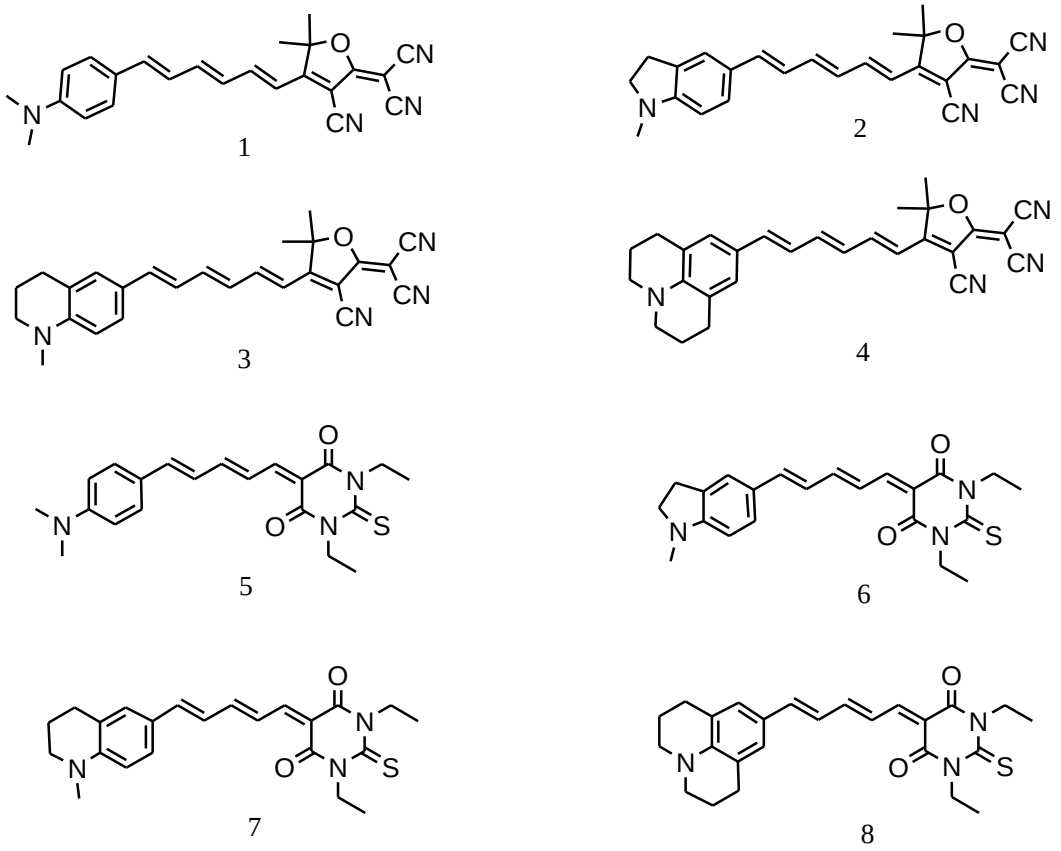

Figure 4. Synthesized compounds **1**-**8**.

2.1 Reagents

1,4-Dioxane (99+%) and acetonitrile (99+%) were purchased from Acros. Hydrochloric acid was purchased from EMD. Cyclohexane (99.8%), anhydrous ethyl ether, chloroform-reagent grade, methylene chloride (99.9%), sodium sulfate, sodium hydroxide, ethyl acetate, and hexanes were purchased from Fisher Scientific. Carbon tetrachloride was purchased from Norell, Inc and ethanol-absolute anhydrous (200 proof) from Pharmco-AAPER. Toluene (99.85), tetrahydrofuran (≥ 99.9%), acetone (99.9+%), pyridine (99.8%), dimethylformamide (≥ 99.9%), dimethyl sulfoxide (99.5%), tert-butyl

lithium, 4-methylpiperidine (96%), lithium wire (99.9%), 3-hydroxy-3-methyl-2-butanone (95%), and malonitrile (≥ 99%) were purchased from Sigma Aldrich.

2.2 UV Spectroscopy and FT-IR

Ultraviolet-visible spectra were measured using an Agilent Technologies Diode Array Spectrophotometer. Data was collected between 400 – 800 nm, maintaining an absorbance between 0.500 ± 0.05. Several solvents were utilized to observe differing maximum wavelengths (λ_{max}), which can be seen in Appendix **A.** Beer's Law plots were constructed to determine a quantitative value for the molar extinction coefficient (ε). Samples were prepared in chloroform at three different concentrations corresponding to absorbance values ranging from 0.10 – 0.80.

FT-IR analysis was done on a Varian 7000 FT-IR Spectrometer. To make a proper analysis, solid samples were dissolved in chloroform and loaded on the surface of the FT-IR. After the solvent evaporated, additional solution was added. This method was repeated several times to ensure a sufficient amount of sample was present on the analyzer.

2.3 NMR and Mass Spectroscopy

NMR analysis was performed on a JEOL EMX 500 MHz NMR and spectra recorded in **Appendix B**. Samples were analyzed in DMSO-*d6*, acetone-*d6*, chloroform-*d*, acetonitrile-*d3*, and sometimes THF-*d*8 or benzene-*d6*. All deuterated solvents were 99.9 % pure and purchased from Cambridge Isotopes (Andover, MD) or Sigma-Aldrich (Milwaukee, WI). Spectra were analyzed to determine the coupling constants and

chemical shifts for the each individual dye. Spectra were referenced to residual protic solvent chemical shifts.[21] To confirm proton assignments, homonuclear correlation spectroscopy (COSY) was utilized to identify spins which are coupled to each other. Other tools, heteronuclear single-quantum correlation spectroscopy (HSQC) and heteronuclear multiple quantum coherence (HMQC), were used to detect correlations between nuclei of two different types that are separated by one bond. To confirm the molecular formula, samples were analyzed on a Bruker micrOTOF mass spectrometer by electrospray ionization (ESI) from the Mass Spectrometry & Proteomics Facility at Notre Dame University.

2.4 Synthesis and Characterization

(2E,4E)-5-(4-(Dimethylamino)phenyl)penta-2,4-dienal (9).[22] Compound **15** (0.720 g, 0.004 mol) was dissolved in THF (10 mL) and cooled to -78°C under argon. *t*-Butyl lithium (4.2 mL) was added drop wise and stirred for one hour. The solution was warmed to 0°C. Next, the solution was cooled to -78°C and compound **16** (0.460 g, 0.003 mol) added in THF. The solution was warmed to room temperature and then shaken in a separatory funnel with 2 M HCl. A 10% NaOH solution was added until a pH ~ 10 was reached. Caution was exercised when adding 10% NaOH. A few drops were added, stirred, and the pH was checked. The organic phase was separated and aqueous layer washed with ether. The combined organic layers were dried over Na_2SO_4, evaporated, and purified by flash chromatography of silica gel using 40% ethyl acetate in hexanes. Recrystallization was done to further purify the final product and resulted in 307 mg of yellow crystalline product (R_f = 0.54). Yield: 51 %; ^{1}H-NMR ($CDCl_3$): δ

3.03 (s, 6H), 6.18 (dd, J = 8.1, 14.9 Hz, 1H), 6.68 (d, J = 8.6 Hz, 2H), 6.82 (dd, J = 11.1, 15.2 Hz, 1H), 6.95 (d, J = 15.2 Hz, 1H), 7.26 (dd, J = 10.6, 15.2 Hz, 1H), 7.40 (d, J = 8.6, 2H), 9.56 (d, J = 8.0 Hz, 1H); ^{13}C NMR ($CDCl_3$): δ 193.7, 153.9, 151.3, 143.6, 129.2, 128.9, 123.5, 121.5, 111.9, 40.1; UV/vis: λ_{max} = 414 nm (log ε = 4.22 M^{-1} cm^{-1}).

5-((2E,4E)-5-(4-(Dimethylamino)phenyl)penta-2,4-dienylidene)-1,3-diethyl-2-thioxo-dihydropyrimidine-4,6(1H,5H)-dione (5).[22] Compounds **14** (55.3 mg, 0.276 mmol) and **9** (55.1 mg, 0.274 mmol) were dissolved separately in hot ethanol and then combined. The combined reagents were heated and stirred for 30 minutes. The solution was cooled and precipitate was collected on a Hirsch Funnel to give a green powder (95.5 mg). Yield: 91 %; ^{1}H-NMR ($CDCl_3$): δ 1.30 (q, J = 6.9, 14.9 Hz, 6H), 3.07 (s, 6H), 4.57 (t, J = 3.5 Hz, 4H), 6.68 (dd, J = 8.6 Hz, 2H), 6.98 (dd, J = 14.9, 11.4 Hz, 1H), 7.07 (d, J = 14.9 Hz, 1H), 7.34 (dd, J = 14.1, 11.2 Hz, 1H), 7.43 (d, J = 9.2 Hz, 2H), 8.05 (t, J = 13.7, 12.6 Hz, 1H), 8.13 (d, J = 12.6 Hz, 1H); ^{13}C NMR: δ 12.6, 40.2, 43.2, 43.7, 111.7, 112.1, 123.9, 124.1, 127.5, 130.5, 152.1, 158.5, 158.7, 160.1, 161.1, 178.9; UV/Vis: λ_{max} = 600 nm (log ε = 4.89 M^{-1} cm^{-1}).

General Procedure for Knoevenagel Condensation of Aldehydes with 2-(3-Cyano-4,5,5-trimethylfuran-2(5H)-ylidene) malononitrile (TCF).[23] Compounds **13** (27.9mg, 0.140mmol) and **9** (25.5 mg, 0.127 mmol) were mixed in ethanol and allowed to reflux for 14 hours, or until TLC demonstrated the disappearance of the aldehyde. The solution was allowed to cool, filtered under vacuum with a Hirsh Funnel and rinsed with hot

ethanol. A green solid was collected and allowed to air dry. The solid was placed under vacuum to remove residual solvent.

2-(3-Cyano-4,5,5-trimethylfuran-2(5H)-ylidene) malononitrile (13).[23,24] Under anhydrous conditions, 3-hydroxy-3-methyl-2-butanone (5.00 g, 0.0490 mol) and malononitrile (6.65 g, 0.101 mol) were dissolved into 125 mL of absolute alcohol. The dissolved solution was attached to reflux condenser and Soxhlet extractor (4 Å molecular sieves). A trace amount of lithium wire (6 mg) was added to the mixture and allowed to reflux for 8 h. Mixture was brought to room temperature and TCF crystals separated out. Crystals were recrystallized with hot ethanol. Yield: 4.40 g (45.1%); ^{1}H-NMR ($CDCl_3$): δ 1.62 (s, 6H), 2.36 (s, 3H); ^{13}C-NMR ($CDCl_3$) δ: 14.31, 24.46, 58.55, 99.89, 104.87, 109.07, 110.51, 111.13, 175.31, 182.73; FT-IR: 860 cm^{-1} (C-H bend), 1157 cm^{-1} (C-O stretch), 1610 cm^{-1} (C=C stretch), 2229 cm^{-1} (nitrile stretch).

2-(3-Cyano-4-((1E,3E,5E)-6-(4-(dimethylamino)phenyl)hexa-1,3,5-trienyl)-5,5-dimethylfuran-2(5H)-ylidene)malononitrile (1). Yield: 65.6%; Dec. onset DSC: 218 °C ; ^{1}H-NMR ($CDCl_3$): δ 1.70 (s, 6H), 3.06 (s, 6H), 6.34 (d, J = 14.9 Hz,1H), 6.48 (dd, J = 11.4, 14.3 Hz, 1H), 6.68 (d, J = 9.2 Hz, 2H), 6.82 (dd, J = 10.9, 14.9 Hz, 1H), 6.91 (d, J = 15.5 Hz, 1H), 7.04 (dd, J = 11.2, 14.0 Hz, 1H), 7.41 (d, J = 9.1 Hz, 2H), 7.52 (dd, J = 11.5, 15.5 Hz, 1H);^{13}C-NMR ($CDCl_3$): δ 26.57, 40.23, 96.9, 112.2, 111.2, 111.6, 112.2, 112.4, 115.7, 123.4, 124.1, 128.9, 129.8, 144.0, 148.9, 149.5, 151.7, 173.3, 176.0; FT-IR 2222 cm^{-1}(nitrile); UV/vis: λ_{max} = 648 nm (log ε = 4.81 M^{-1} cm^{-1}); HRMS: $C_{24}H_{23}N_4O$: 383.1866, observed = 383.1872.

2-(3-Cyano-5,5-dimethyl-4-((1E,3E,5E)-6-(1-methylindolin-5-yl)hexa-1,3,5-trienyl)furan-2(5H)-ylidene)malononitrile (2) Yield: 19.0 % ; Dec onset (DSC) 221 °C; ^{1}H-NMR ($CDCl_3$): δ 1.69 (s, 6H), 2.86 (s, 3H), 3.02 (t, J = 8.6 Hz, 2H), 3.50 (t, J = 8.6 Hz, 2H), 6.32 (d, J = 14.9 Hz, 1H), 6.38 (d, J = 8.6 Hz, 1H), 6.45 (dd, J = 11.5, 13.8 Hz, 1H), 6.78 (dd, J = 11.2, 15.2 Hz, 1H), 6.89 (d, 15.4 Hz, 1H), 7.03 (dd, J = 11.2, 14.1 Hz, 1H), 7.22 (d, J = 8.6 Hz, 1H), 7.27 (s, 1H), 7.51 (dd, J = 11.5, 14.0 Hz, 1H);^{13}C-NMR: δ 26.56, 27.93, 28.31, 34.63, 55.14, 57.76, 96.92, 101.27, 105.99, 111.71, 115.44, 121.28, 122.90, 123.27, 125.62, 128.75, 130.73, 131.21, 132.95, 144.28, 149.01, 149.38, 149.86, 155.34, 158.17; FT-IR: 2223 cm^{-1} (nitrile stretch); UV/vis: λ_{max} = 668 nm (log ε = 4.66); HRMS: $C_{25}H_{23}N_4O$ = 395.1866, observed = 395.1872.

2-(3-Cyano-5,5-dimethyl-4-((1E,3E,5E)-6-(1-methyl-1,2,3,4-tetrahydroquinolin-6-yl)hexa-1,3,5-trienyl)furan-2(5H)- ylidene)malononitrile (3) Yield: 70 %; Dec onset (DSC) 189 °C; ^{1}H-NMR ($CDCl_3$): δ 1.69 (s, 6H), 1.98 (t, J = 6.0 Hz, 2H), 2.76 (t, J = 6.3 Hz, 2H), 2.99 (s, 3H), 3.36 (t, J = 5.8 Hz, 2H), 6.31 (d, J = 14.9 Hz, 1H), 6.45 (dd, J = 11.8, 14.1 Hz, 1H), 6.53 (d, J = 8.6 Hz, 1H), 6.79 (dd, J = 10.9, 14.9 Hz, 1H), 6.87 (d, J = 14.9 Hz, 1H), 7.03 (dd, J = 10.9, 13.8 Hz, 1H), 7.14 (s, 1H), 7.29 – 7.23 (m centered at 7.25, 2H), 7.51 (dd, J = 11.5, 15.5 Hz, 1H);^{13}C-NMR: δ21.82, 26.51, 27.73, 38.89, 51.19, 94.77, 96.82, 105.11, 110.44, 111.72, 112.47, 115.23, 122.80, 123.70, 128.31, 128.85, 134.21, 144.51, 148.39, 148.96, 149.86, 173.09, 175.85; UV/vis: λ_{max} = 681 nm (log ε = 4.67); HRMS: Calcd. $C_{26}H_{25}N_4O$: 409.2023; Obsd. 409.2028.

6-(4-Julolidin-4-yl)-2,4,6-hexatrienyl-tricyanofuran (4) Yield: 42.7 %; Dec. onset (DSC): 201 °C; ^{1}H-NMR ($CDCl_3$): δ 1.67 (s, 6H), 1.94 – 1.99 (m centered at 1.96, 4H), 2.74 (t, J = 6.3 Hz, 4H), 3.28 (t, J = 5.8 Hz, 4H), 6.28 (d, J = 15.5 Hz, 1H), 6.43 (dd, J = 11.5, 13.8 Hz, 1H), 6.76 (dd, J = 10.6, 14.6 Hz, 1H), 6.83 (d, J = 14.9 Hz, 1H), 6.98 (s, 2H), 7.02 (dd, J = 10.9, 14.4 Hz, 1H), 7.51 (dd, J = 11.5, 14.9 Hz, 1H); ^{13}C-NMR ($CDCl_3$): δ 21.5, 26.7, 27.8, 50.2, 58.6, 96.7, 107.6 110.0, 111.6, 111.9, 112.8, 114.8, 121.5, 122.5, 123.1, 127.9, 128.1, 145.2, 145.4, 149.2, 150.5, 173.1, 176; FT-IR: 2223 cm^{-1} (nitrile stretch)UV/vis: λ = 722 nm (log ε = 4.52 M^{-1} cm^{-1}); HMRS: Calcd. $C_{28}H_{27}N_4O$: 435.2179; Obsd.: 435.2185.

CHAPTER III

RESULTS AND DISCUSSION

3.1 Geometrical Effects

To examine the postulated effects of pyramidalization on conjugation, compounds **1-8** were modeled by utilizing a DFT/B3LYP 6-31G** basis set in PC Spartan package.[25] This specific basis set was chosen due to its reliability and good predictive power for spectroscopic data.[17] Pyramidalization is the phenomenon where the nitrogen trigonal planar geometry is forced to adopt a tetrahedral geometry due to restricted conformations. This distortion caused from pyramidalization could force the molecule into a new conformation, reducing planarity, and decreasing the level of conjugation. To quantify this distortion, several angles were calculated (**Table 1**). An illustration of these measured angles can be seen in **Figure 5**.

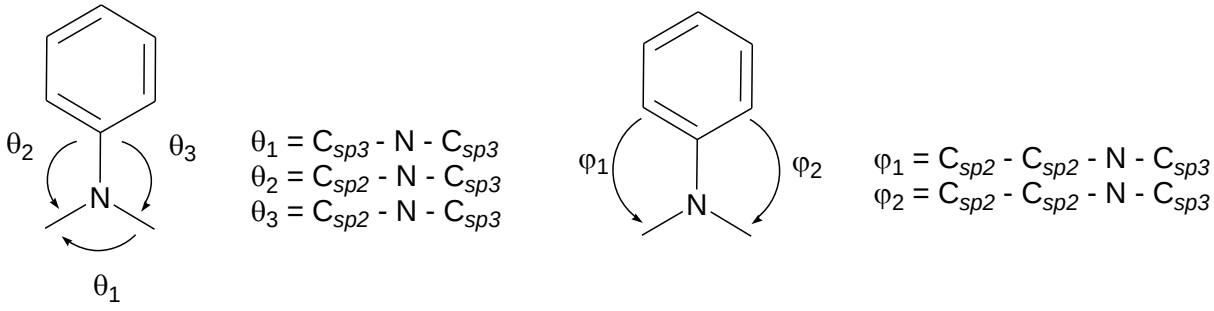

Figure 5. Illustration of varying angle planes and dihedral angles. Angle θ_1 represents the plane between C_{sp3} - N - C_{sp3}, θ_2 betweenC_{sp2} - N - C_{sp3}, and θ_3 between C_{sp2} - N - C_{sp3}. Angle φ_1 represents the ring dihedral angle between the C_{sp2} - C_{sp2} - N - C_{sp3}whereas φ_2 represents the methyl dihedral angle between the C_{sp2} - C_{sp2} - N - C_{sp3}.

Based on **Table 1**, several trends can be observed. Compounds **1** and **5** are not restricted by ring strain, have free rotation about the N – C_{sp2} axis, and thus adopt more of a trigonal planar geometry. It can be observed from **Table 1** that compounds **1** and **5** show minimal variation in angles θ_1, θ_2, and θ_3. Additionally, dihedral angles φ_1 and φ_2 for compounds **1** and **5** appear to be relatively small and suggest a coplanar relationship between the alkyl groups on nitrogen and the aromatic ring. Conversely, in compounds **2** and **6**, the alkyl groups are not coplanar with the aromatic ring. The nitrogen atom in compounds **2** and **6** is bound within a five-membered ring, lacking free rotation about the N – C_{sp2} axis, resulting in a nearly tetrahedral geometry. The dihedral angles reveal that angle strain from the five-membered ring, inducing a distortion that pushes the methyl group out of plane and leading to non-coplanarity. This distortion could limit the level of conjugation throughout the dye. For compounds **3** and **7**, the nitrogen atom is bound within a six-membered ring. Like compounds **2** and **6**, the constraint of the ring causes a distortion in angles θ_1, θ_2, and θ_3. However, the angle distortions are not as pronounced and maintain trigonal planar geometry (with some variation). Lastly, the nitrogen atom for compounds **4** and **8** is shared between two six-membered rings. These two compounds tend show some derivation from 120 º but never reaches the 109.5 º requirements for tetrahedral geometry. In **Figure 6**, θ_1, θ_2, and θ_3 are correlated against the methyl dihedral angle (φ_2). The overall effect of ring strain can be observed in **Figure 6** for compounds **1-8**. As the strain of the heterocyclic ring increases, an increased deviation from 120 º is observed for compounds **2** and **6**. It is interesting to note the large deviation between pairs **2,6** and **3,7** illustrated in **Figure 6**. Decreasing the

heterocyclic ring by one carbon, forces angles θ_1, θ_2, and θ_3 for compounds **2, 6** to show large deviations from the 120 º and larger shifts in dihedral angle φ_2. Compounds **3, 7** show some deviation from 120 º. However, the cyclohexane ring is less strained and stablilizes the nitrogen and limits its deviations.

Table 1. Bond Lengths and Angles Calculated from Spartan Modeling Using DFT/B3LYP 6-31G**.

Compds	**N-C*sp2*** (Å)	**C*sp3*-N-C*sp3*** (θ_1)	**C*sp2*-N-C*sp3*** (θ_2)	**C*sp2*-N-C*sp3*** (θ_3)	**Ring Dihedral** (φ_1)	**Methyl Dihedral** (φ_2)
1	1.374	119.55	120.14	120.30	-0.49	0.21
2	1.380	119.18	108.88	123.02	-15.15	18.66
3	1.375	117.79	121.38	120.35	-3.64	4.89
4	1.384	116.28	120.52	120.64	-10.33	9.93
5	1.375	119.56	120.08	120.31	-1.75	1.02
6	1.380	119.21	108.95	123.02	-15.10	18.71
7	1.380	117.38	120.79	120.04	-8.20	8.2
8	1.385	116.08	120.82	120.40	-10.95	9.79

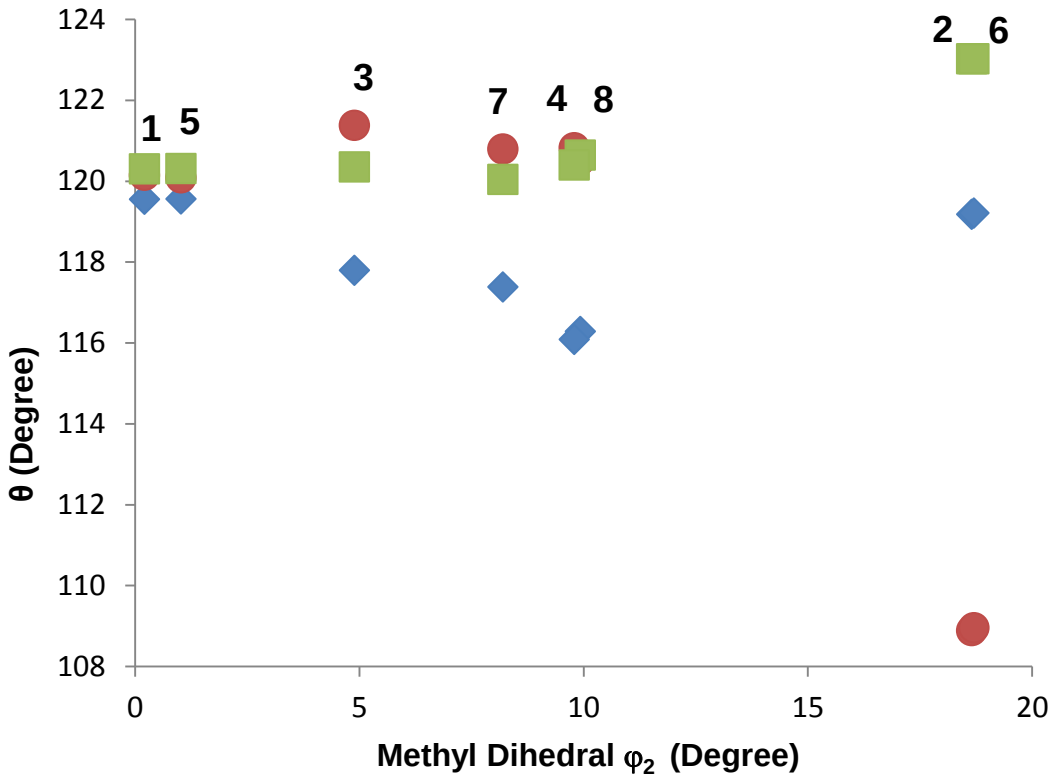

Figure 6. Angle (θ) vs Methyl Dihedral (φ_2) for compounds **1** – **8**. θ_1 (blue diamond); θ_2 (red circle); θ_3 (green square).

3.2 Synthesis

A three-step method was utilized to synthesize compounds **9** – **12** (**Figure 7**). First, a selective electrophilic aromatic bromination using N-bromosuccinimide was accomplished, yielding para-brominated products (compounds **15** and **18**).[26] Following the bromination, a lithium halogen exchange was carried out on compounds **15** and **18** as well as a nucleophilic addition to compound **16**, resulting in the formation of compounds **9** and **12**.

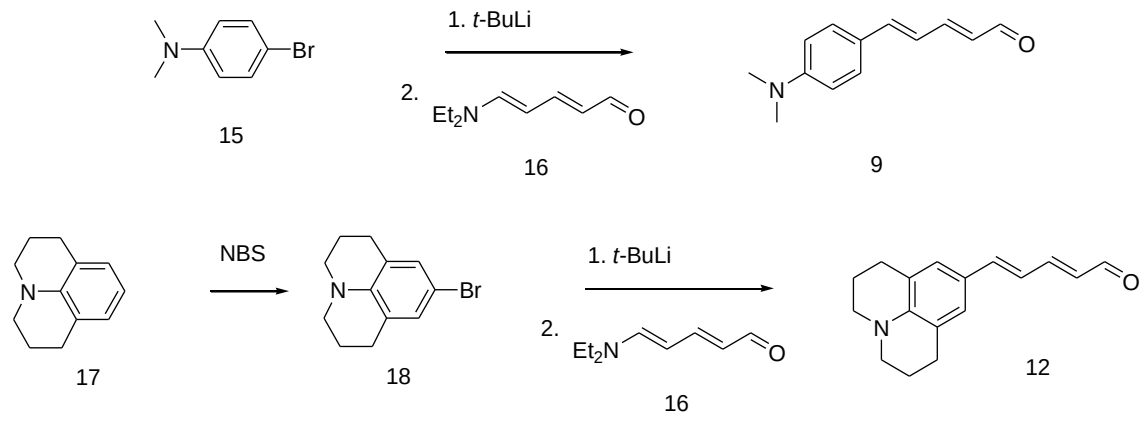

Figure 7. Synthesis of aldehydes **9** and **12**.

To make electronic structural comparisons, compounds **9** – **12** were converted into push-pull donor-acceptor dyes by attaching two strong acceptors, 2-(3-cyano-4,5,5-trimethylfuran-2(5H)-ylidene) malononitrile (**13**) and N, N-diethyl thiobarbituric acid (**14**). Attachment of these strong acceptors was accomplished via Knoevenagel condensations.

Condensations with compound **14** (**Figure 9**) resulted in compounds **5** – **8** that were slightly soluble in hot ethanol. To obtain nearly a quantitative yield, the solution allowed to reflux for 15 minutes. Similarly, condensations with compound **13** (**Figure 8**) resulted in compounds **1**-**4** that were slightly soluble in hot ethanol but required catalytic piperidine to reach the desired product. Actual yields for compounds **1** – **4** were very low, with compound **1** producing the highest yield, compounds **2** and **3** relatively the same, and compound **4** with the lowest. After isolating compounds **1** – **4** and allowing to air dry, rinsing the dyes with hot ethanol removed residual contaminants within the

sample.[2] This purification method proved to be very effective and resulted in relatively pure samples (confirmed by ^{1}H NMR).

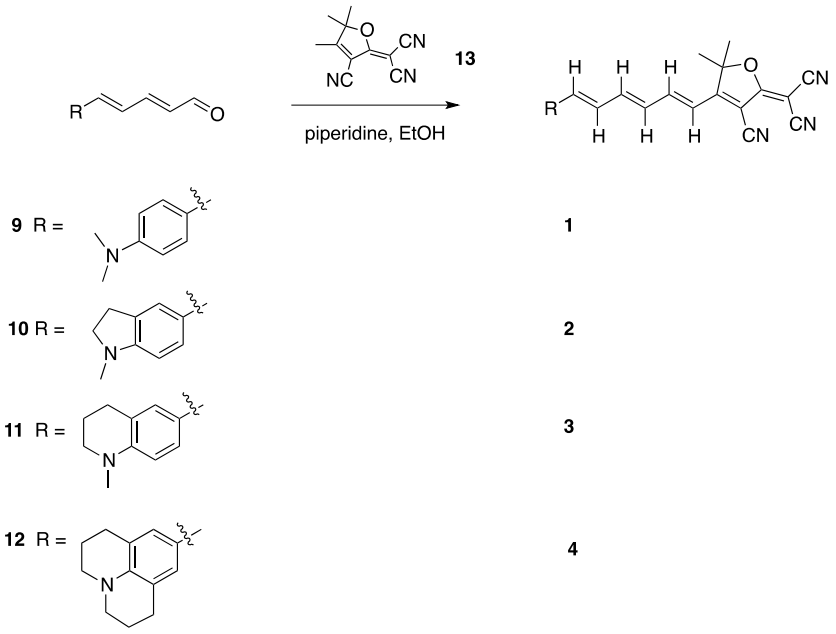

Figure 8. Synthesis of tricyanofuran derivatives **1-4** from aldehydes **9-12.**

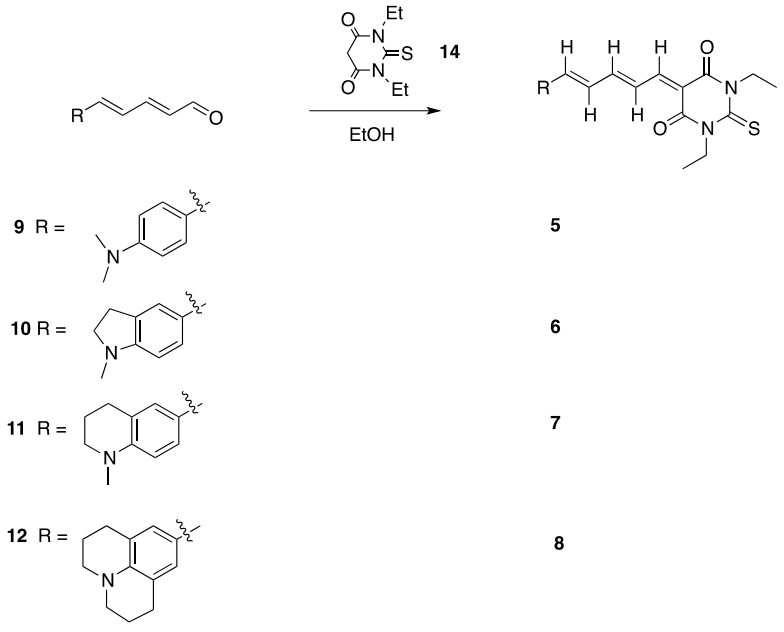

Figure 9. Synthesis of thiobarbituric derivatives **5-8** from aldehydes **9-12**.

3.3 UV-Vis Spectrometry and Solvatochromism

Solvatochromic studies for compounds **1-8** were performed in several solvents (**Appendix A**), focusing on the UV-Vis region. The experimental λ_{max} was plotted against a solvent polarity parameter (π^*) to analyze possible solvatochromic trends.[19] Previously, E_T^N and $E_T(30)$ polarity parameters were utilized to observe solvent effects on wavelength.[19] It was determined that the π^* polarity parameter correlated better with experimental solvent effects. The π^* scale is an experimentally determined scale that is based on solvatochromic effects of n $\rightarrow \pi^*$ and $\pi \rightarrow \pi^*$ transitions.[5] It originates from experimental averaged values of indicator solvents and their corresponding sovatochromic behaviors. Compounds **5-8** presented good solubility and allowed for several solvents to be tested. Typically, solvents with the ability to hydrogen bond can strongly affect the sample and produce results that fluctuate. However, compounds **5-8** were minimally affected and proved to be stable in hydrogen-bonding solvents.

A shift to longer wavelengths (positive solvatochromism) is observed as the polarity of the solvent is increased (**Figure 10**). In **Figure 11**, the experimental λ_{max} for compounds **5-8** was plotted against the π^* polarity scale. It can be observed that compound **5** shifts to longer wavelengths, which indicates an increased amount of energy between the ground state and first excited state (ICT band gap).[19] Conversely, compound **8** shifts to longer wavelengths with a decreased amount of energy between the ground state and first excited state. As polarity increases, the ICT band shifts to longer wavelengths, decreasing the energy transfer due to stabilization in the excited state. Additionally, compounds **6** and **7** seem to rank in similar energies between both

extremes. To quantify the solvent stabilization of the charge separated state (ΔS), the difference between the most polar solvent (DMSO) and the least polar solvent (ether) was taken. The ΔS values measured were 108 nm for compound **6**, 96 nm for compound **7**, 86 nm for compound **8**, and 76 nm for compound **5**.

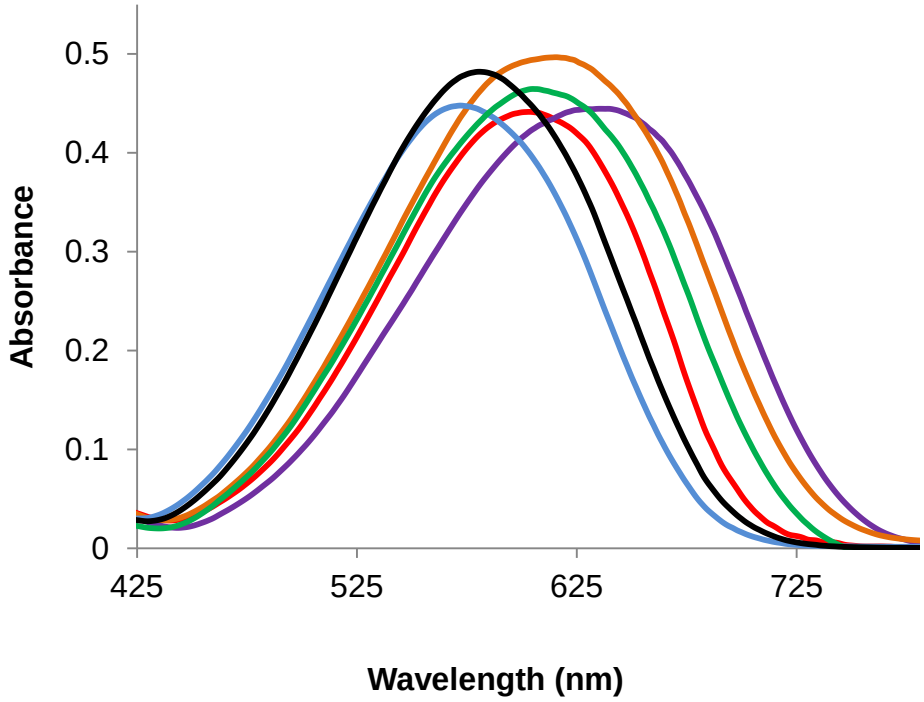

Figure 10. Illustration of positive solvatochromism for compound **5** in varying solvents. Ethyl Acetate (blue), THF (black), $CHCl_3$ (red), Ethanol (green), DMF (orange), and DMSO (purple).

In **Figure 12**, the experimental λ_{max} for compounds **1-4** was plotted against the π^* polarity scale. In comparison to **Figure 11**, solvatochromic trends were more difficult to

interpret for compounds **1-4**. In comparison to compounds **5- 8**, compounds **1-4** presented poor solubility which resulted in a smaller range of solvents that could be tested (**Figure 12**).

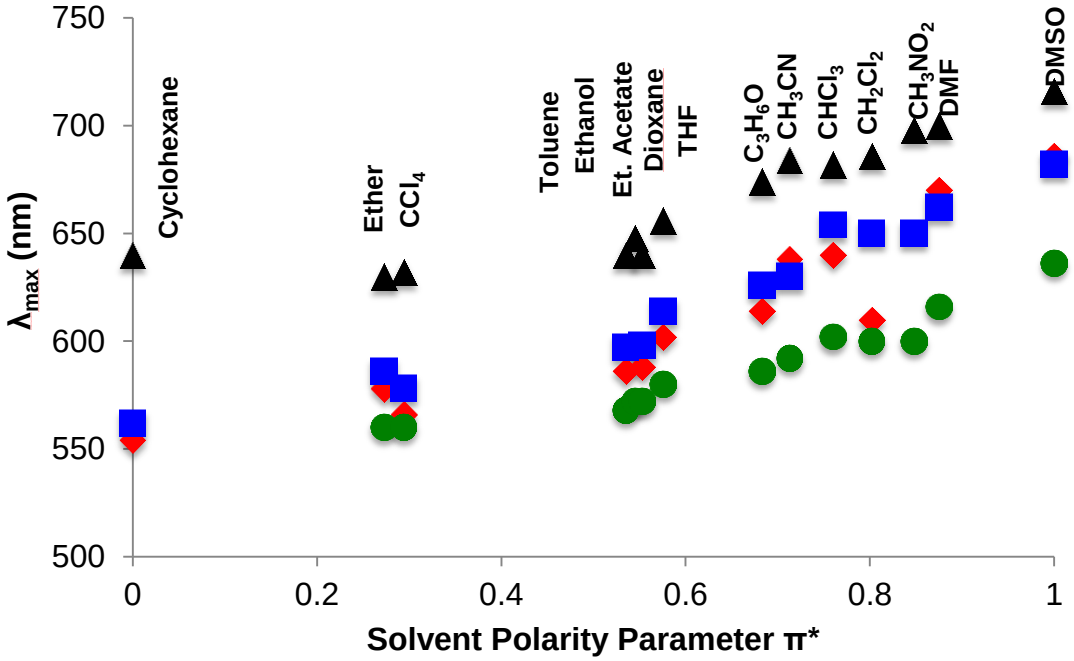

Figure 11. λ_{max} vs π* polarity scale for compounds **5-8** in varying polar solvents. **5** (green circle); **6** (red diamond); **7** (blue squre); **8** (black triangle).

In **Figure 12**, the experimental λ_{max} for compounds **1-4** was plotted against the π* polarity scale. In comparison to **Figure 11**, solvatochromic trends were more difficult to interpret for compounds **1-4**. In comparison to compounds **5- 8**, compounds **1-4**

presented poor solubility which resulted in a smaller range of solvents that could be tested (**Figure 12**). In **Figure 13**, several λ_{max} values were eliminated due to irregularities in solvatochromic trends. Eliminated λ_{max} values were chosen due to increased sensitivity to solvents that involve hydrogen bonding, chlorinated compounds, or sample decomposition. Despite the apparent randomness between π^* and λ_{max} in **Figure 12**, trends can be observed between compounds containing the same donor group. Compounds **1** and **5** (dimethylamino donor) show the lowest λ_{max} values and compounds **4** and **8** (julolidine donor) have the largest λ_{max} values. This suggests a larger ICT band gap for compounds **1** and **5** and a smaller gap for compounds **4** and **8**. Similar to compounds **5-8**, indoline and tetrahydroquinoline donors have λ_{max} values between julolidine and dimethylamino donor groups with similar ICT band gaps, as solvent polarity increases. The ΔS for compounds **1-4** was calculated between the most polar solvent (DMSO) and the least polar solvent (dioxane). Dioxane was chosen as the least polar solvent due to toluene's producing anomalous data points. The ΔS values measured were 52 nm for compound **4**, 44 nm for compound **3**, 40 nm for **2**, and 36 nm for **1**. Irreproducible

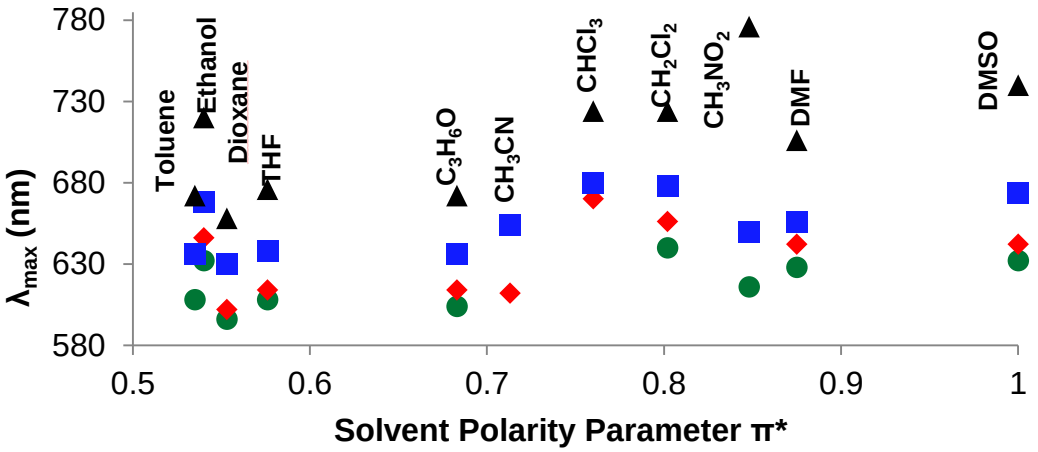

Figure 12. λ_{max} vs π* polarity scale for compounds **1-4** in varying polar solvents. **1** (green circle); **2** (red diamond); **3** (blue square); **4** (black triangle).

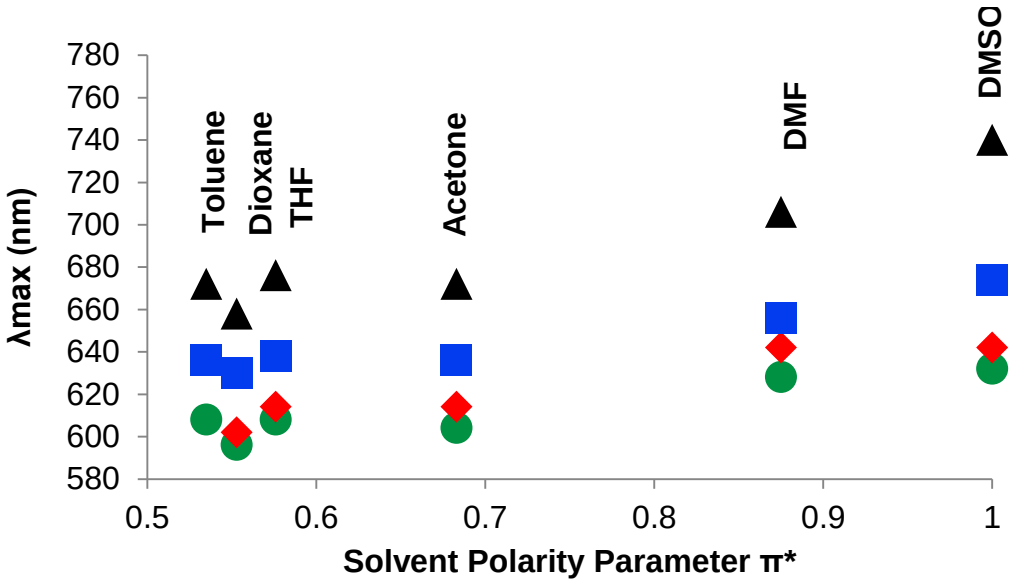

Figure 13. λ_{max} vs π* polarity scale for compounds **1-4** in varying polar solvents. **1** (green circle); **2** (red diamond); **3** (blue squre); **4** (black triangle).

3.4 NMR Spectroscopy and Solvatochromism

3.4.1 ^{1}H NMR

To study the effects of amine donor group geometry on conjugation and donor strength, the solvatochromism for ^{1}H NMR was analyzed using the E_T^N solvent polarity scale. Each compound was analyzed in several solvents. To discover solvatochromic trends, proton-coupling constants (J) were calculated to determine the degree of BLA between single and double bonds in the polyene chain. To correlate BLA to J, the difference between the average coupling constants for C=C bond and C-C bond was taken (ΔJ).[27] The lower the ΔJ value the less BLA that is observed in a molecule. Lower ΔJ values indicate more contribution of the two resonance structures in the ground state (BLA = 0.0-0.11 A). The Coupling constants are typically larger for protons on double bonds versus single bonds. Also, changes in chemical shifts with increased solvent polarity were examined to determine charge stabilization.

For ^{1}H NMR, a general letter designation was established to differentiate protons and monitor changes in chemical shifts and coupling constants (**Figures 14 -15**).

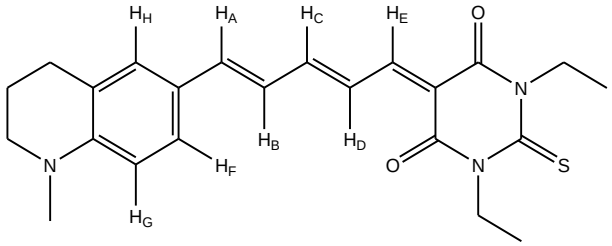

Figure 14. Proton letter designation for compound **7**.

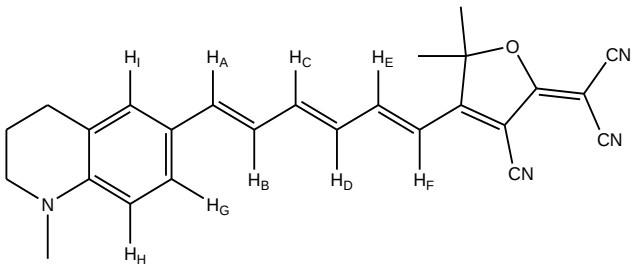

Figure 15. Proton letter designation for compound **3**.

For compounds **5-8**, solvatochromic trends in chemical shifts are observed in **Figures 16-19**. It appears that protons nearest the donor are subjected to a greater shielding effect and shift more upfield. Conversely, the acceptor has an electron withdrawing effect. The protons nearest the acceptor experience a greater effect from the external magnetic field and shifted downfield. It can be observed that H_C is affected mostly as the solvent polarity is increased. It is susceptible to effects from both the donor as well as the acceptor. Additionally, **Figure 19** represents complications resulted in characterizing every proton. Several contributing factors include second order coupling, possible concentration effects, decomposition, and poor solubility, preventing a complete solvatochromic analysis on every proton.

To determine the amount of BLA, coupling constants were calculated from the ^{1}HNMR spectra (**Table 2**). ΔJ was calculated by taking the difference between the average C=C bond and average C-C bond coupling constants. To observe changes in BLA, the ΔJ values were plotted against the solvent polarity parameter E_T^N (**Figure 20**). From **Figure 20**, an effect of solvent polarity on ΔJ can be observed. As the polarity

increases, an overall decrease in ΔJ is observed with a corresponding increase in conjugation. In DMSO, compounds **5** and **7** have the highest ΔJ values whereas compound **8** has the lowest ΔJ. A lower ΔJ correlates to an increased amount of conjugation. This can be confirmed in **Figure 11** that illustrates positive solvatochromism.

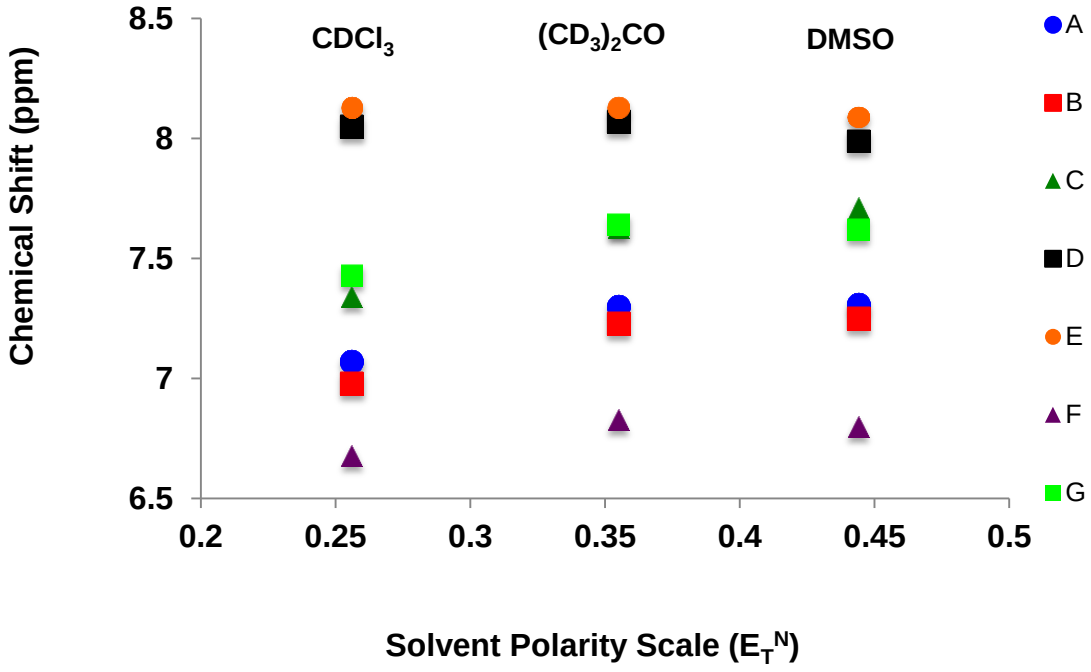

Figure 16. Chemical Shift (ppm) vs Solvent Polarity Scale E_T^N for compound **5**.

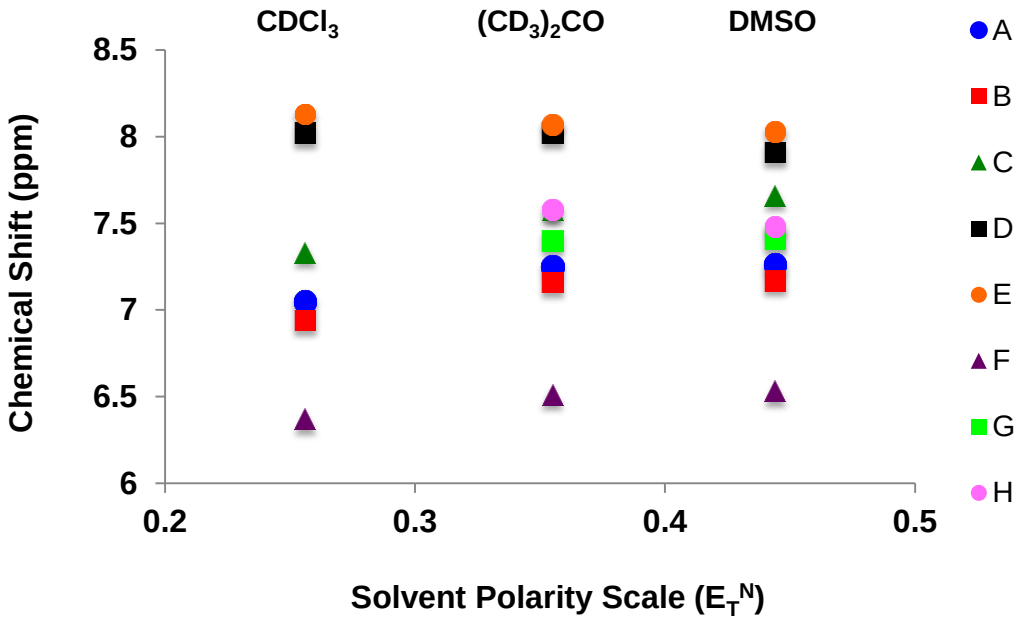

Figure 17. Chemical Shift (ppm) vs Solvent Polarity Scale E_T^N for compound **6**.

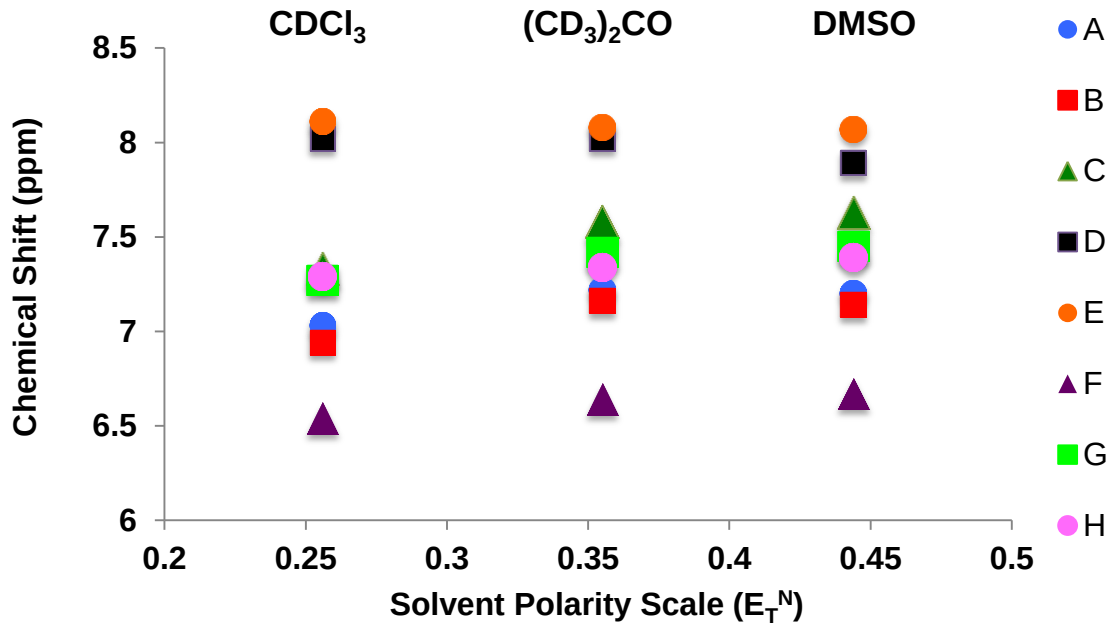

Figure 18. Chemical Shift (ppm) vs Solvent Polarity Scale E_T^N for compound **7**.

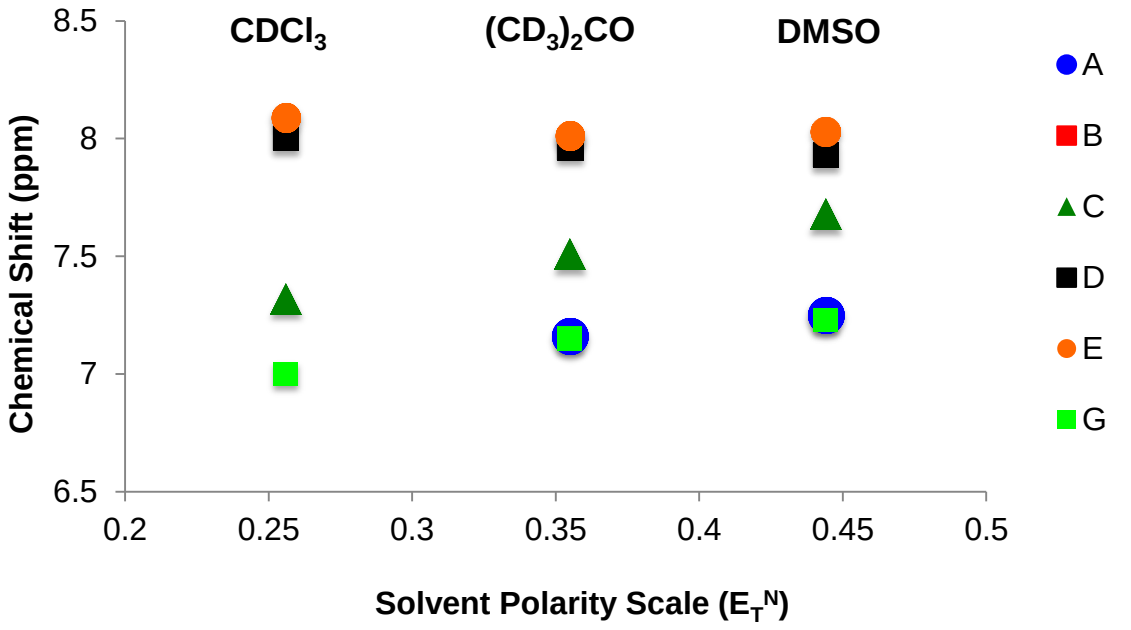

Figure 19. Chemical Shift (ppm) vs Solvent Polarity Scale E_T^N for compound **8**.

Table 2. Coupling Constants for Compounds **5-8** in $CDCl_3$.

	5	**6**	**7**	**8**
AB	14.9	14.9	14.9	14.9
BA	14.9	14.9	14.9	14.9
BC	11.4	11.5	11.5	10.9
CB	11.2	13.7	10.9	10.9
CD	14.1	13.2	13.7	13.8
DC	13.7	11.5	13.2	13.2
DE	12.6	13.2	13.2	13.2
ED	12.6	12.6	12.6	12.6
ΔJ	**2.45**	**2.0**	**2.13**	**2.3**

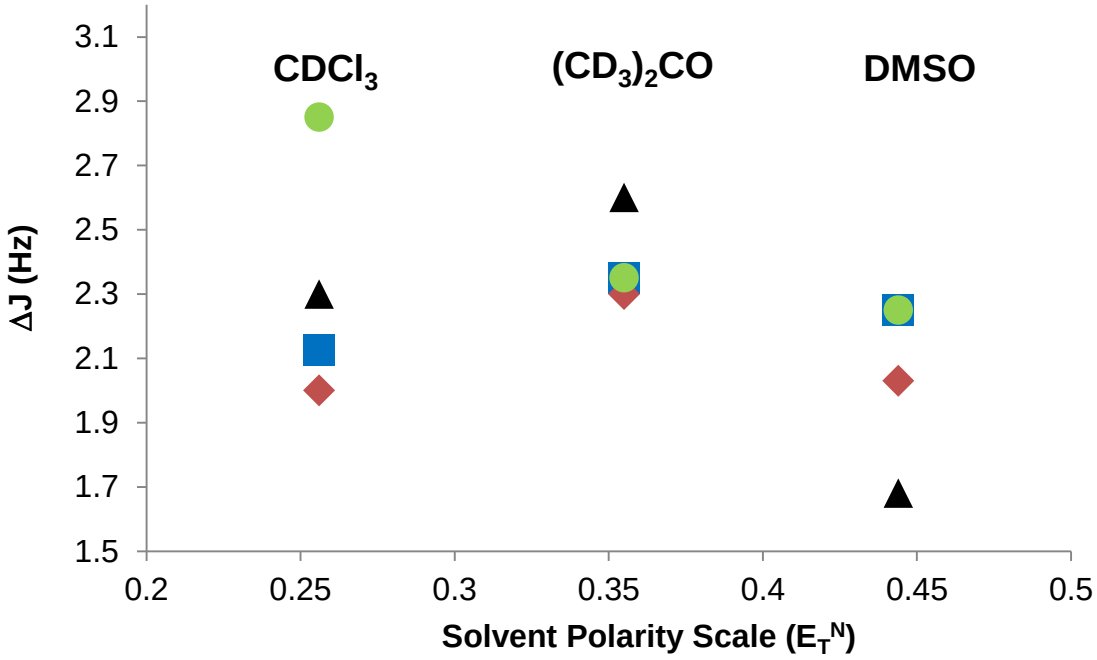

Figure 20. ΔJ vs Solvent Polarity Scale E_T^N for compounds **5-8**. **5** (green circle); **6** (red diamond); **7** (blue square); **8** (black triangle).

For compounds **1-4**, chemical shift correlations were difficult to assign (**Figures 21-24**). It can be observed that several proton chemical shifts are missing due second order coupling and possible concentration effects (**Figure 23**). Similar to compounds **5-8**, H_C is mostly affected by a change in polarity and combined effects from the donor and acceptor groups. Interestingly, for compounds **1-4**, the proton neighboring the acceptor is shifted upfield. This phenomenon can be explained due to the presence of the cyano group. The circulating π electrons within the triple bond induce a magnetic field that opposes the applied magnetic field. This opposing magnetic field induces H_F to resonate at a lower frequency, thus shifting it more upfield in comparison to the other olefinic protons.

The bond length alternation was calculated for compounds **1-4**. Coupling constants were difficult to discriminate, thus leading to inadequacies in determining overall bond length alternation. Compounds **1-4** shown best solubility in $CDCl_3$ and presented with low BLA values (**Table 3**). Typically, as the BLA decreases, an increase in conjugation is observed. However, due to low solubility and second-order coupling, DMSO-*d6* and acetone-*d6* prevented proton assignments and ground state electronic/structural speculations.

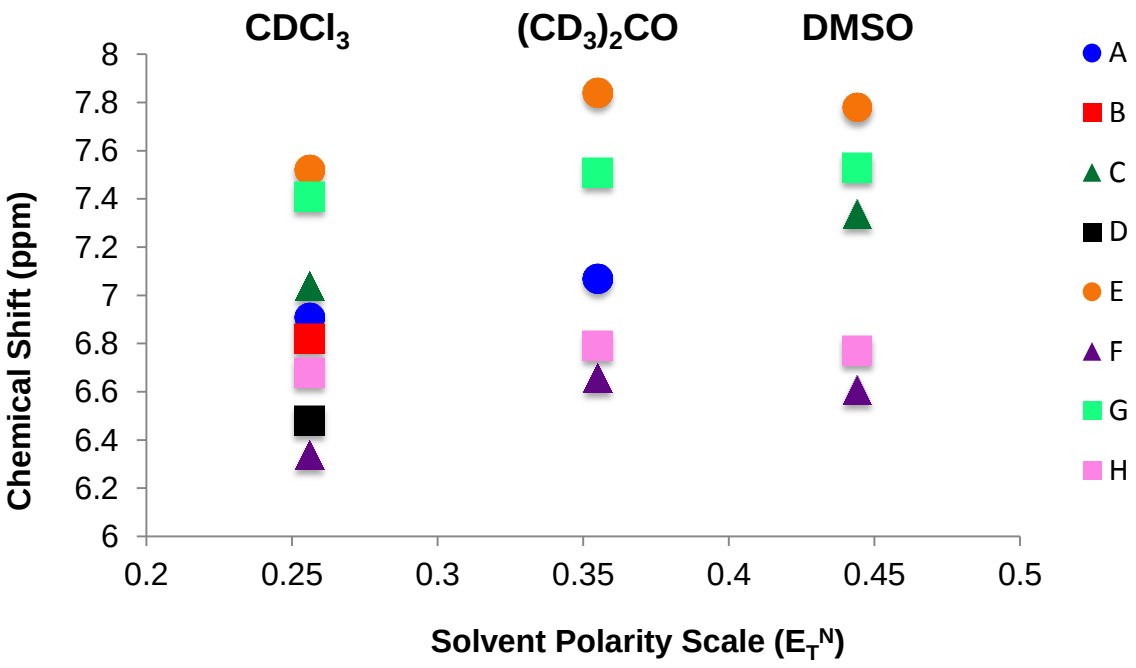

Figure 21. Chemical Shift (ppm) vs Solvent Polarity Scale (E_T^N) for compound **1**.

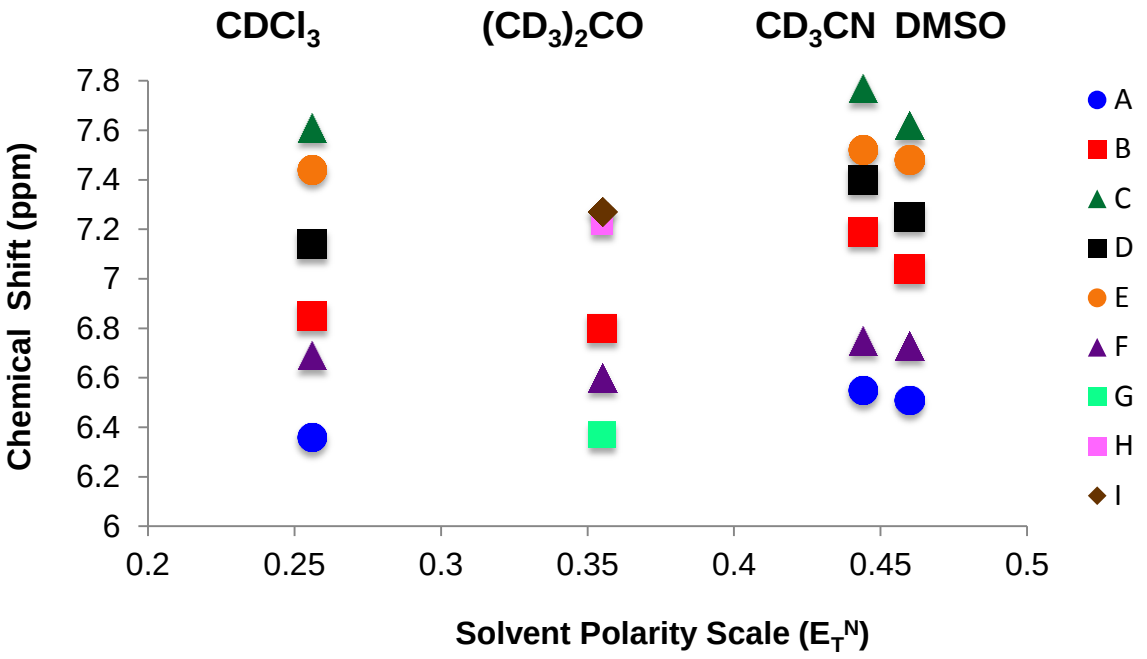

Figure 22. Chemical Shift (ppm) vs Solvent Polarity Scale (E_T^N) for compound **2**.

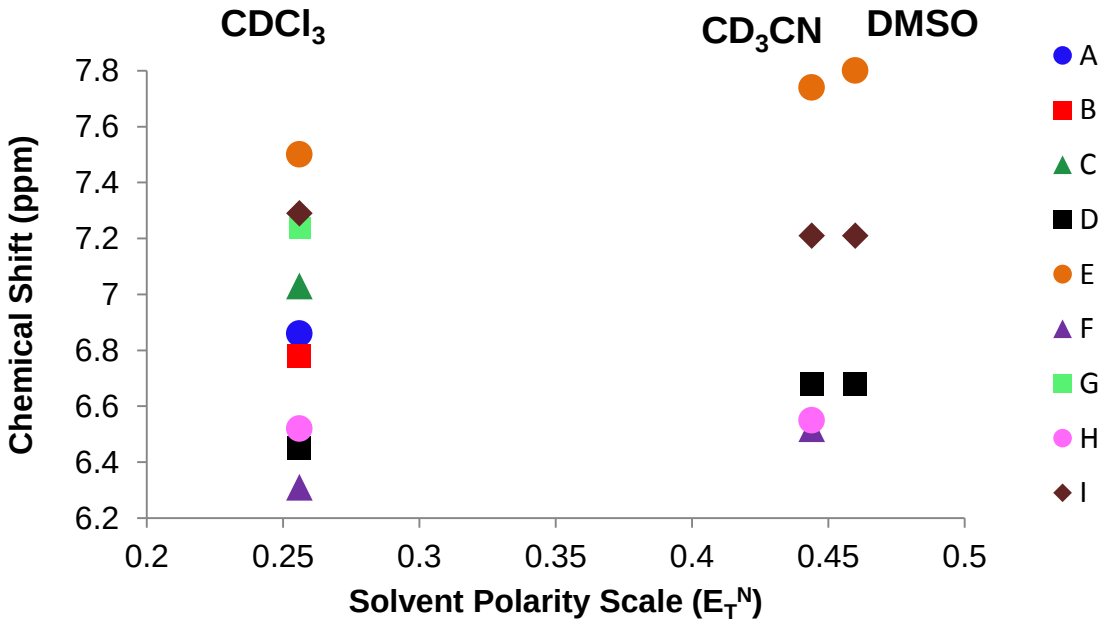

Figure 23. Chemical Shift (ppm) vs Solvent Polarity Scale (E_T^N) for compound **3**.

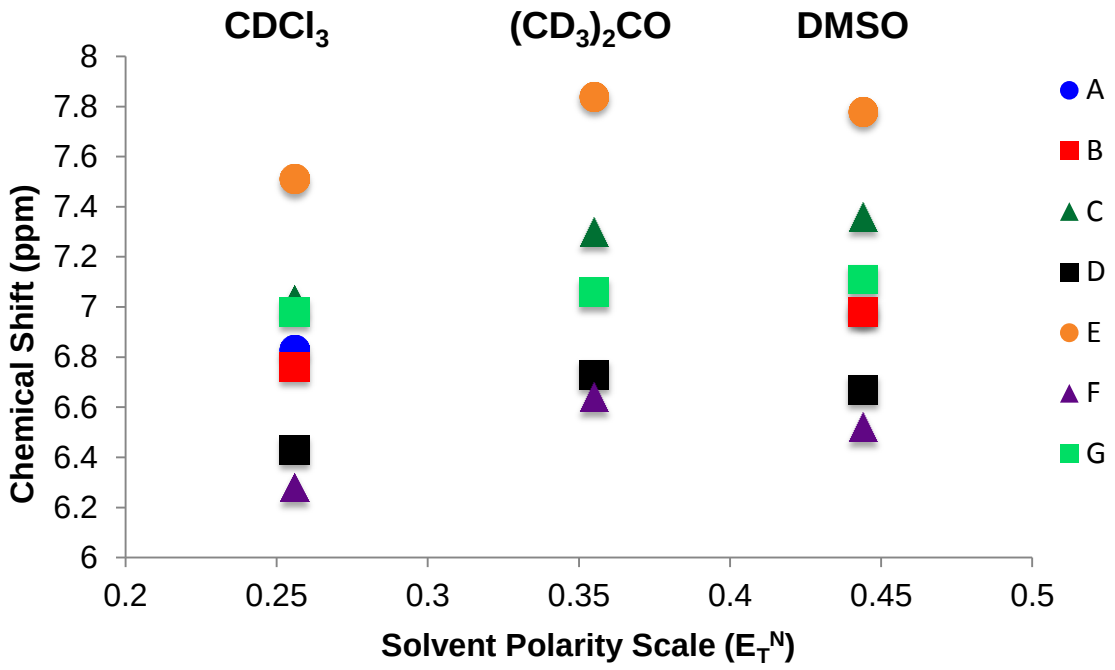

Figure 24. Chemical Shift (ppm) vs Solvent Polarity Scale (E_T^N) for compound **4**.

Table 3. Coupling Constants for Compounds **1-4** in $CDCl_3$.

	1	**2**	**3**	**4**
AB	15.5	14.9	14.9	14.9
BA	14.9	14.9	14.9	14.6
BC	10.9	11.4	10.9	10.6
CB	11.2	11.2	10.9	10.9
CD	14.0	14.0	13.8	14.4
DC	14.3	13.8	14.1	13.8
DE	11.4	11.5	11.8	11.5
ED	11.5	11.5	11.5	11.5
EF	14.9	14.9	15.4	14.9
FE	15.5	14.9	14.9	15.5
ΔJ	**3.6**	**3.2**	**3.4**	**3.6**

3.4.2 ^{13}C NMR Solvatochromism

^{13}C NMR has been used to determine solvatochromic effects.[18] ^{13}C NMR chemical shift assignments for compounds **1**-**8** are based on ChemDraw predictions and HSQC proton/carbon correlations. Due to poor solubility in most solvents, the effects of solvent polarity could not be analyzed. Compounds **1**-**8** shown reasonable solubility in chloroform-*d* and chemical shift measurements were taken to analyze differences within each series of dyes. To visualize chemical shift deviations, ^{13}C NMR chemical shifts for compounds **5**-**8** were plotted against compound **5** (**Figure 25**), setting compound **5** as the standard to determine deviations. The largest deviations are between C1, C2, and C6 for compounds **5**-**8**.

In **Figure 21**, compounds **6** and **7** show C2 falling under the trendline. These carbons are shared between benzene and heterocyclic rings, corresponding to lower chemical shifts. This trend is consistent with the mesomeric effect where C2 is affected by donating effects from nitrogen and the neighboring carbons in the cyclo-pentane/hexane ring. The "donation" of electron density results in more shielding of that carbon. The donating effects on C6 are similar to C2 but lack the effects from the additional ring, resulting in decreased electron density, deshielding, and higher chemical shifts (relative to compound **5**). The effects on C1 are consistent with electron density trends where C1 is electron deficient and deshielded. Interestingly, C1 for compound **6** appears to be the most electron deficient whereas compounds **7** and **8** are more electron rich. This would imply that compound **6** has the better donor. As the size of the corresponding heterocyclic ring increases, a slight increase in shielding is observed,

resulting in a drop below the trendline. In compound **8**, C2 and C6 present different trends compared to compounds **5-7**. Both C2 and C6 share the heterocylic and benzene rings and experience a slight deshielding effect. Additionally, it was observed that certain electronic effects induced C4 for compound **6** to stray from the trendline. This result is inconclusive. Similar trends for C1, C2, and C6 were observed in compounds **1-4**, containing the tricyanofuran acceptor (**Figure 26**). Also, C3 for compound **2** strays from the trendline. The deviation is assumed to be induced by some electron density effect but remains inconclusive.

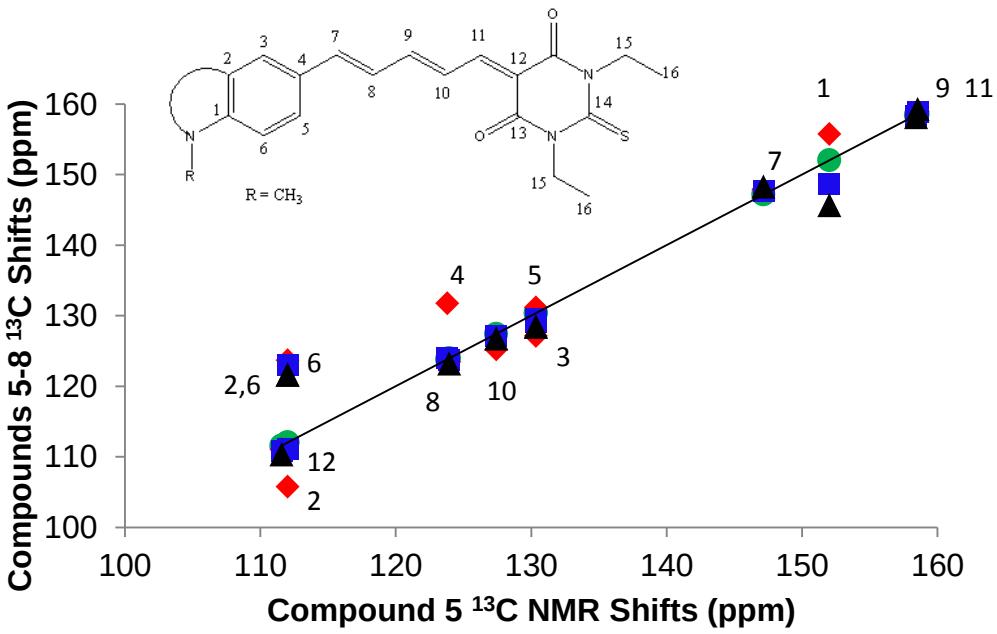

Figure 25. Compounds **5-8** ^{13}C NMR shifts (ppm) vs Compound **5** ^{13}C shifts (ppm). **5** (green circle); **6** (red diamond); **7** (blue square); **8** (black triangle). Top illustration represents carbon numbering system for thiobarbituric derivatives.

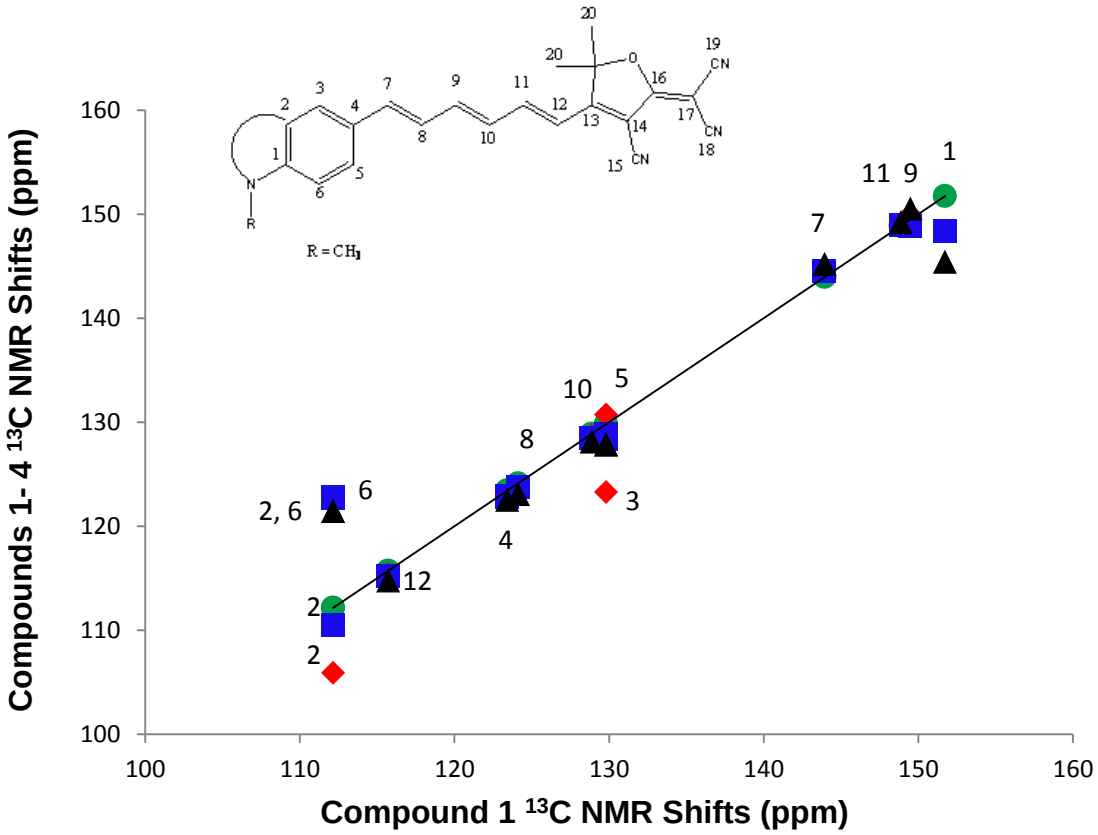

Figure 26. Compounds **1-4** ^{13}C shifts vs compounds **1** ^{13}C shifts. **1** (green circle); **2** (red diamond); **3** (blue square); **4** (black triangle). Top illustration represents carbon numbering system for tricyanofuran derivatives.

CHAPTER IV

CONCLUSIONS

Computational and spectroscopic studies were done to study the effects of the donor group geometries in D-π-A dyes. Based on **Table 1**, it can be seen that compounds **1** and **5** show structures that exhibit high freedom of rotation about the N-C_{sp2} axis, allowing sp^2 hybridization at the nitrogen atom and increased planarity. Conversely, compounds **2** and **6** showed less planarity due to restrictions caused by a higher level of ring strain. Presumably, this should result in a non-coplanar molecule with a lower level of conjugation and a possible decreased ICT band gap.

Solvatochromic trends were observed in the UV-Vis analysis for compounds **1**-**8**. It can be observed that compounds **5**-**8** exhibit positive solvatochromism, thus shifting λ_{max} to longer wavelengths as polarity increases (**Figure 11**). For compound **5**, positive solvatochromism occurred at shorter wavelengths, correlating to a lower ICT band gap between the ground and excited state. Compound **8** exhibited positive solvatochromism at longer wavelengths, correlating to a higher ICT band gap between the ground and excited state, and presented with the highest conjugation. Compounds **6**-**7** positive solvatochromic trend appeared to have similar ICT band gap energies. For compounds **1**-**4**, a different trend was observed. From **Figure 12**, it can be noted that the compounds do not follow the ideal trend for positive solvatochromism. However, solvents that were chlorinated, induced decomposition, or could hydrogen bond, were removed and resulted in positive solvatochromic (**Figure 13**). This would imply that compounds **1**-**4** are more

sensitive to the solvent environment and the solvent medium greatly affects the λ_{max}. The ΔS values for compounds **5-8** were relatively high measuring 108 nm for compound **6**, 96 nm for compound **7**, 86 nm for compound **8**, and 76 nm for compound **5**. Conversely, ΔS values were significantly lower for compounds **1-4** measuring 52 nm for compound **4**, 44 nm for compound **3**, 40 nm for compound **2**, and 36 nm for compound **1**.

Solvatochromism is observed throughout ^{1}H NMR for compounds **1**-**8**. The changes are minimal but show definite shifts. The protons nearest the donor region shift upfield whereas protons nearest the acceptor shift downfield. For compounds **1-8,** H_C seems to be the most affected by polarity of the solvent. It equals feels the "pushing" effects from the donor region as well as the "pulling" effects from the acceptor region. For compounds **5-8**, as the polarity of the solvent increases, ΔJ values decrease and conjugation increases. This suggests that the charge-separated form contributes to the ground state, resulting in increased conjugation. Compound **8** seems to have the most conjugation in the ground state. For compounds **1**-**4**, this conclusion cannot be made. Several coupling constants could not be determined as a result of poor solubility and second order coupling. Despite the inability to observe ^{13}C NMR solvatochromic trends, electronic characteristics were analyzed for compounds **1-8** to observe changes in chemical shifts. It was predicted that compounds **4** and **8** would be the best donors due to donation of electron density from alkyl substituents. However, chemical shift trends show compounds **2** and **6** having a more electron deficient C1, resulting in better donors. Overall, pyramidalization at nitrogen appears to increase donating ability and decrease

conjugation, contradicting previous computational speculations. However, the effects are too subtle to affect properties negatively.

LITERATURE CITED

1. Blanchard-Desce, M.; Alain, V.; Bedworth, P.V.; Marder, S.R.; Fort, A.; Runser, C.; Barzoukes, M.; Lebus, S.; Wortmann, R. Large Quadratic Hyperpolarizabilities and Donor-Acceptor Polyenes Exhibiting Optimum Bond Length Alternation: Correlation Between Structure and Hyperpolarizability. *Chem. Eur. J.* **1997,** *3*, 1091-1104.
2. Chen, H.; Mingying, M.; Lu, Q. Preparation of D-π-A Chromophores and Their Solvatochromisms. *Polycycl. Aromat. Comp.* **2013,** *33*, 289-296.
3. B.E.A. Saleh and M.C. Teich, *Fundamentals of Photonics*, Wiley, New York, 1991.
4. Long, N.J. Organometallic Compounds For Nonlinear Optics-The Search For En-light-enment! *Angew. Chem., Int. Ed. Engl.* **1995,** *34*, 21-38.
5. I.C. Khoo, *Liquid Crystals. Physical Properties and Nonlinear Optical Phenomena*, Wiley, New York. **1995**.
6. P.N. Prasad and D.J. Williams, *Introduction to Nonlinear Optical Effects in Molecules & Polymers*, Wiley, New York, **1991**.
7. Verbiest, T.; Houbrechts, S.; Kauramen, M.; Clays, Koen; Persoons, A. Second-order Nonlinear Optical Materials: Recent Advances In Chromophore Design. *J. Mater. Chem.* **1997,** *7*, 2175-2189.
8. Marder, S.R.; Cheng, L.; Tiemann, B.G.; Friedli, A.C.; Blanchard-Desce, M.; Perry J.W.; Skindhoj, J. Large First Hyperpolarizabilities In Push-Pull Polyenes

By Tuning of the Bond Length Alternation and Aromaticity. *Science* **1994,***263*, 511-514.

9. Grubbs, R.B.; Marder, S.R.; Perry, J.W. Second-Order Nonlinearities and Crystal Structure of 2-methoxy-4'-nitro-(*E*)-stilbene. *Chem. Mater.* **1991,** *3*, 3-4.
10. Gorman, C.B.; Marder, S.R. An Investigation of the Interrelationships Between Linear and Nonlinear Polarizabilities and Bond-Length Alternation in Conjugated Organic Molecules. *Proc. Natl. Acad. Sci.* **1993,** *90*, 11297-11301.
11. Marder, S.R.; Gorman, C.B.; Tiemann, B.G.; Cheng, L. Stronger Acceptors Can Diminish Nonlinear Optical Response in Simple Donor-Acceptor Polyenes. *J. Am. Chem. Soc.* **1993,** *115*, 3006-3007.
12. Bourhill, G.; Brédas, J.; Cheng, L.; Marder, S.R.; Meyers, F.; Perry, J.W.; Tiemann, B.G. Experimental Demonstration of the Dependence of the First Hyperpolarizability of Donor-Acceptor Substituted Polyenes on the Ground-State Polarization and Bond Length Alternation. *J. Am. Chem. Soc.* **1994,** *116*, 2619-2620.
13. Marder, S.R.; Gorman, C.B.; Meyers, F.; Perry, J.W.; Bourhill, G.; Brédas, J.; Pierce, B.M. A Unified Description of Linear and Nonlinear Polarization in Organic Polymethine Dyes. *Science* **1994,** *265*, 632-635.
14. Risser, S.M.; Beratan, D.N.; Marder, S.R. Structure-Function Relationships For β, the First Molecular Hyperpolarizability. *J. Am. Chem. Soc.* **1993,** *115*, 7719-7728.
15. Barzoukas, M.; Fort, A.; Blanchard-Desce, M. Quadratic Hyperpolarizability of Push-Pull Polyenes: A Two-Form Analysis of the Length Effect. *Synthetic Metals*. **1996,** *83*, 277-280.

16. Meyers, F.; Marder, S.R.; Pierce, B.M.; Bredas, J.L. Electric Field Modulated Nonlinear Optical Properties of Donor-Acceptor Polyenes: Sum-Over-States Investigation of the Relationship Between Molecular Polarizabilities (α, β, and γ) and Bond Length Alternation. *J. Am. Chem. Soc.* **1994,** 116, 10703-10714.
17. Gorman, C.B.; Marder, S.R. Effect of Molecular Polarization on Bond-Length Alternation, Linear Polarizability, First and Second Hyperpolarizability in Donor-Acceptor Polyenes as a Function of Chain Length. *Chem. Mat.* **1995,** *7*, 215-220.
18. Albert, I.D.L; Marks, T.J.; Ratner, M.A. Rational Design of Molecules with Large Hyperpolarizabilities. Electric Field, Solvent Polarity, and Bond Length Alternation Effects on Merocyanine Dye Linear and Nonlinear Optical Properties. *J. Phys. Chem.* **1996,** *100*, 9714-9725.
19. Reichardt, C. Solvatochromic Dyes as Solvent Polarity Indicators. *Chem. Rev.* **1994,** *94*, 2319-2358.
20. Greco, P.F. Part I. Synthesis and Characterization of Donor-π-Acceptor Compounds with Pentedienyl-Bridged Indoline and Tetrahyroquioline Donors and Aldehyde and Thiobarbituric Acid Acceptors Part II. Longitudinal Study Comparing Online Versus Face-To-Face Course Delivery in Introductory Chemistry. D.A. Dissertation, Middle Tennessee State University, Murfreesboro, TN, **2012**.
21. Gottlieb, H.E.; Kotlyar, V.; Nudelman, A. NMR Chemical Shifts of Common Laboratory Solvents as Trace Impurities. *J. Org. Chem.* **1997,** *62*, 7512-7515.

22. Friedli, A. C.; Yang, E.; Marder, S. R. A Convenient Synthetic Entry Into Aldehydes with Extended Conjugation. *Tetrahedron* **1997,** *53*, 2717-2730.

23. Gopalan, P.; Katz, H.; McGee, D. J.; Erben, C.; Zielinski, T.; Bousquet, D.; Muller, D.; Grazul, J.; Olsseon, Y. Star-Shaped Azo-Based Dipolar Chromophores: Design, Synthesis, Matrix Compatibility, and Electro-Optic Activity. *J. Am. Chem. Soc.* **2004,** *126*, 1741-1747.

24. Villemin, D.; Liao, L. Rapid and Efficient Synthesis of 2-[3-Cyano-4-(2-aryliden)-5,5-dimethyl-5H-furan-2-ylidene]-malononitrile Ender Focused Microwave Irradiation. *Synthetic Commun.* **2001,** *31*, 1771-1780.

25. Isborn, C.; Leclercq, A.; Villa, F.; Dalton, L.; Bredas, J.; Eichinger, B.; Robinson, B. Comparison of Static First Hyperpolarizabilities Calculated with Various Quantum Mechanical Methods. *J. Phys. Chem.* **2007**, *111*, 1319-1327.

26. Katayama, H.; Ohkoshi, M.; Kaneko, K. Amino-Claisen Rearrangement. IV. Quaternary Amino-ClaisenRerrangement of N-Allyljulolidium Derivatives. *Chem. Pharm. Bull.* **1984**, *32*, 1770-1778.

27. Garin, J.; Orduna, J.; Ruperez, J.I.; Alcala, R.; Villacampa, B.; Sanchez, C.; Martin, N.; Segura, J.L.; Gonzalez, M. Second-Order Nonlinear Optical Properties of Tetrathiafulvalene-π-(thio)barbituric Acid Chromophores. *Tetrahedron Lett.* **1998,** *39*, 3577-3580.

PART II. EFFECTS OF VINYLTRIMETHOXYSILANE ON BONE GROWTH TEMPLATES

CHAPTER I

INTRODUCTION

1.1Bioceramics

Bone is one of the most utilized materials in today's world of graft transplantations. Nearly 2.2 million bone graft operations are annually conducted in order to repair bone defects in orthopedic and dental surgeries.[1] Currently, bone grafts are commonly performed utilizing autografts. An autograft excises a portion of bone from either the iliac crest or the tibia. However, due to the limitation of tissue samples and death of tissue, biosynthetic graft materials are increasingly becoming a topic of interest.[2] Over the past decade, a sudden increase in applications within biomaterial science has birthed several ideas applicable to bone implantation/regeneration. Several techniques have been analyzed to mimic natural bone healing processes and mitigate the effects of bone degenerative pathologies (e.g. osteoporosis).

To promote bone healing with synthetic materials, a thorough understanding of bone and its mechanics are required. The synthesis of bone is an intricate process and remains a challenge to scientists. Its series of convoluted biomineralization reactions give rise to an organic/inorganic hybrid that provides bone with exceptional flexibility and mechanical properties. Bone consists of two main layers: cortical (hard) and cancellous (spongy) bone. Cortical bone is very dense and surrounds the trabecular bone (Figure 1). The cancellous bone is a highly porous honeycombed network that serves as an environment for specific cells, osteoblasts and osteoclasts. Osteoblasts are cells that

create new bone whereas osteoclasts break up old bone. Both cell types work in concert to maintain a natural bone building/resorption homeostasis.[13]

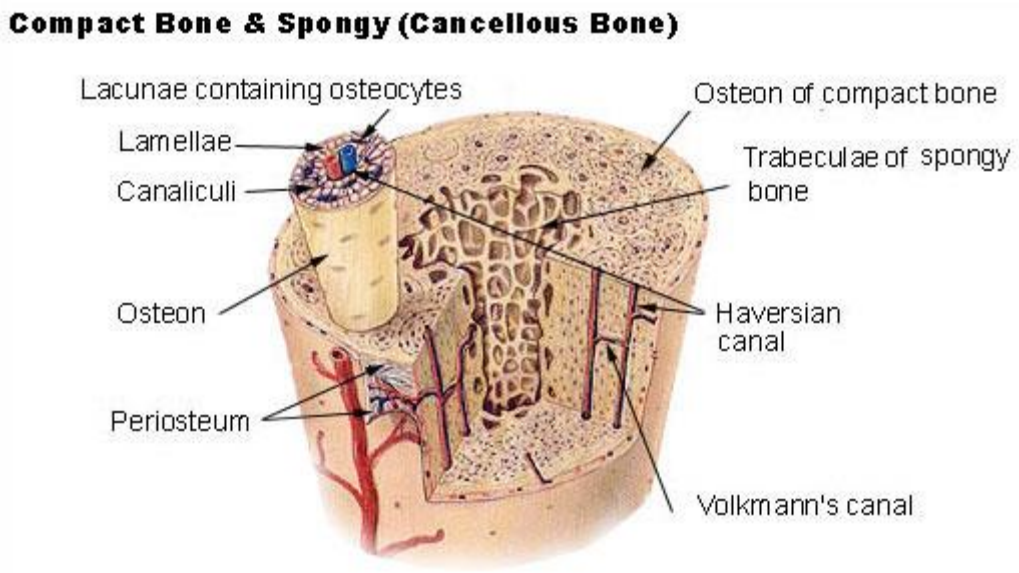

Figure 1. Illustration of compact and cancellous bone.[13]

The cortical and cancellous regions are typically formed in a lamellar pattern. Collagen fibrils are laid down in alternating patterns while inorganic nano-composites are incorporated to produce a hard surface.[3] The organic and inorganic combination patterning is not fully understood and remains to be analyzed.

Typically, bone is composed of 50-70 % mineral and 20-40 % organic matrix as well as other ingredients (e.g. water, lipids, etc.).[4] The mineral component of bone is mostly hydroxyapatite [$Ca_{10}(PO_4)_6(OH)_2$] where the crystals are a maximum of 200 Å

long.[4] Ultimately, the mineral portion of bone provides the mechanical rigidity and load-bearing strength while the organic portion contributes elasticity and flexibility.[4] Scientists specializing in the fields of material science and bioengineering have collaborated with biologists and chemists to design complex materials suitable for implants. One material that has been highly investigated for bone repair is ceramics. Ceramics have a structure similar to natural bone and include materials like oxides, phosphates, carbonates, nitrides, carbides, and glasses.[5] When ceramics are utilized to bind to tissues, these materials are termed bioceramics. Silica-based bioceramics are highly biocompatible and one of the most interesting targets for future implants.[5]

Bioceramics can be categorized into three groups, the first being the inert bioceramics. Inert bioceramics were claimed as the "First-generation" ceramics that would serve as an ideal implant for architectural purposes. However, due to their ability to "elicit a foreign body reaction ultimately causing aseptic loss of the implant" [6], first generation bioceramics quickly fell by the wayside. As a result, further research lead to the development of second-generation bioceramics. Such materials are devoted to forming an implant that is biodegradable as well as bioactive. The silica-based second-generation bioceramics mimic several natural properties including osteoinduction and osteoconduction. Osteoinduction is the process where "…undifferentiated and pluripotent cells are somehow stimulated to develop into the bone-forming cell lineage."[7] Osteoconduction is a surface that "…permits bone growth on its surface or down into pores, channels, or pipes."[7] These properties allow them to elicit specific functions for a given amount of time as well as allow the material to degrade and be resorbed. A

drawback to these ceramics is rate of degradation. When exposed to the extracellular fluid, second-generation bioceramics degrade in an unregulated fashion and result in further surgeries to repair the implant. Also, these materials have a small surface area, limiting the total area for bone growth to occur. Finally, the evolution of different ceramics has lead to the creation of more advanced ceramics, third-generation bioceramics. The concept behind such materials is that they should be highly porous (resembling spongy bone), maintain a high level of biocompatibility, be osteoconductive and osteoinductive, provide a high level of mechanical strength, and encourage osteogenesis. Osteogenesis is the process of inducing cellular gene transcription to cause further differentiation and proliferation. Thus, inducing cells to migrate into the implant, proliferate, and regenerate new bone (versus replacing bone).[3,7] Apart from inducing a cellular response, a major advantage of third generation bioceramics is the high porosity, interconnected pores, and increased surface area. High porosity and interconnected pores allow for ingrowths of neovasculatization and increased cellular colonization.[8] To obtain such qualities, scaffolds should be synthesized form 20-1000 μm pores.[15]

1.2 Bioactive Sol-gels

Since osteogenic factors are biomolecules, different methods of preparing ceramic scaffolds must be developed. Typically, ceramics are processed at very high temperatures. High temperatures denature the osteogenic biomolecules and lead to decreased functionality. One method for processing ceramics at lower temperatures as well as incorporating osteogenic factors is the sol-gel process. Sol-gel chemistry is a biphasic wet chemical process utilized to create ceramics. It begins as a liquid and

eventually evolves into a gel-like state. Sol-gels are colloidal solutions that several ingredients, including an alkoxide (e.g. tetraethyl orthosilicate, TEOS) that provides the ceramic structure. After being synthesized, the sol-gel will air-dry on a substrate through evaporation-induced self-assembly (EISA). This allows for solvent to evaporate and further condense the sol-gel. Finally, the sol can be sintered at lower temperatures (<1000 °C), heated for approximately 24 hours, and produce a ceramic solid.

1.3 Sol-gel Reaction

In a typical sol-gel reaction with TEOS, the alkoxide readily reacts with water to hydrolyze the ethoxy group and produce hydroxylated side chains. By introducing a catalyst (acidic or basic), TEOS will completely be hydrolyzed, resulting in four functional hydroxyl groups. Next, two hydroxy side chains will link together through a condensation reaction to produce siloxane groups (R-Si-O-Si-R). Since TEOS is tetra-functional, it can fully polymerize to form a branched network of silicon/oxygen bonds (Figure 2).

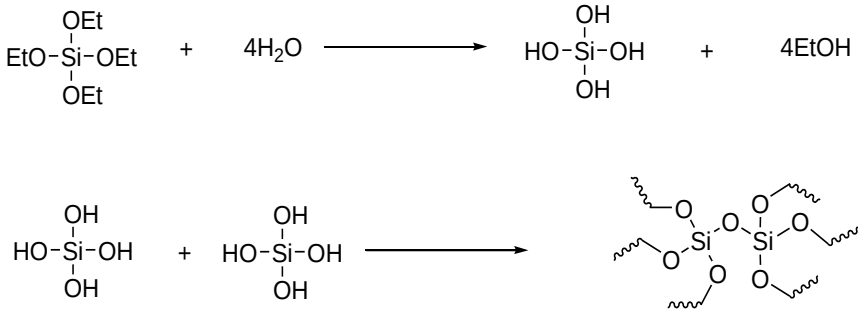

Figure 2. Reaction of TEOS and H_2O to form a polymer via the sol-gel process.

To regulate branching patterns, a templating agent is added to the sol-gel to direct the formation of mesopores within the ceramic. Mesopores are helpful in providing microenvironments for osteogenic factors as well as increasing the surface area to maximize implant / cellular interactions. Typically a non-ionic block co-polymer (e.g. F127) is utilized as a mesopore template. This co-polymer prevents interactions between the polymer and ionic compounds (e.g. calcium and phosphate ions). The templating agent forms micelles, causing the alkoxide to branch along the surface of the micelles (**Figure 3**). Once the sol-gel has been furnace treated, the non-ionic block co-polymer is burned out, leaving an inorganic scaffold with mesopores.

For bone regeneration applications, a series of techniques are utilized to alter the sol-gel and form an implant that closely resembles natural bone. For instance, ions like calcium and phosphorous have been incorporated for proper implant adhesion and induction of cellular responses. It was discovered that these ions contribute interesting properties to the mesoporous silicate. First, calcium acts as a network modifier [8] to cleave the covalent bond between silicon and oxygen and form calcium oxide bonds. The network modifier destabilizes the network, increases reactivity, and gives the ceramic bioactive behavior. When the scaffold is exposed to the extracellular fluid, an ion exchange occurs between the glass and a proton from the extracellular matrix.[9] At the same time, the siloxane groups are broken to form silanol groups, ultimately forming the tetrafunctional $Si(OH)_4$ silanol groups. The silanol groups can proceed to repolymerize to form a network of silica on the top surface of the implant.[10] Finally, the calcium and phosphorous ions migrate to the top of the scaffold surface and precipitate

out, forming an amorphous Ca-P_2O_5 layer on the surface of the silica layer.[9] The amorphous layer tends to incorporate hydroxyl and carbonate anions from the extracellular fluid and crystallize to form the hydroxylcarbonate apatite layer (HCA).[9] This layer allows the scaffold to bind to the tissue.

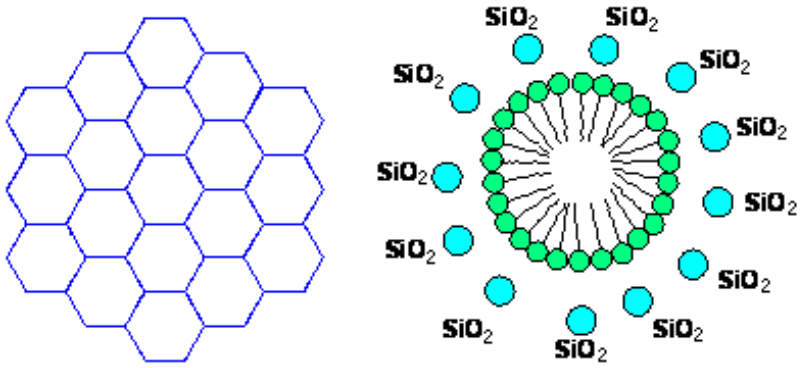

Figure 3. Illustration of calcium concentration effects.[10,11] Hexagonal mesopores (left) are the product of increased Ca^{2+} concentrations and micelle formation induced by templating agent.

Also, the amount of calcium incorporated into the matrix will affect the overall mesopores that are created within the scaffold. It was proven that increased concentrations of Ca^{2+} ions found in the extracellular matrix will lead to the increased micelle curvature of the non-ionic block co-polymer, consequently producing hexagonal mesopores (**Figure 3**).[10,11]

1.4 Sol-Gel Substrates

To create a scaffold that possesses high porosity, interconnected pores, and specified pore lengths, scientists have analyzed several techniques useful in designing materials that fulfill these requirements. When creating such materials, one needs to be mindful of the macrostructure and microstructure. One way of synthesizing these materials is through rapid prototyping methods. This methods is very useful in creating giant-sized pores (30 – 1000 μm) that are uniform and evenly spaced.[12] This method is very expensive and requires extreme precision. A simpler method is to use polyurethane foams (PUF) as templates.[12] This material is very cheap and user friendly. The PUF can be immersed into the sol-gel, air-dried, and then furnace treated. The organic foam is burned out and a porous inorganic scaffold is produced. PUF can be molded to fit any space, contain high porosity, and interconnected pores. The major disadvantage of using PUF is the lack of pore size regulation and shrinkage after being furnace treated (> 700 μm).[12]

1.5 Organic / Inorganic Hybrid Materials

A major drawback when using ceramics as biocompatible materials is their lack of mechanical strength. Natural bone possesses a high degree of mechanical strength and flexibility due to an intricate amalgamation of organic and inorganic components. Mesoporous silicates are thermally stable, although brittle materials. Organic polymers, although usually unstable at high temperature, provide flexibility. Currently, scientists are formulating innovative organic / inorganic hybrids to improve the overall mechanical

strength of synthetic bone materials. Vinyl trimethoxy silane (VTMS) is an example of an organic precursor that presumably could provide flexibility and strength to otherwise brittle mesoporous silicates. Vinyl groups possess the ability to crosslink with adjacent vinyl groups when activated by heat or UV exposure.

1.6 Research Goals

The goal of this research is incorporate both VTMS and TEOS into a sol-gel solution, coat a template sponge with sol-gel, expose the sol-coated sponge to UV light, burn out the sponge template with a furnace, and then characterize the scaffolds through scanning electron microscopy (SEM) (**Figure 4**),. Through characterization, the pore sizes can be measured to determine a change in pore thickness. This could produce a "stronger" scaffold. Once the scaffolds have proven to be strong enough to handle a stress test, the samples can be seeded with harvested bone cells and placed in a simulated environment similar to human bone.

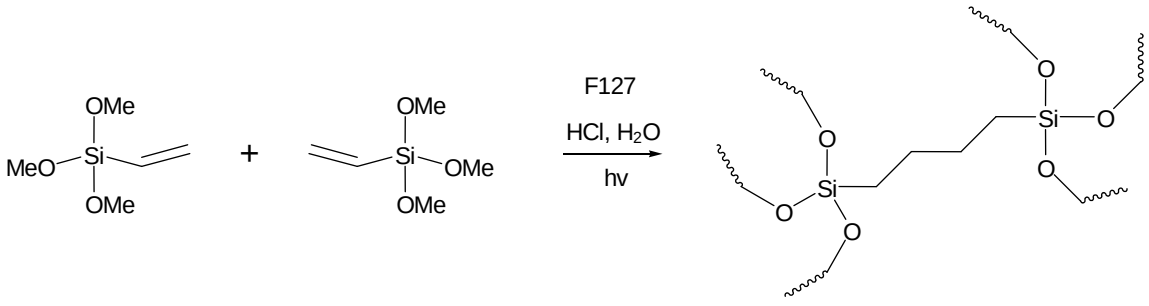

Figure 4. Illustration of VTMS Branching.

CHAPTER II

EXPERIMENTAL

To analyze the effect of incorporating VTMS, a series of sol-gel recipes were modified from literature.[12] The hypothesis was that VTMS should increase the strength of the mesoporous matrix. Ultimately, a strong synthetic scaffold was expected to result as the number of dips and VTMS concentration increased. Three different ratios of VTMS:TEOS were analyzed to determine an ideal VTMS concentration. Following the sol-gel synthesis, samples were placed into the sol-gel, compressed, and photochemically treated with a 450 W UV lamp to crosslink the vinyl side chains. The samples were further dipped, treated and allowed to air-dry. After air drying, the sponge template was furnace treated at 1°C / min to 350 °C, temperature held constant for an hour, increased to 700 °C at a rate of 1 °C / min, temperature held constant for an hour, and finally brought back to 25 °C. After furnace treating, the sponge was burnt out leaving a mold of the sample sponge. The ceramic scaffolds were analyzed using scanning electron microscopy (SEM). Cell wall sizes were measured using a computer software program *ImageJ*. [14] This program was useful in observing changes in the scaffold and seeing if VTMS contributed to the strength of the scaffold.

2.2 Instruments

Samples were analyzed with a Hitachi S-3400 Scanning Electron Microscope from the MTSU Interdisciplinary Microanalysis and Imaging Center (MIMIC). Samples were prepared by evaporating a thin layer of palladium/gold from a sputter coater. This

process was repeated a few times to guarantee sufficient coverage as well as to prevent possible charging. Also, MIMIC provided the program *Image J* for measuring pore sizes and pore cell walls.

2.2 Materials and Reagents

Pluronic® F-127 (F127) was purchased from Sigma Life Sciences. Ethyl Alcohol (EtOH) (200 proof, ACS/USP grade) was purchased from Pharmco-AAPER. tetraethyleorthosilicate (TEOS, 98%) and vinyltrimethoxysilane (VTMS, 97%) were purchased from Sigma Aldrich. Calcium nitrate tetrahydrate ($Ca(NO_3)_2{\cdot}4H_2O$, ≥99.0%) was purchased from Acros Organics. Triethyl phosphate (TEP, ≥99.0%) was purchased from Alfa Aesar. Hydrochloric acid (12.1 M) was purchased from EMD Chemical. The sponge material were Brillo® Estracell® scrub sponges purchased from Wal-Mart. The sponges displayed several desirable characteristics.

2.3 Synthesis

Si-O_2 sol gel containing $Ca(NO_3)_2{\cdot}4H_2O$ and triethyl phosphate (Control)[12]

The sol-gel was synthesized by mixing F127 (1.0 g, 0.079 mmol), $Ca(NO_3)_2.4H_2O$ (0.35g, 1.5 mmol), and ethanol (15.0 g, 0.33 mol) into a round bottom flask. Next, TEP (0.091 g, 0.5 mmol), TEOS, and 0.5M (0.25 g) HCl were added to complete the sol-gel recipe. The resulting solution was stirred and refluxed for one hour.

SiO_2 sol gel containing 0.1:1 (VTMS : TEOS)

The sol-gel was synthesized by mixing F127 (1.0 g, 0.079 mmol), $Ca(NO_3)_2.4H_2O$ (0.35

g, 1.5 mmol), and ethanol (15.0 g, 0.33 mol) into a round bottom flask. Next, a series of compounds were added including TEP (0.091 g, 0.5 mmol), TEOS (0.167 g, 0.80 mmol), VTMS (1.067 g, 0.72 mmol) and 0.5 M HCl (0.25 g). The resulting solution was stirred and refluxed for one hour.

SiO_2 sol gel containing 1:1 (VTMS : TEOS)

The sol-gel was synthesized by mixing F127 (1.0 g, 0.079 mmol), $Ca(NO_3)_2.4H_2O$ (0.35 g, 1.5 mmol), and ethanol (15.0 g, 0.33 mol) into a round bottom flask. Next, a series of compounds were added including TEP (0.091 g, 0.5 mmol), TEOS (0.835 g, 4.0 mmol), VTMS (0.592 g, 4.0 mmol) and 0.5 M HCl (0.25 g). The resulting solution was stirred and refluxed for one hour.

SiO_2 sol gel containing 1:0.1 (VTMS : TEOS)

The sol-gel was synthesized by mixing F127 (1.0 g, 0.079 mmol), $Ca(NO_3)_2.4H_2O$ (0.35 g, 1.5 mmol), and ethanol (15.0 g, 0.33 mol) into a round bottom flask. Next, a series compounds were added including TEP (0.091 g, 0.5 mmol), TEOS (1.50 g, 7.2 mmol), VTMS (0.119 g, 0.80 mmol) and 0.5M HCl (0.25 g). The resulting solution was stirred and refluxed for one hour.

CHAPTER III

RESULTS AND DISCUSSION

To determine the ideal VTMS concentration, several factors were analyzed. Aside from the VTMS concentration, drying intervals, photochemical exposure, and dipping times were taken into consideration. Initially, samples were allowed to dry from 1- 6 hours between dips, and one sample was dried for for twelve hours between dips. A two hour drying period was determined to be a reasonable compromise that allowed more layers (to decrease brittleness), and efficient time use (to move the project forward).

After each drying time, the samples were placed in a photochemical box for UV exposure. Samples were positioned on a glass side approximately 10 cm away from the UV lamp source. Initially, the exposure time was set to 10 minutes. The samples were turned over and treated with an additional ten minutes of exposure (to irradiate every side). This amount of exposure time was too much and caused minimal charring on the foam. To prevent the charring, the sample was exposed for five minutes, turned over, and exposed for an additional five minutes.

It was found that the varying ratios of VTMS concentrations showed minimal structural changes. Based off the structural integrity, it was concluded that the 1:1 VTMS:TEOS ratio would be best suited for further experiments. Concurrently, it was decided that the minimal number of dips resulted in incomplete/brittle scaffolds and required further experimentation. A control sample containing no VTMS was synthesized and compared against the the 1:1 ratio. Initially, the samples were dipped

from 1-6 dips and increased to 6-12 dips. Each set of dips included a control (**Figure 5**) and VTMS treated sample (**Figure** 6). Figures **5-12** illustrate a statisical measurement for average cell wall thickness as determined by measurements of cell wall thickness using *ImageJ* [14] computer software. To visualize the control and VTMS treated samples, SEM images were taken and paired with corresponding histograms. It can be determined that as the number of dips increase, pore thicknesses tend to remain the same. The histograms illustrate an average cell wall thickness ranging from 40-50 μm (**Table 1**). The structural characteristics of each cell wall became more defined and complete as the dips increase (**Figure 12)**. However, the scaffold completeness was not consistent throughout the scaffold and several regions presented with incomplete pore formation. The increase in dipping shown minimal improvements between the control and VTMS treated samples. Ultimately, scaffolds maintained their brittle characteristics and failed to improve the overall strength of the scaffold. It can be concluded that further investigation is required to understand the nature of the brittleness. It has been speculated that the hollowness of the scaffold after the foam has been burned out contributes to the overall lack of strength. Also, possible dissolving of dried sol-gel during the reapplication process could affect the number of layers actually drying on the surface of the foam. Once the foam has been burned out, an insufficient number of layers could produce areas of decreased structural integrity, resulting in a collapse in the pore walls. Additionally, an energy-dispersive X-ray (EDX) analysis was done to determine the distribution of calcium and phosphorous throughout the scaffold template. It was confirmed that the ions were equally distributed throughout each pore.

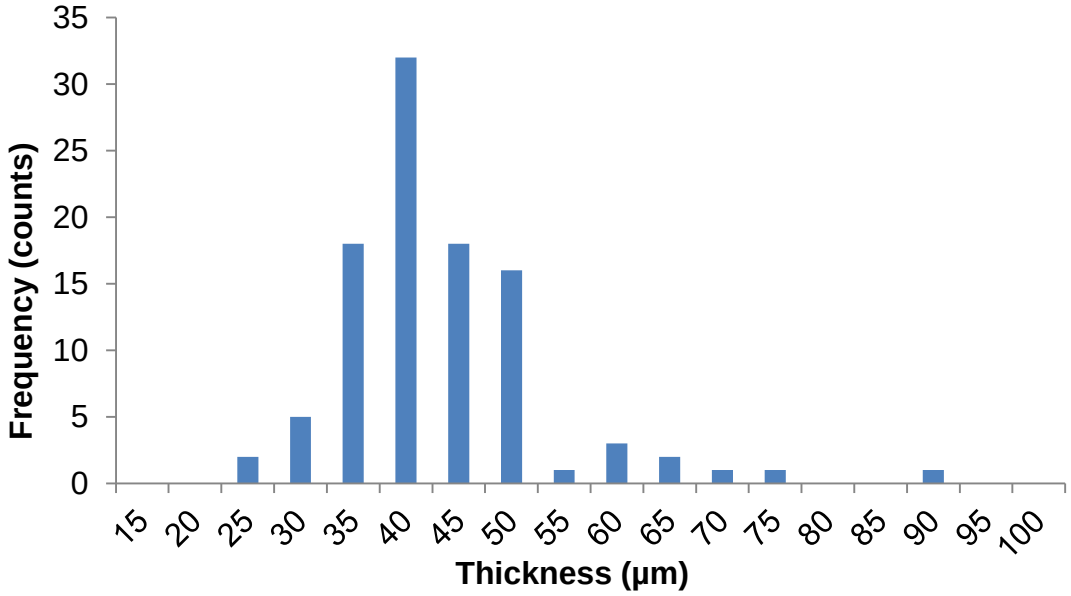

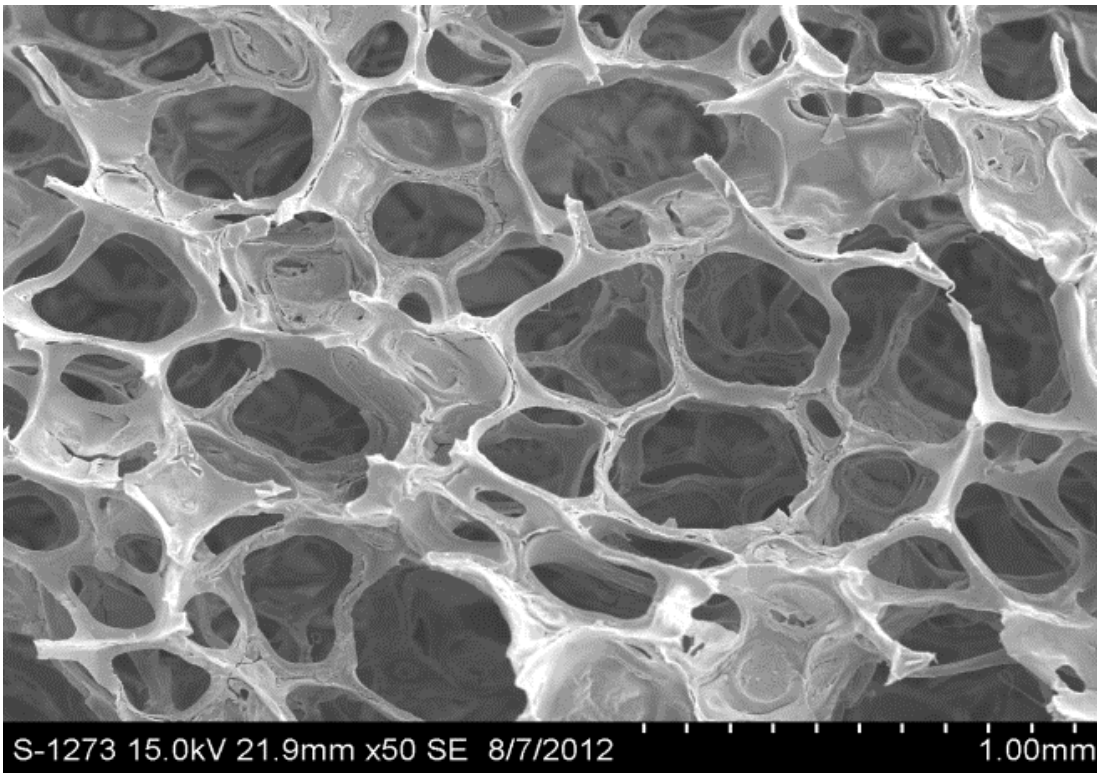

Figure 5. Control sample 6 (CS6) with corresponding SEM image.

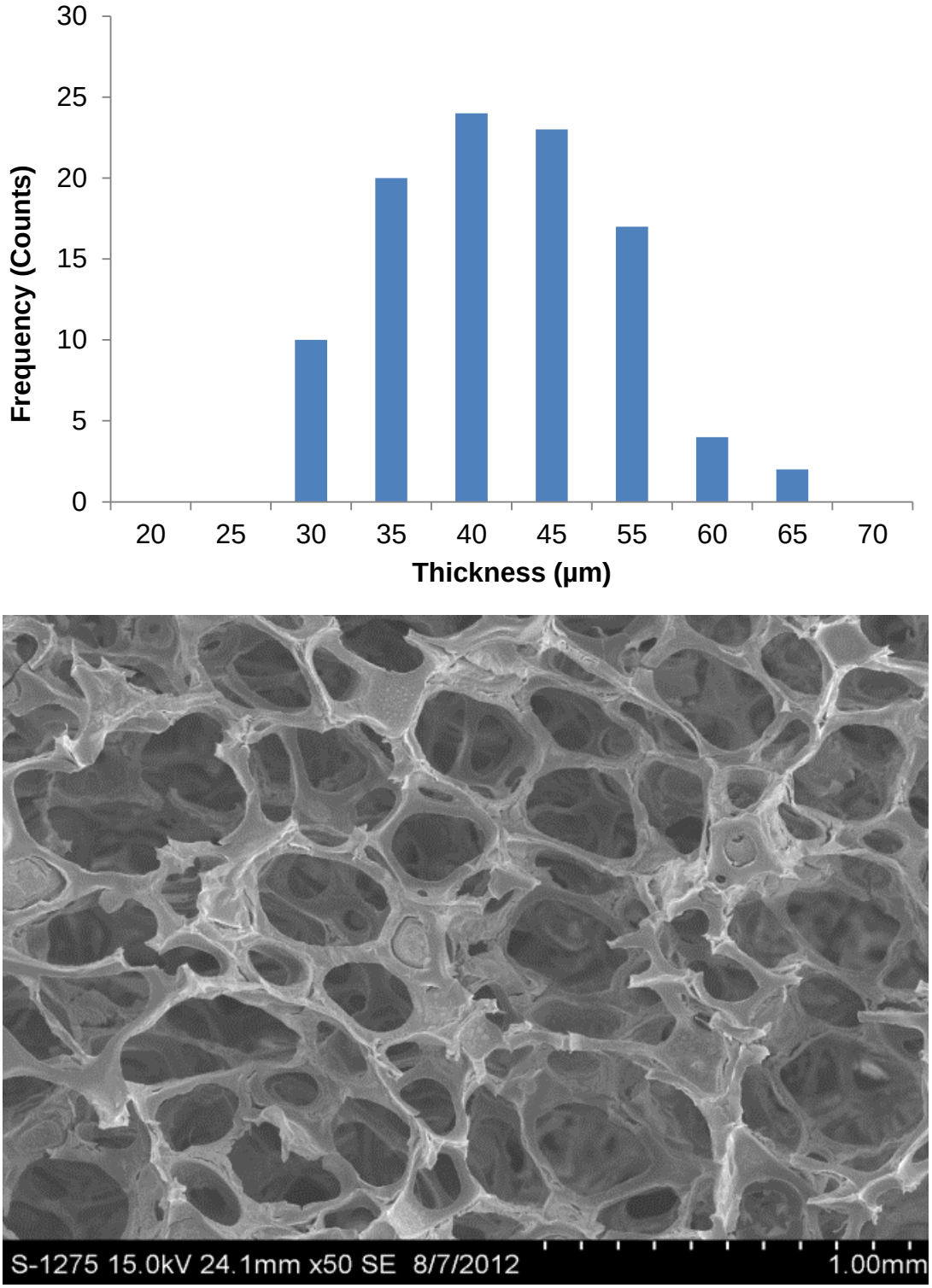

Figure 6. VTMS sample 6 (VS6) with corresponding SEM image.

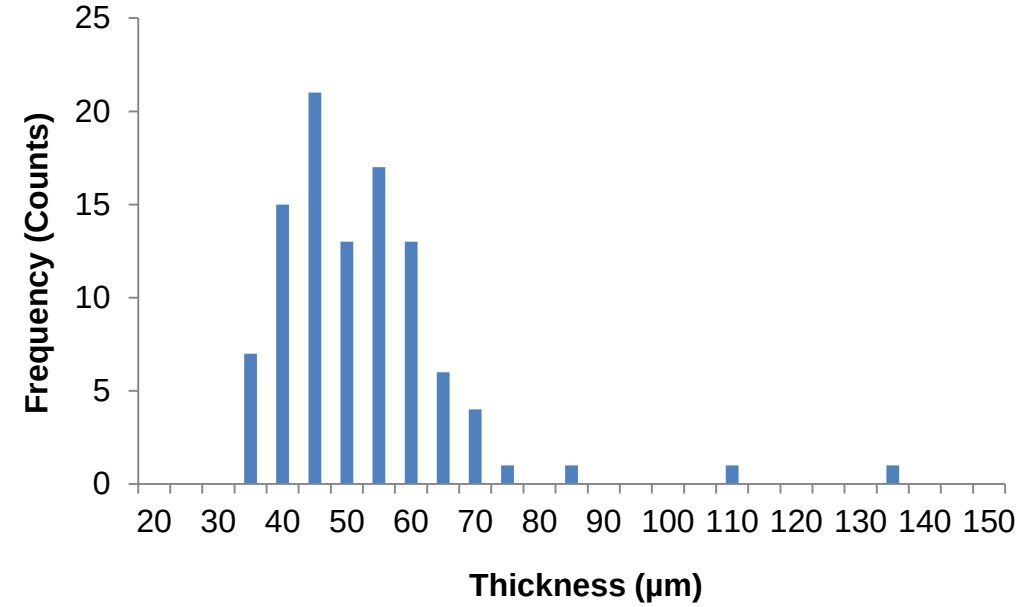

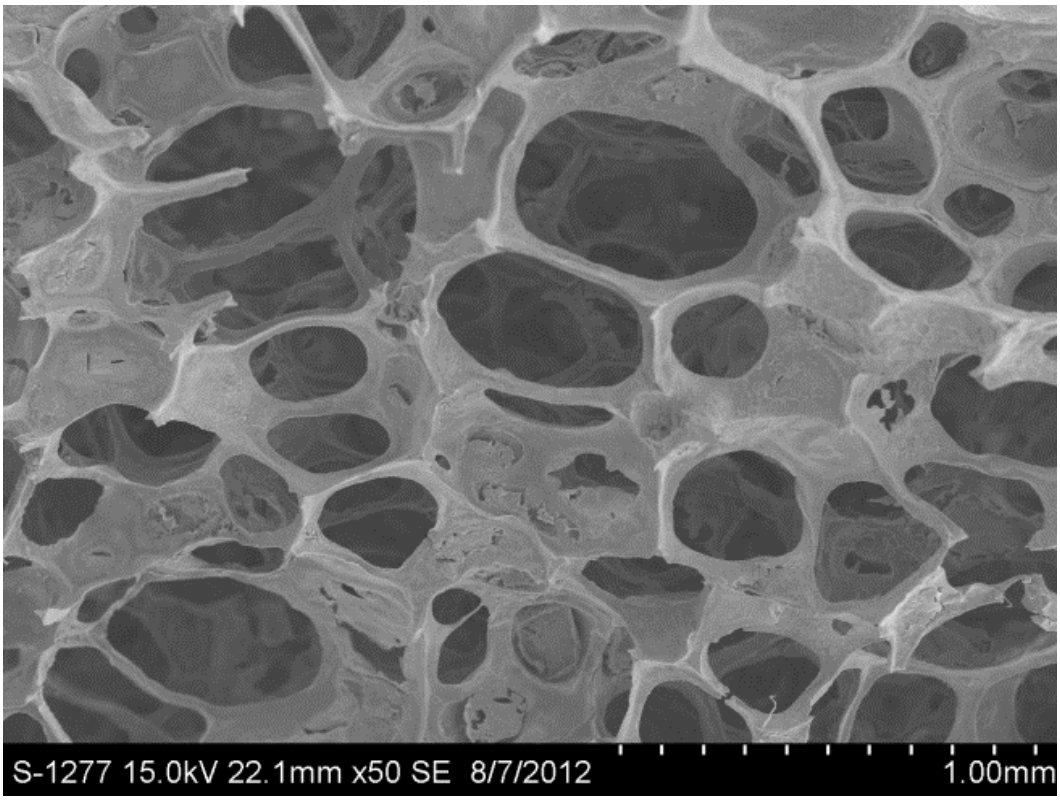

Figure 7. Control sample 8 (CS8) with corresponding SEM image.

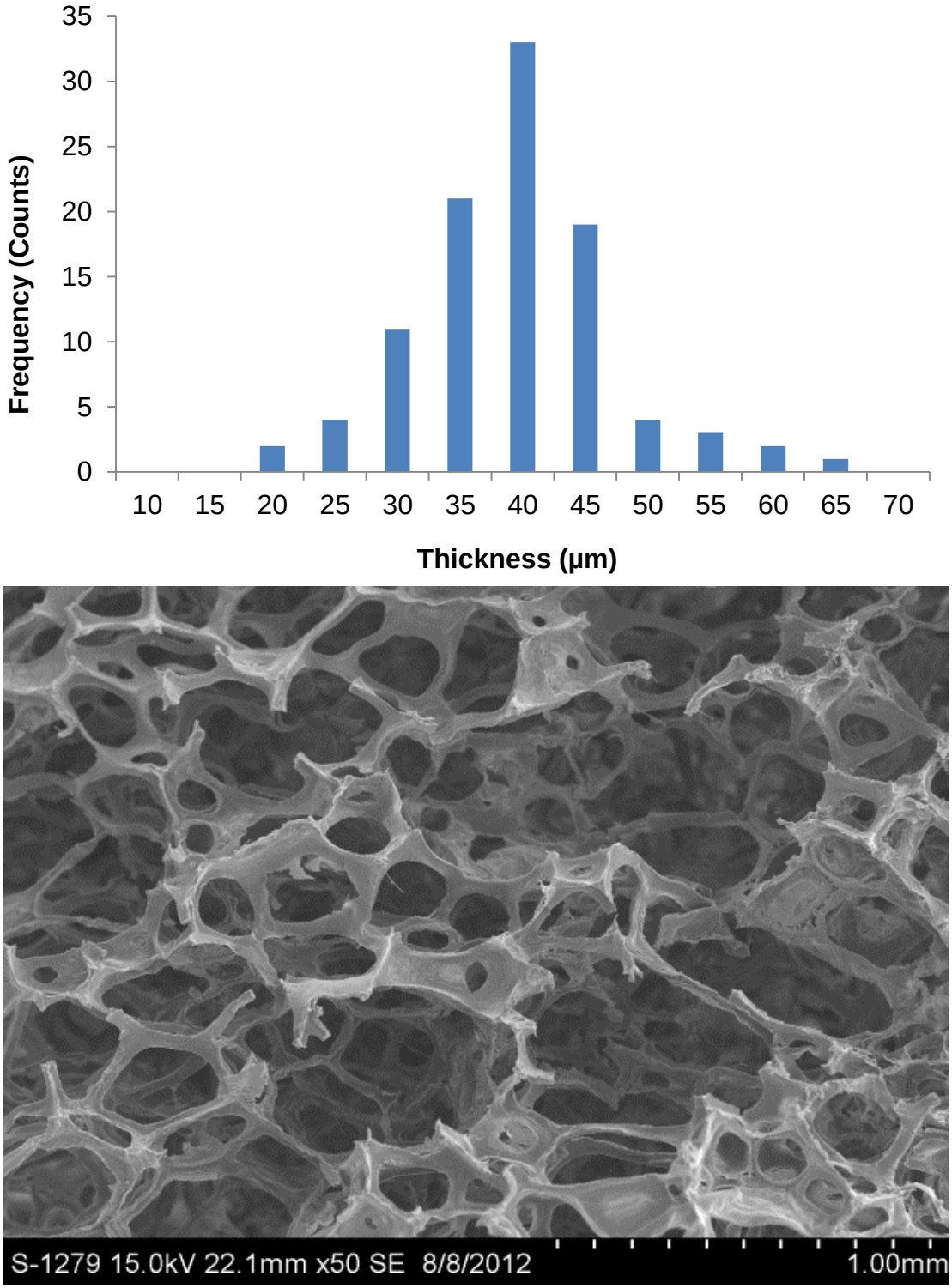

Figure 8. VTMS sample 8 (VS8) with corresponding SEM image.

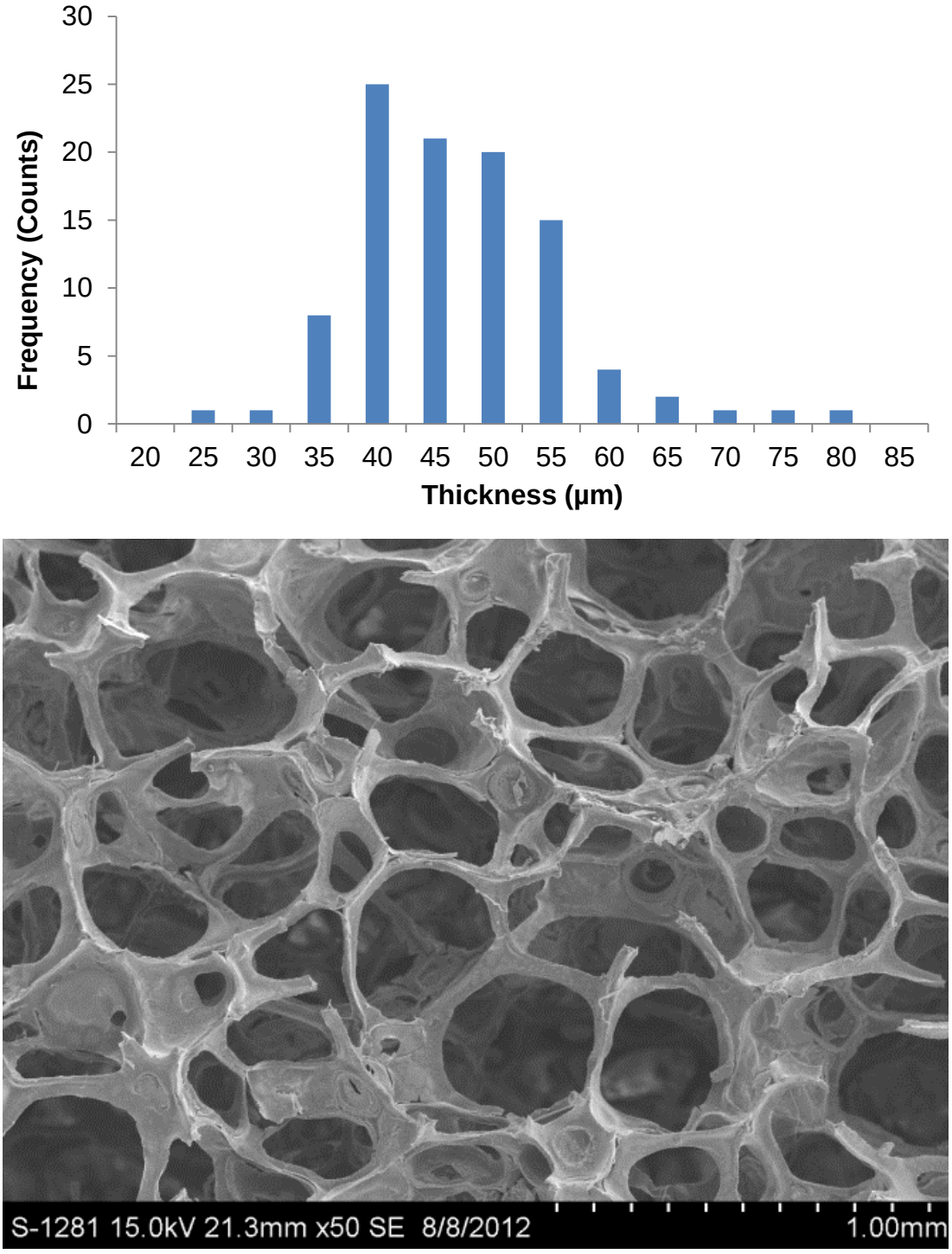

Figure 9. Control sample 10 (CS10) with corresponding SEM image.

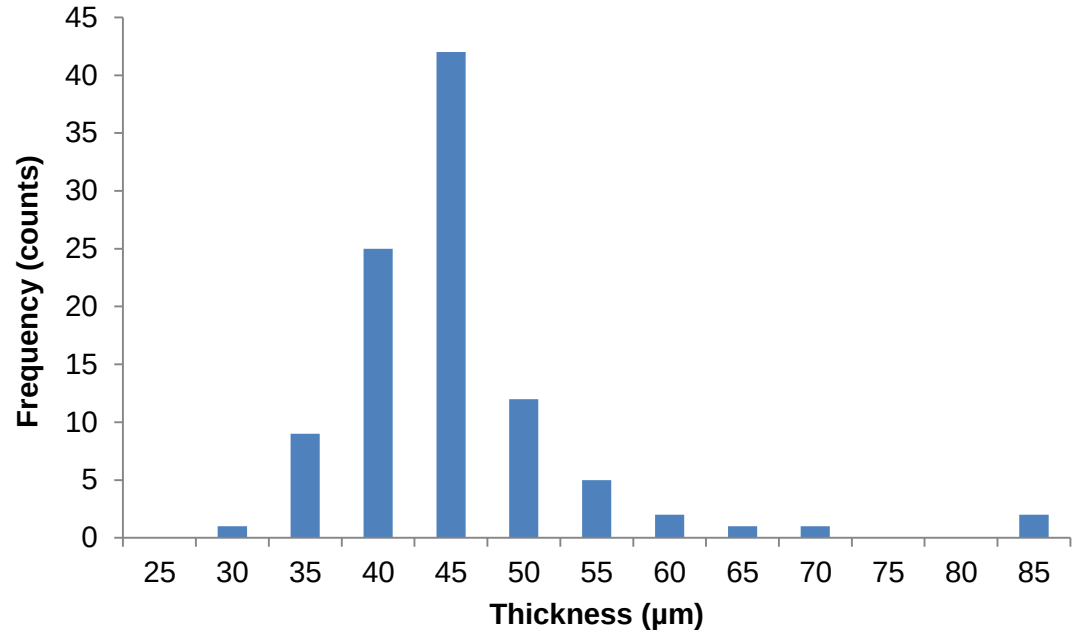

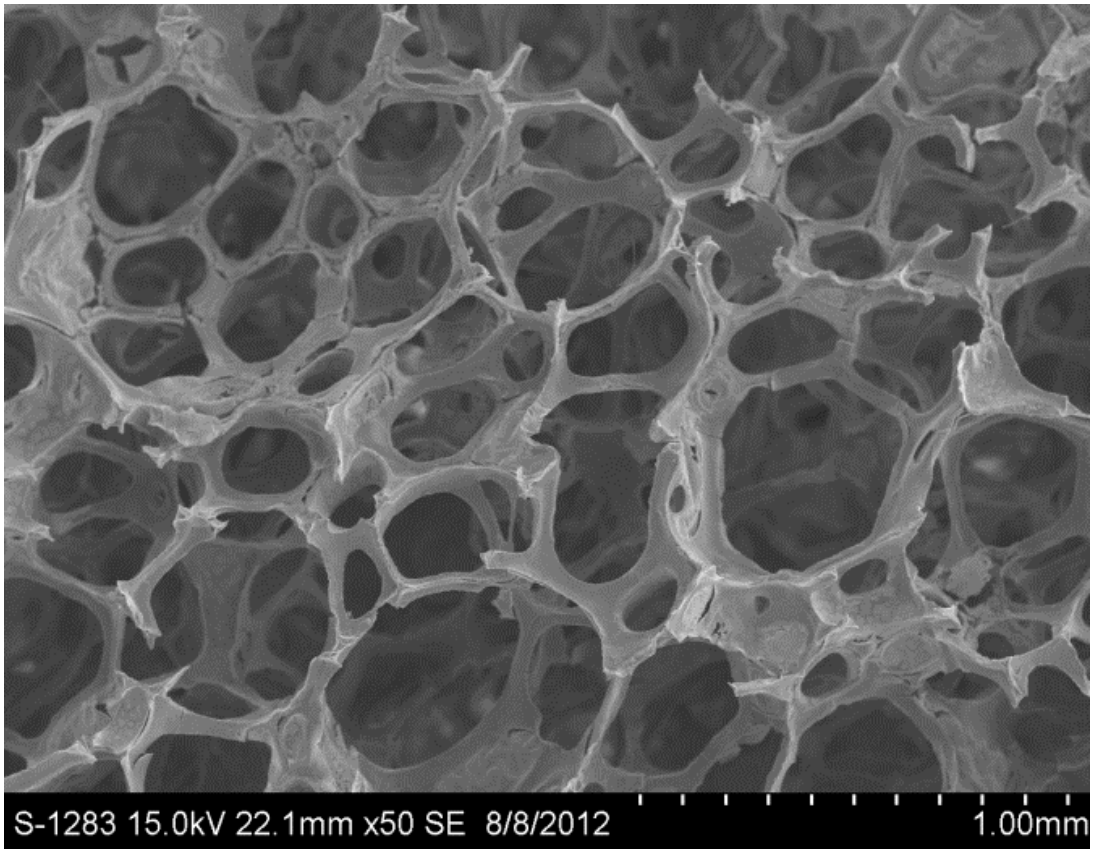

Figure 10. VTMS sample 10 (VS10) with corresponding SEM image.

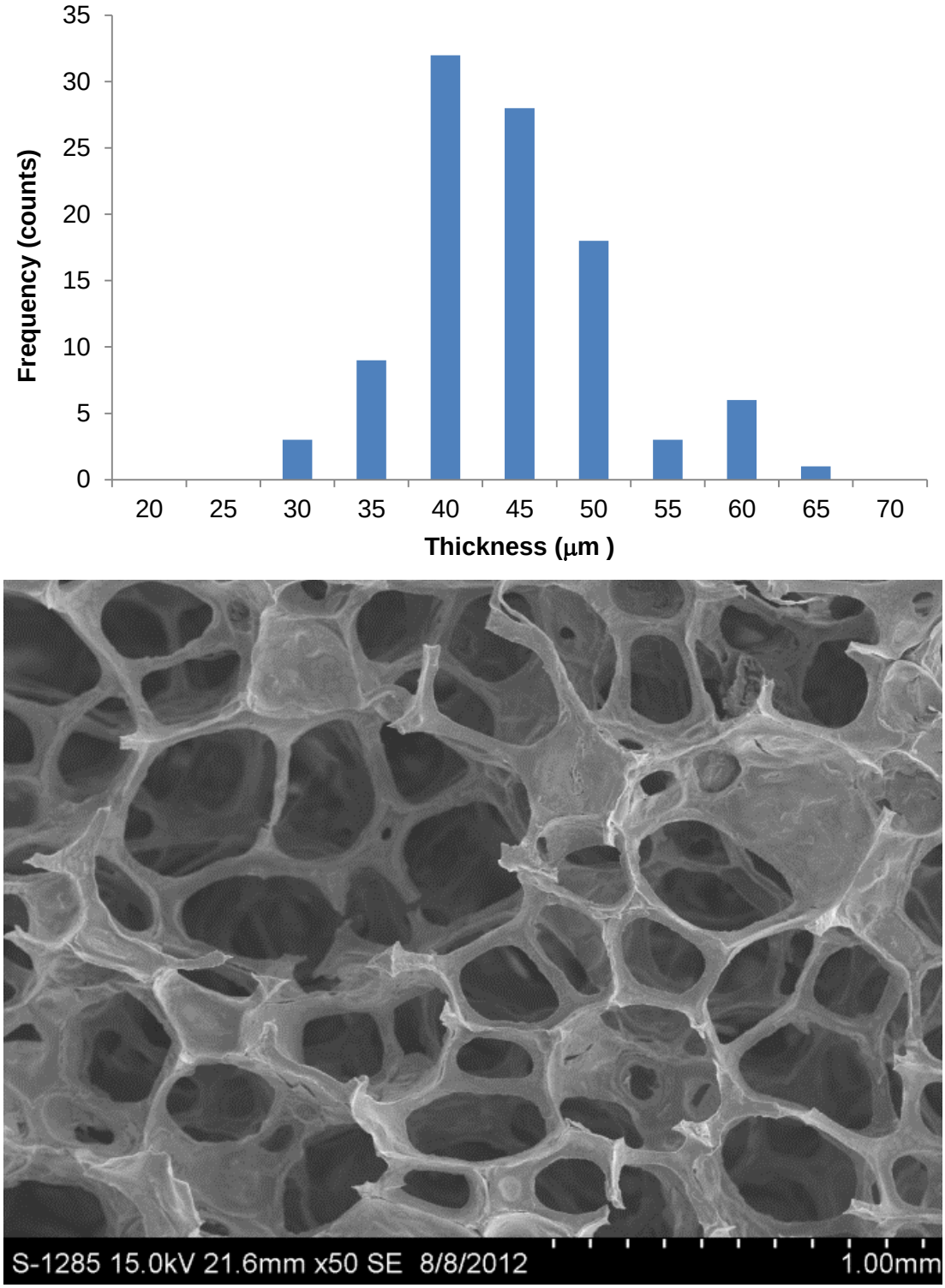

Figure 11. Control sample 12 (CS12) with corresponding SEM image.

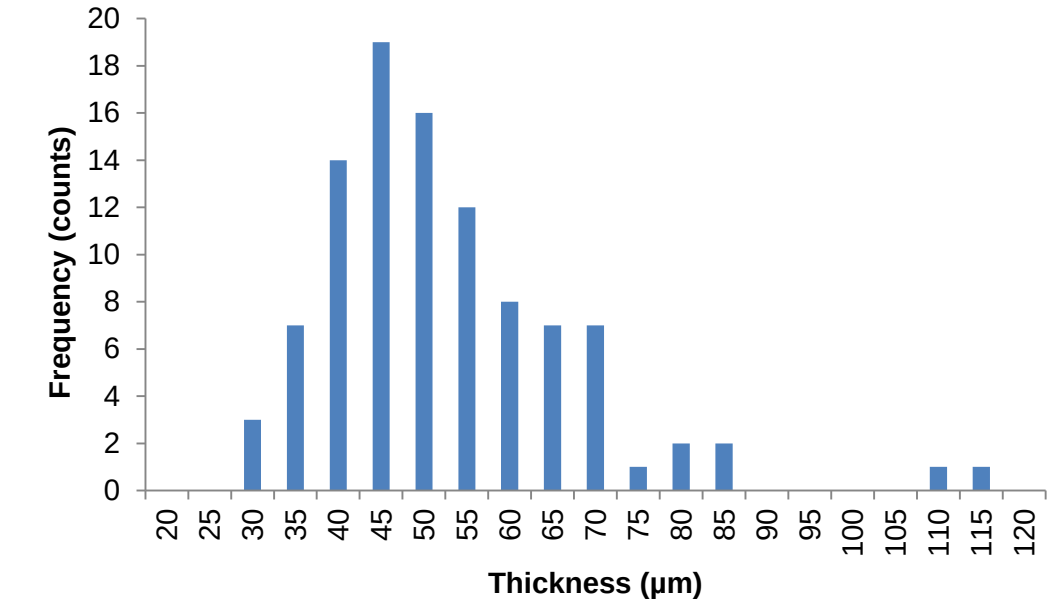

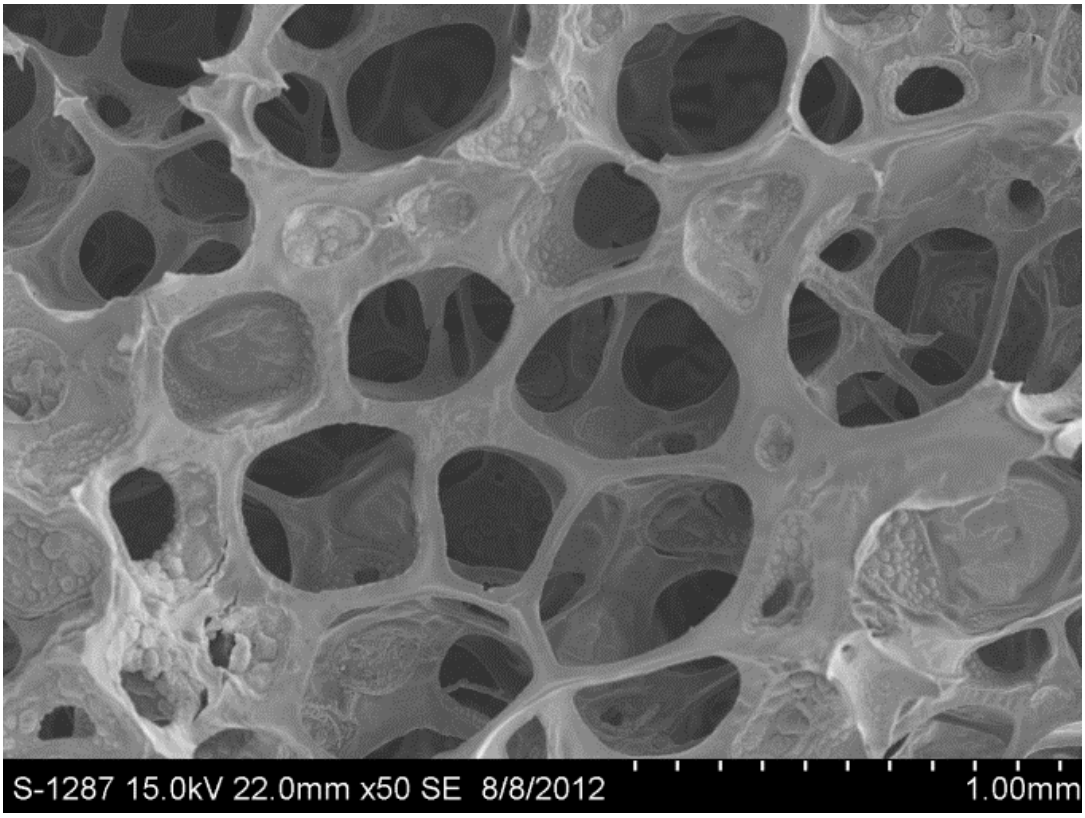

Figure 12. VTMS sample 12 (VS12) with corresponding SEM image.

Table 1. Average Pore Thickness for Control and VTMS Treated Samples

Sample	Standard Deviation	Mean thickness (μm)	Number of Dips	Drying time (hour)
Control-6	7.05	40.1	6	2
VTMS-6	*	*	6	2
Control-8	14.4	50.3	8	2
VTMS-8	7.92	37.1	8	2
Control-10	8.85	44.9	10	2
VTMS-10	8.29	43.2	10	2
Control 12-	7.19	42.3	12	2
VTMS-12	12.4	49.3	12	2

* Sample was too brittle for analysis.

CHAPTER IV

CONCLUSION

VTMS modified glasses were used in an attempt to strengthen mesoporous silicate structures that have been reported as scaffolds for bone replacement materials. The ratio of VTMS, the number or layers of silicate used, and drying times were varied. However, VTMS did not improve flexibility and no clear effect of VTMS/TEOS ratio was identified. If a mesoporous silicate coating on sponge could be produced that was strong enough for further derivatization, a VTMS coating applied as a post-thermal treatment could strengthen the scaffold. However, this may not be biocompatible.

LITERATURE CITED

1. Giannoudis, P. V.; Dinopoulos, H.; Tsiridis E. Bone Substitutes: An Update. *Injury* **2005,** *36*, 20-27.

2. Hench, L. L.; Polak, J. Third-Generation Biomedical Materials. *Science* **2002,** *295*, 1014-1017.

3. Eriksen, E. F.; Axelrod, D. W.; Melsen, F. *Bone Histomorphometry*, New York, Raven Press, 1994, pp 1-12.

4. Clarke, B. Normal Bone Anatomy and Physiology. *Clin. J. Am. Soc. Nephrol.* **2008,** *3*, 131-139.

5. Salinas, A. J.; Esbrit, P.; Vallet-Regi, M. A Tissue Engineering Approach on the Use of Bioceramics for Bone Repair. *Biomater. Sci.* **2013,** *1*, 40-51.

6. Castner, D. G.; Ratner, B. D. Biomedical Surface Science: Foundations to Frontiers. *Surf. Sci.* **2002,** *500*, 28-60.

7. Albrektsson, T.; Johansson, C. Osteoinduction, Osteoconduction, and Osseointegration. *Eur. Spine. J.*, **2001,** *10*, 96-101.

8. Hill, R. An Alternative View of the Degradation of Bioglass. *J. Mater. Sci. Lett.* **1996,** *15*, 344-351.

9. Hench, L. L.; Thompson, L. Twenty-First Century Challenges for Biomaterials. *J. R. Soc. Interface.* **2010,** *7*, 379-391.

10. Izquierdo-Barba, I.; Arcos, D.; Sakamoto, Y.; Terasaki, O.; López-Noriega, A.; Vallet-Regí, M. High-Performance Mesoporous Bioceramics Mimicking Bone Mineralizaton. *Chem. Mater.* **2008,** *20*, 3191-3198.

11. Garcia, A.; Cicuendez, M.; Izquierdo-Barba, I.; Arcos, D.; Vallet-Regí, M. Essential Role of Calcium Phosphate Heterogeneities in 2D-Hexagonal and 3D-Cubic SiO_2-CaO-P_2O_5 Mesoporous Bioactive Glasses. *Chem. Mater.* **2009,** *21*, 5474-5484.

12. Li, X.; Wang, X.; Chen, H.; Jiang, P.; Dong, X.; Shi, J. Hierarchically Porous Bioactive Glass Scaffolds Synthesized with a PUF and P123 Co-Templated Approach. *Chem. Mater.* **2007,** *19*, 4322-4326.

13. SEER Training Modules, *Anatomy and Physiology*. U.S. National Institute of Health, National Cancer Institute. 11 December 2010. http://training.seer.cancer.gov/anatomy/body/terminology.html.

14. Rasband, W.S., ImageJ, U. S. National Institutes of Health, Bethesda, Maryland, USA, http://imagej.nih.gov/ij/ , 1997-2014.

15. Vallet-Regi, M.; Ruiz-Hernandez, E. Bioceramics: From Bone Regeneration to Cancer Nanomedicine. *Ad. Mater.* **2011,** *23*, 5177-5218.

APPENDICES

Appendix A: UV Solvent Dependent Data

Table A.1: Solvent Dependent UV Data for Compounds **1 - 4**.

Solvent	**1** λ_{max} (nm)	**2** λ_{max} (nm)	**3** λ_{max} (nm)	**4** λ_{max} (nm)
Cyclohexane	-	-	-	-
Toluene	608	-	636	672
Ethanol	632	646	668	720
Dioxane	596	602	630	658
THF	608	614	638	676
C_3H_6O	604	614	636	672
CH_3CN	-	612	654	-
$CHCl_3$	-	670	680	724
CH_2Cl_2	640	656	678	724
CH_3NO_2	616	-	650	776
DMF	628	642	656	706
DMSO	632	642	674	740

Table A.2: Solvent Dependent UV Data for Compounds **5** - **8**.

Solvent	**5** λ_{max} (nm)	**6** λ_{max} (nm)	**7** λ_{max} (nm)	**8** λ_{max} (nm)
Cyclohexane	-	554	562	580
Ether	560	578	586	630
CCl_4	560	566	578	632
Toluene	568	586	597	640
CH_3CH_2OH	606	-	654	-
Ethyl acetate	572	-	-	648
dioxane	572	588	598	640
THF	580	602	614	656
C_3H_6O	586	614	626	674
CH_3CN	592	638	630	684
$CHCl_3$	604	640	654	682
CH_2Cl_2	600	610	650	-
CH_3NO_2	600	-	650	698
Pyridine	608	-	-	-
DMF	616	670	662	700
DMSO	636	686	682	716

Table A.2: Solvent Dependent UV Data for Compounds **9-11**.

Solvent	**9** λ_{max} (nm)	**10** λ_{max} (nm)	**11** λ_{max} (nm)
Cyclohexane	-	406	410
CCl_4	402	408	412
THF	408	410	419
C_3H_6O	410	412	420
CH_3CN	406	412	422
$CHCl_3$	416	420	434
CH_2Cl_2	414	422	430
DMF	414	422	428
DMSO	420	425	435

Appendix B: NMR Solvent Dependent Data

Compound **9 :** (2E,4E)-5-(4-(dimethylamino)phenyl)penta-2,4-dienal

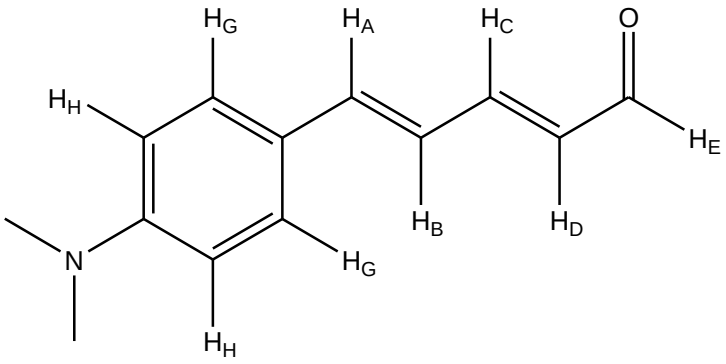

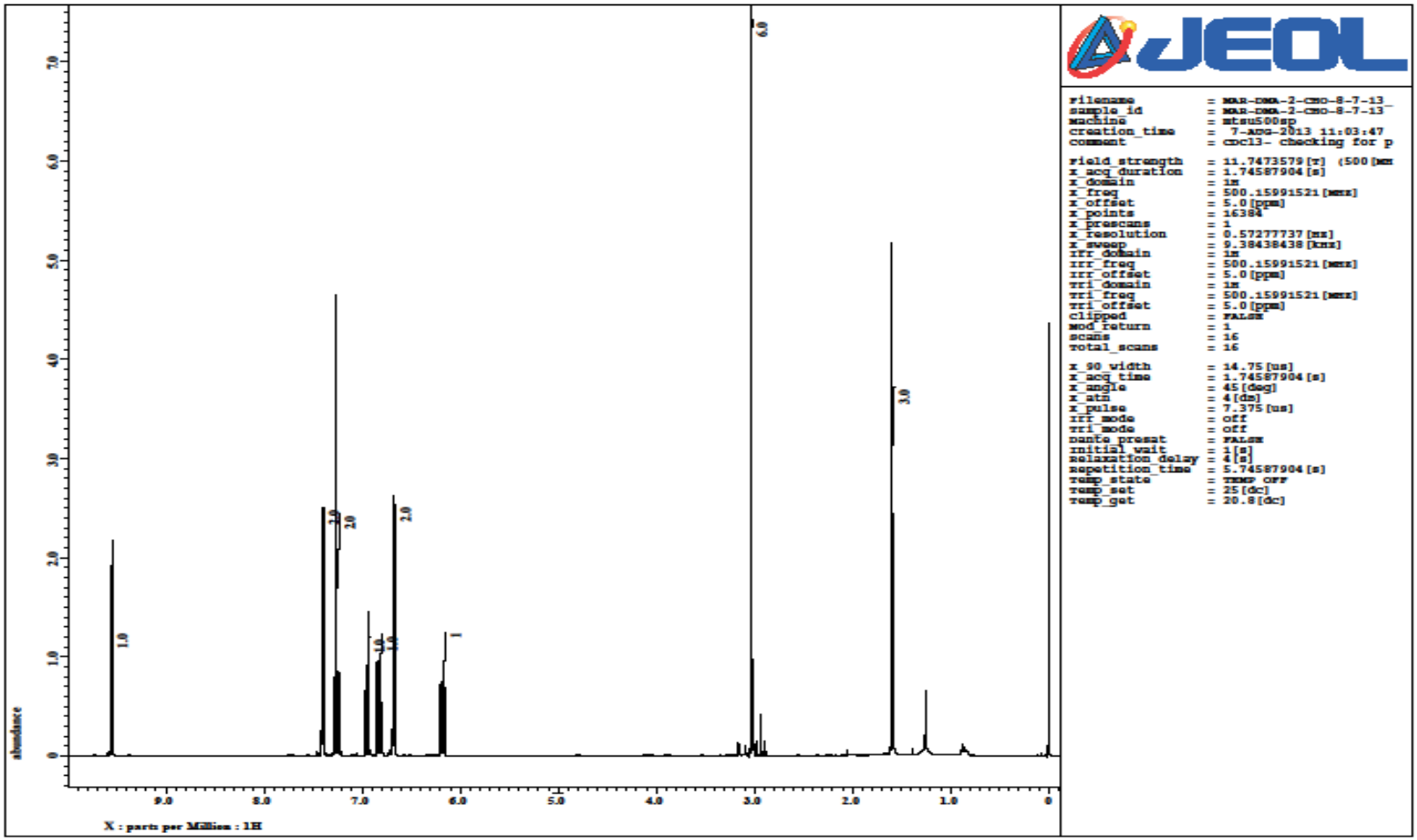

Figure B.1 ^{1}H NMR Spectrum for compound **9** in $CDCl_3$.

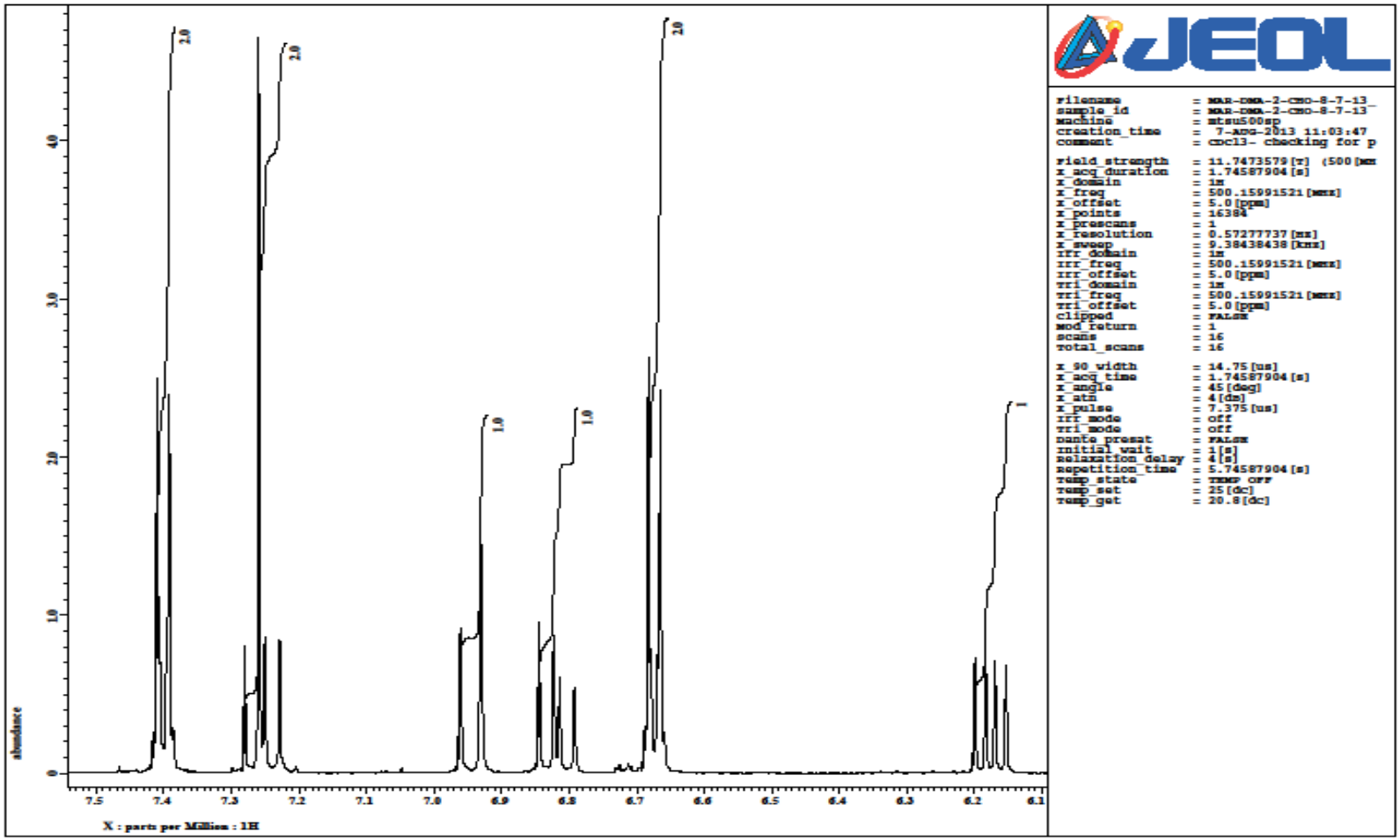

Figure B.2 ^{1}H NMR Spectrum zoomed in for compound **9** in $CDCl_3$.

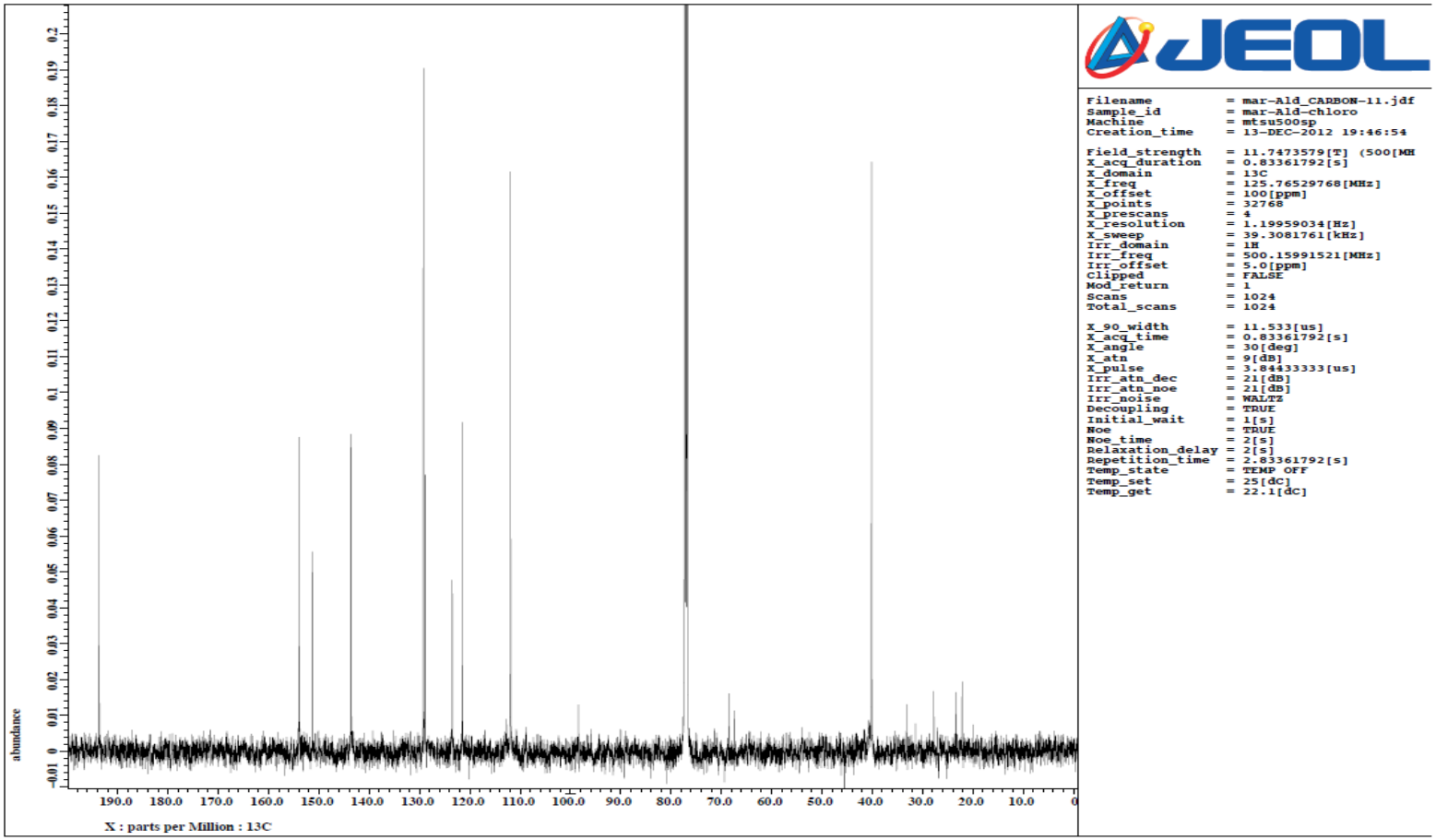

Figure B.3 ^{13}C NMR spectrum for compound **9** in $CDCl_3$.

Table B.1 ^{1}H NMR Coupling Constants for compound **9**.

Solvent	AB	BA	BC	CB	CD	DC	DE	ED	ΔJ
CDCl3	15.4	14.9	10.9	10.9	14.9	14.9	8.0	8.1	5.53
DMSO	15.4	15.4	10.9	9.7	15.5	14.9	8.0	8.1	6.1
C_3D_6O	15.5	15.5	10.9	10.6	15.2	14.9	8.1	8.0	5.63
C_2D_3CN	15.5	15.5	10.9	10.8	14.9	15.2	8.3	8.0	o

Table B.2 ^{1}H NMR Chemical shifts for compound **9**.

Solvent	A	B	C	D	E
CDCl3	6.95	6.82	7.26	6.18	9.56
DMSO	7.04	6.95	7.41	6.11	9.47
C_3D_6O	7.04	6.95	7.37	6.11	9.53
C_2D_3CN	6.99	6.88	7.32	6.09	9.50

Compound **5:** 5-((2E,4E)-5-(4-(dimethylamino)phenyl)penta-2,4-dienylidene)-1,3-diethyl-2-thioxo-dihydropyrimidine-4,6(1H,5H)-dione

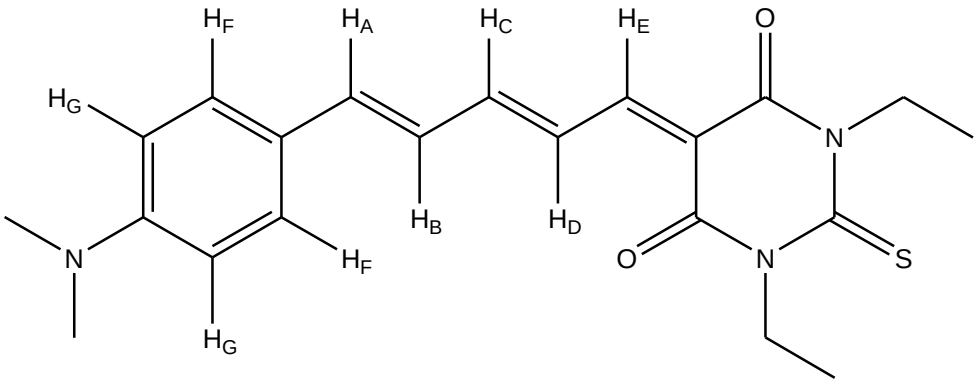

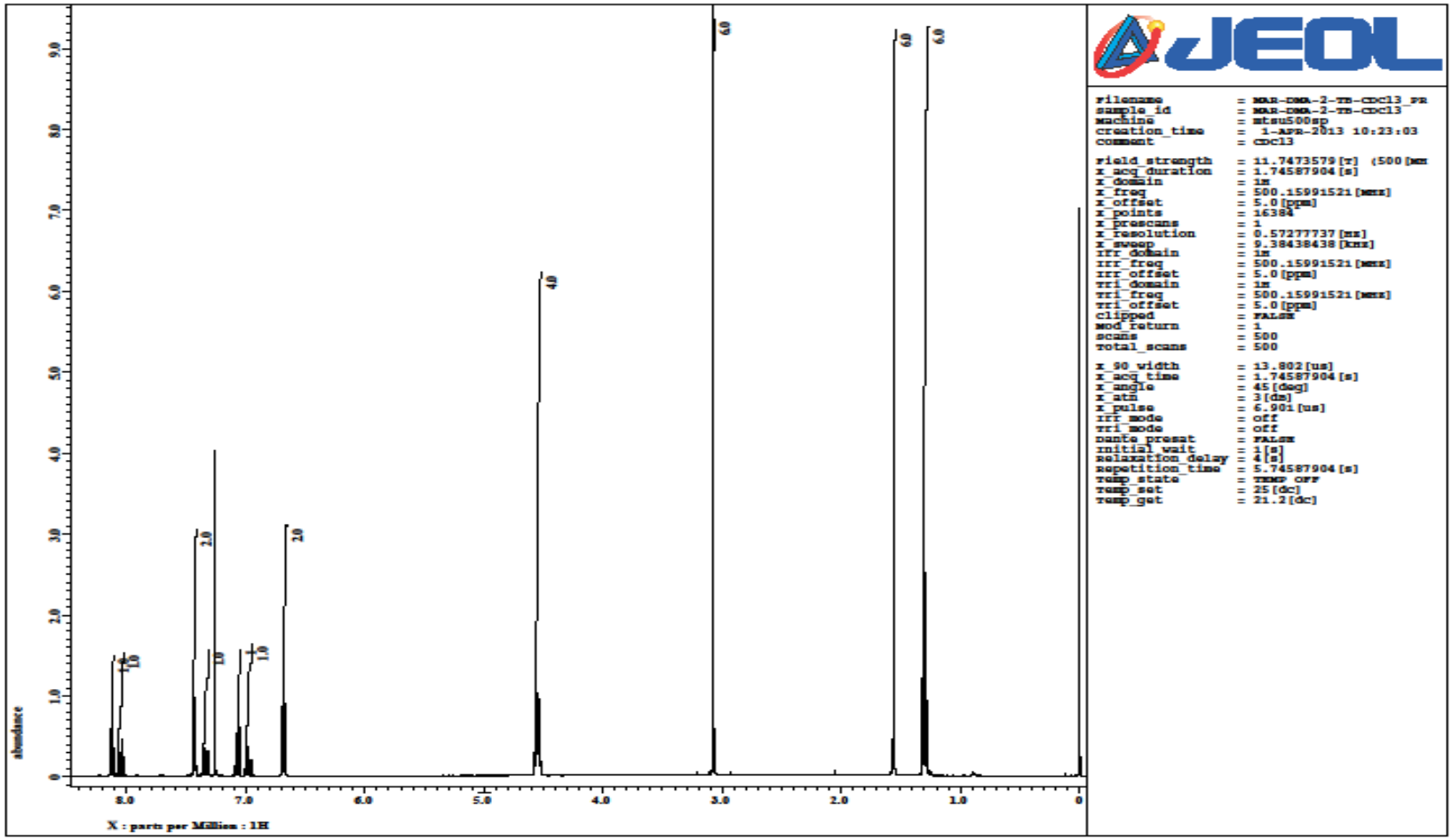

Figure B.4 ^{1}H NMR spectrum for compound **5** in $CDCl_3$.

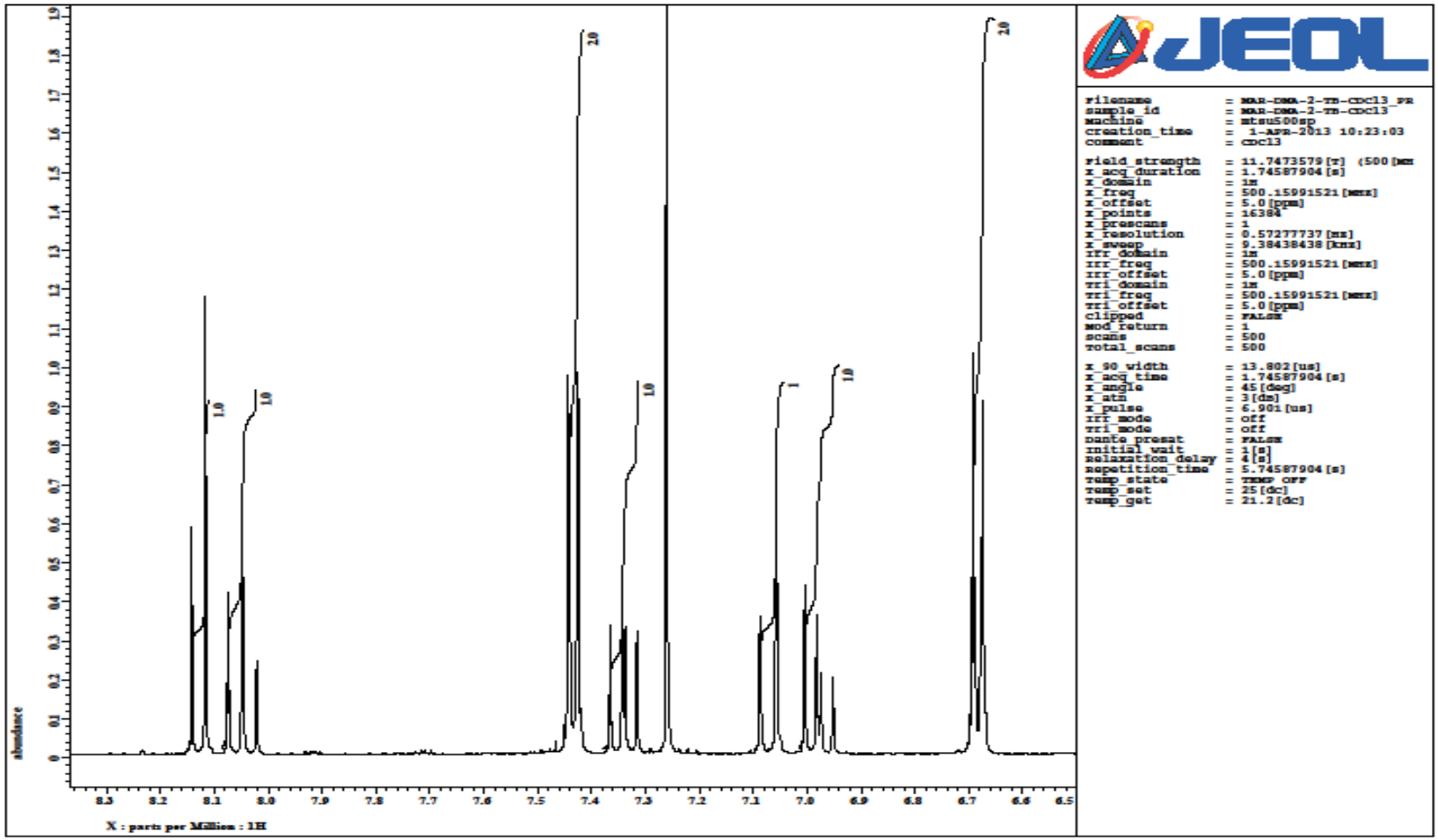

Figure B.5 ^{1}H NMR spectrum zoomed in for compound **5** in $CDCl_3$.

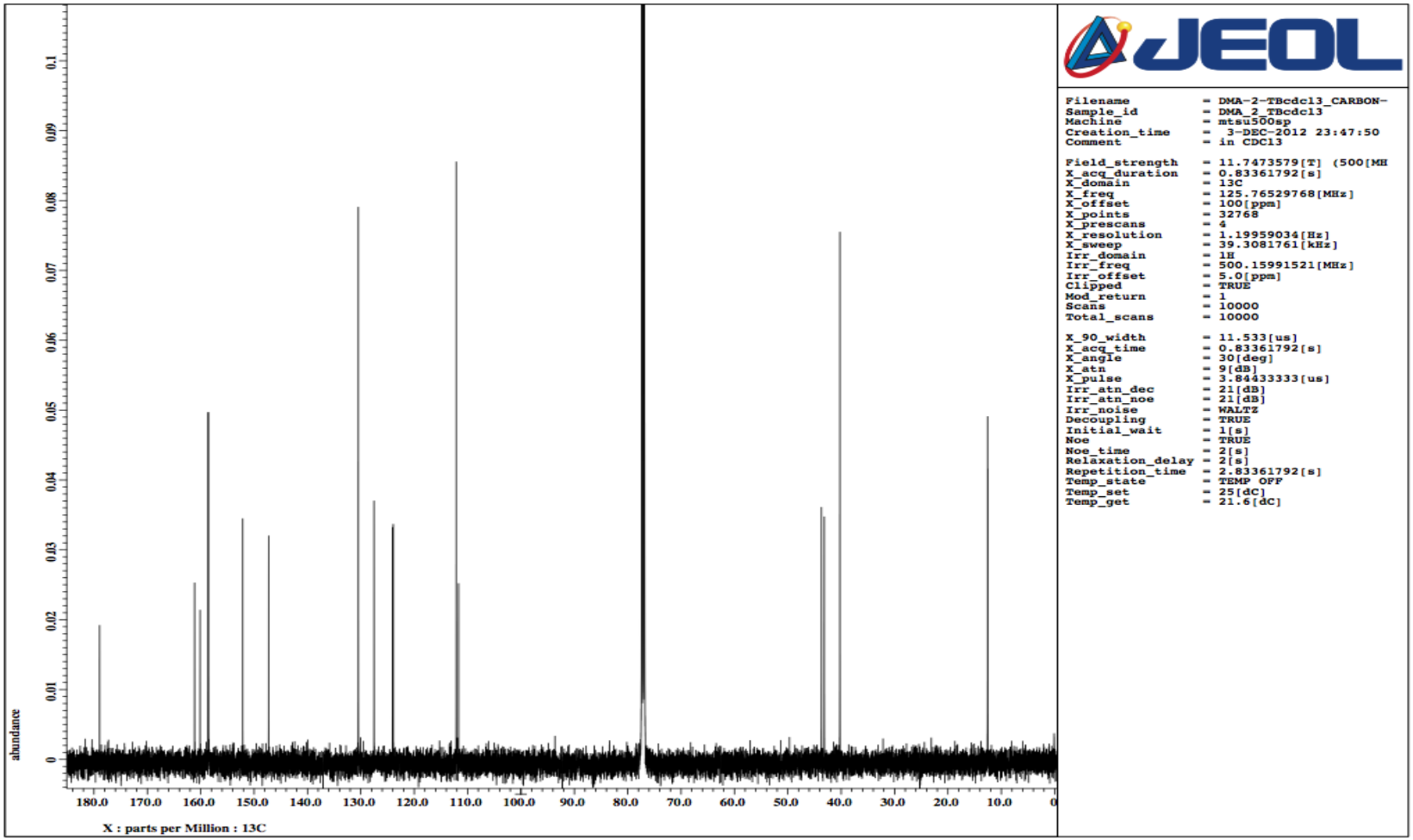

Figure B.6 ^{13}C NMR for compound **5** in $CDCl_3$.

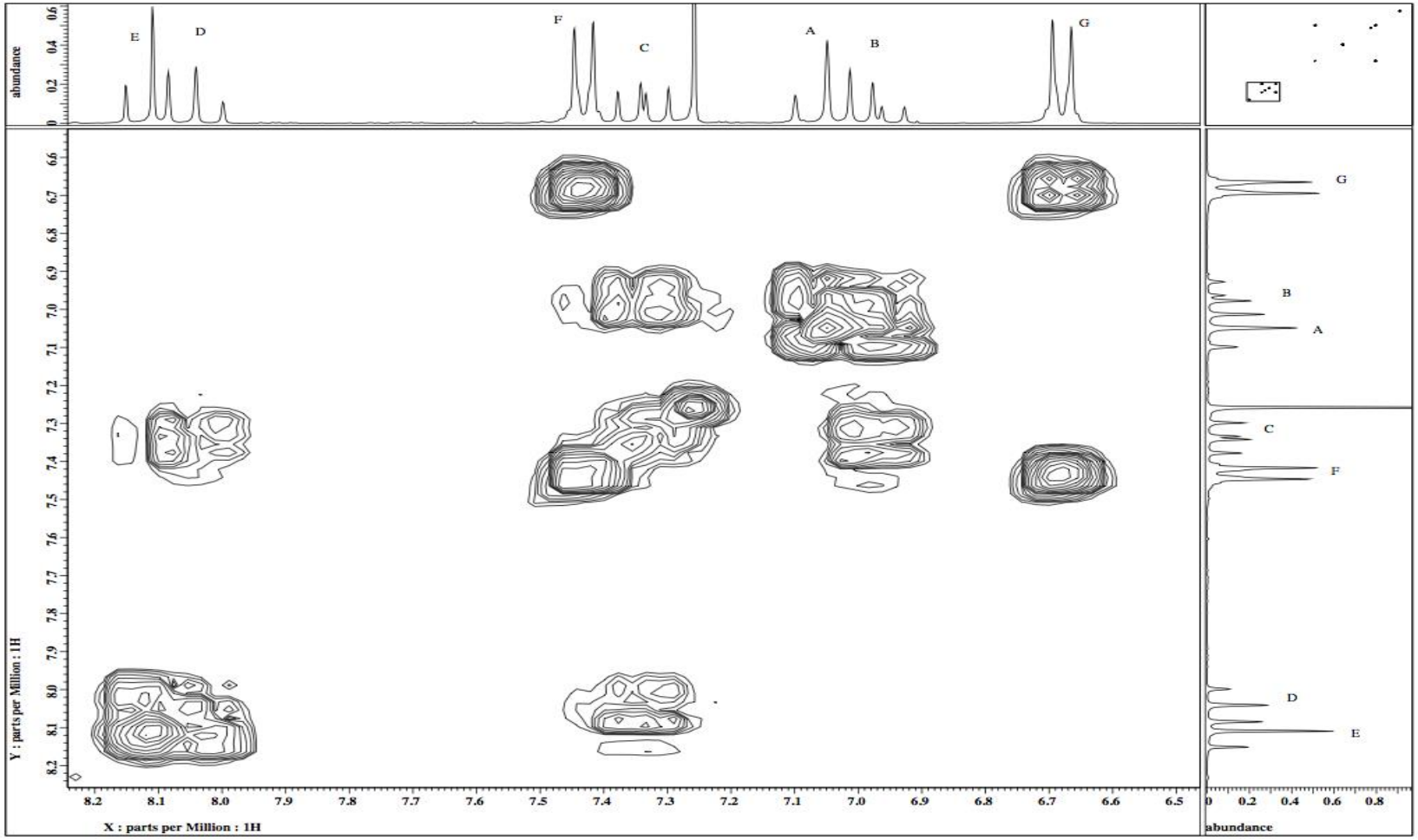

Figure B.7 ^{1}H-^{1}H COSY spectrum for compound **5** in $CDCl_3$.

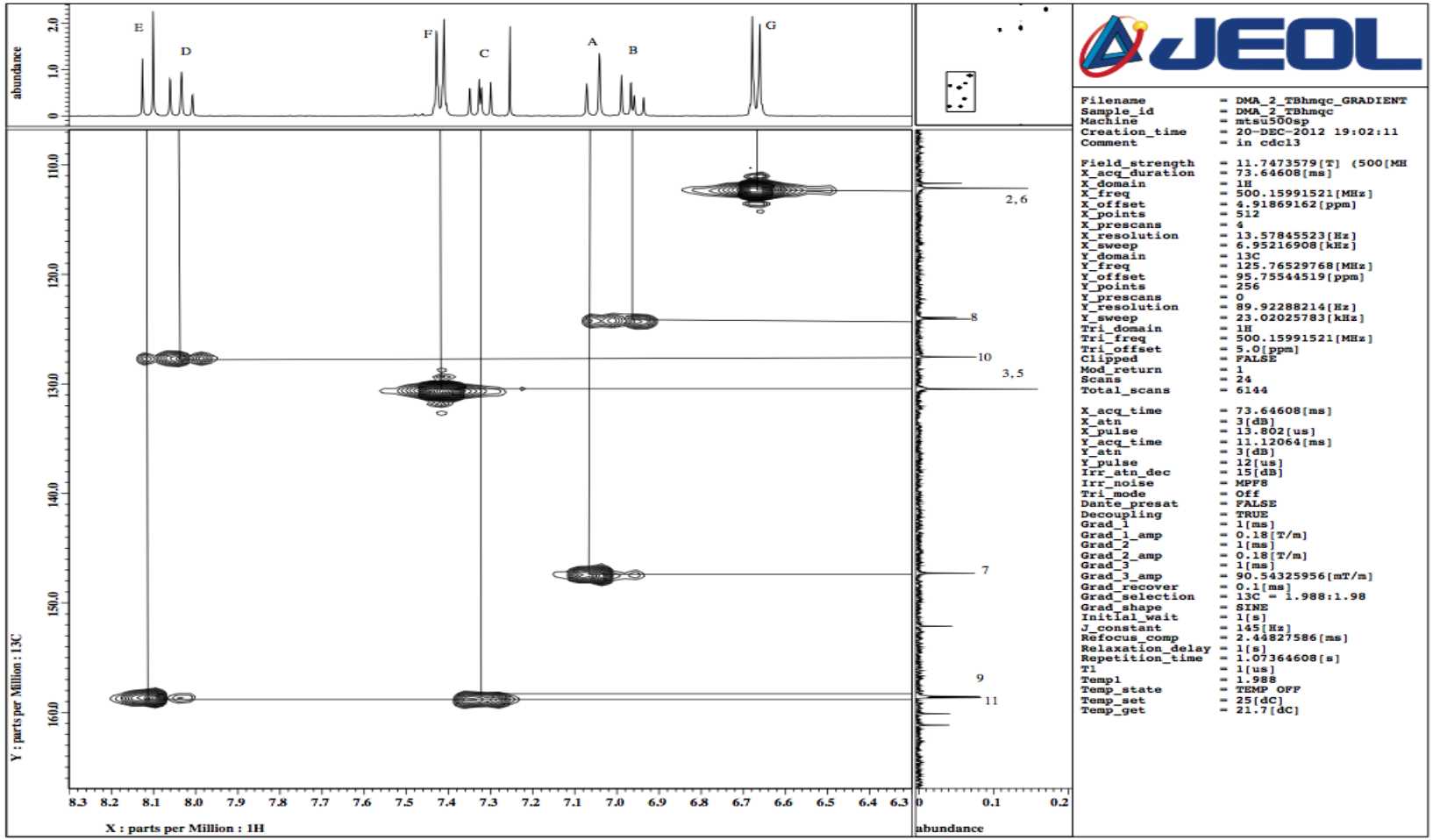

Figure B.8 HMQC of compound **5** in $CDCl_3$.

Table B.3 ^{1}H NMR Coupling Constants for compound **5**.

Solvent	AB	BA	BC	CB	CD	DC	DE	ED	ΔJ
CDCl3	14.9	14.9	11.4	11.2	14.1	13.7	12.6	12.6	2.45
DMSO	14.8	14.9	10.9	10.3	13.8	13.8	12.6	12.6	2.3
C_3D_6O	14.8	14.9	10.9	7.4	16.6	13.6	12.6	12.6	2.73
C_6D_6	14.9	14.3	10.3	10.3	14.3	13.8	12.6	12.7	

Table B.4 ^{1}H NMR Chemical Shifts for compound **5**.

Solvent	A	B	C	D	E	F	G
$CDCl_3$	7.07	6.98	7.34	8.05	8.13	6.68	7.43
DMSO	7.31	7.25	7.71	7.99	8.09	6.80	7.62
C_3D_6O	7.30	7.23	7.63	8.07	8.13	6.83	7.64
C_6D_6	6.61	6.71	6.74	8.38	8.23	6.34	-

Compound **6**: (2*E*, 4*E*)-(5-(4-N-Methyl indolinyl)-penta-2,4,6-trienyl)-thiobarbituric acid

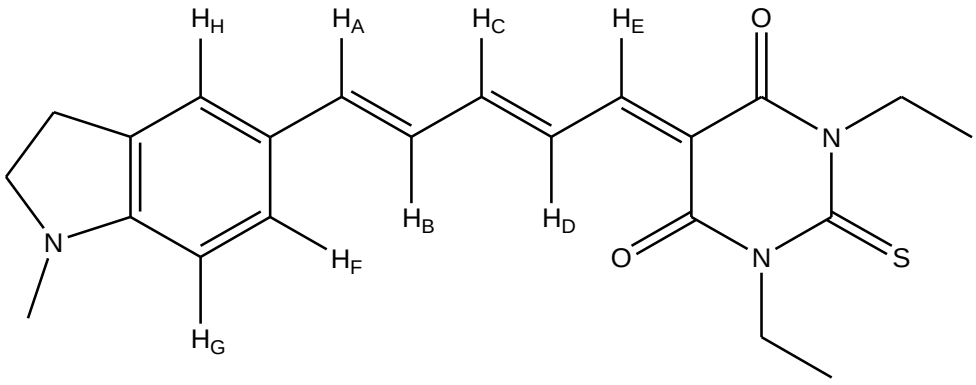

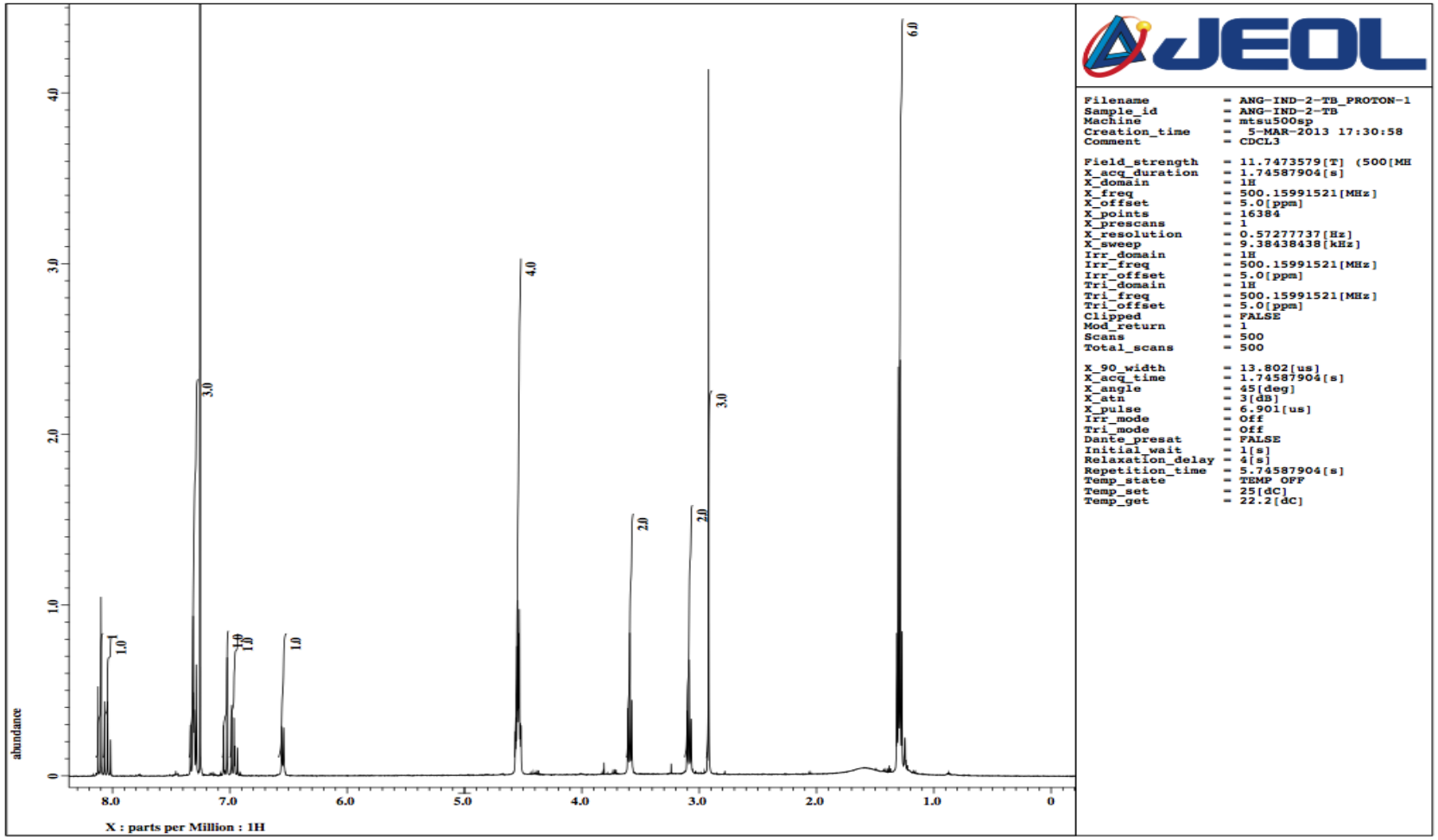

Figure B.9 ^{1}H NMR spectrum of compound **6** in $CDCl_3$.

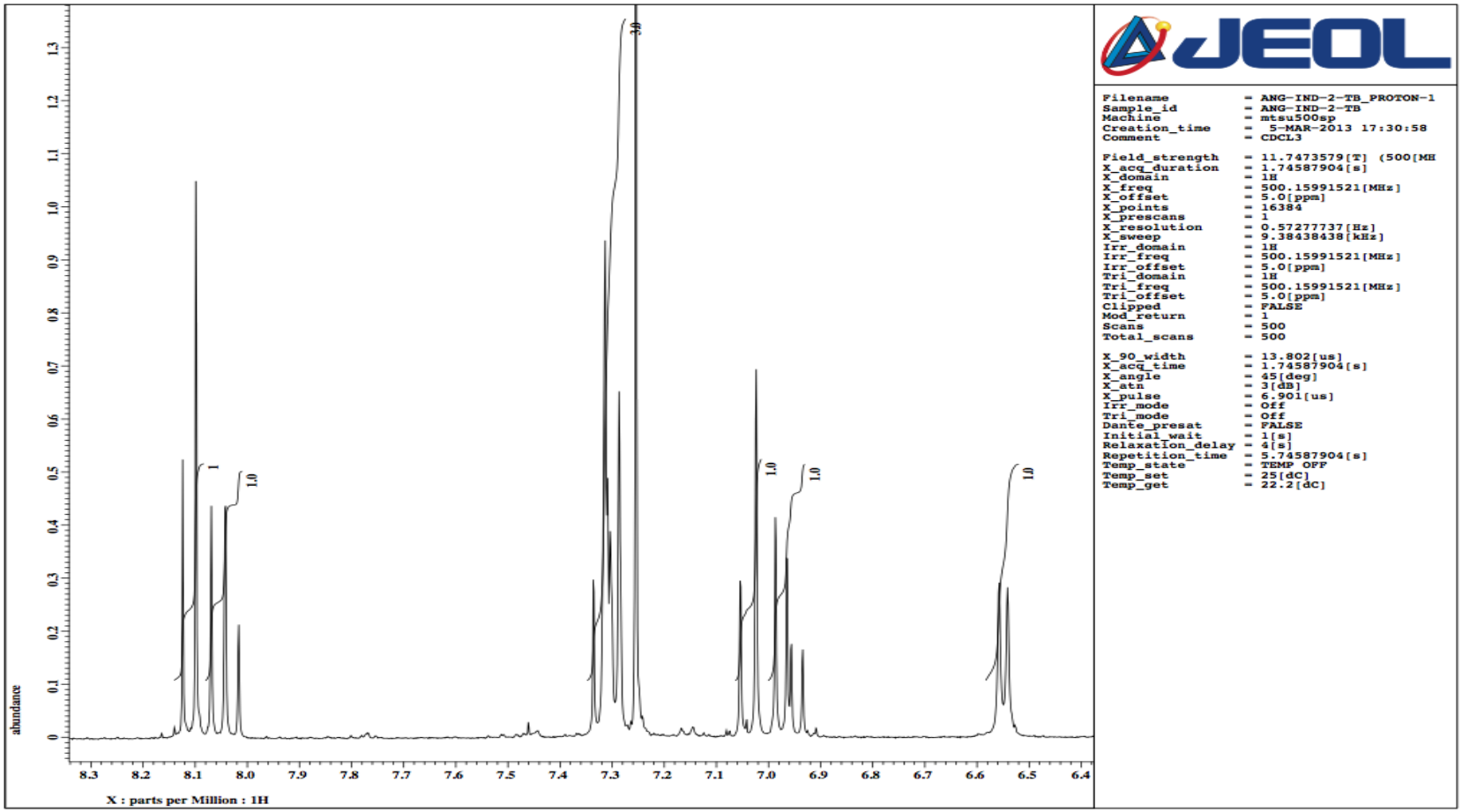

Figure B.10 ^{1}H NMR spectrum zoomed in for compound **6** in $CDCl_3$.

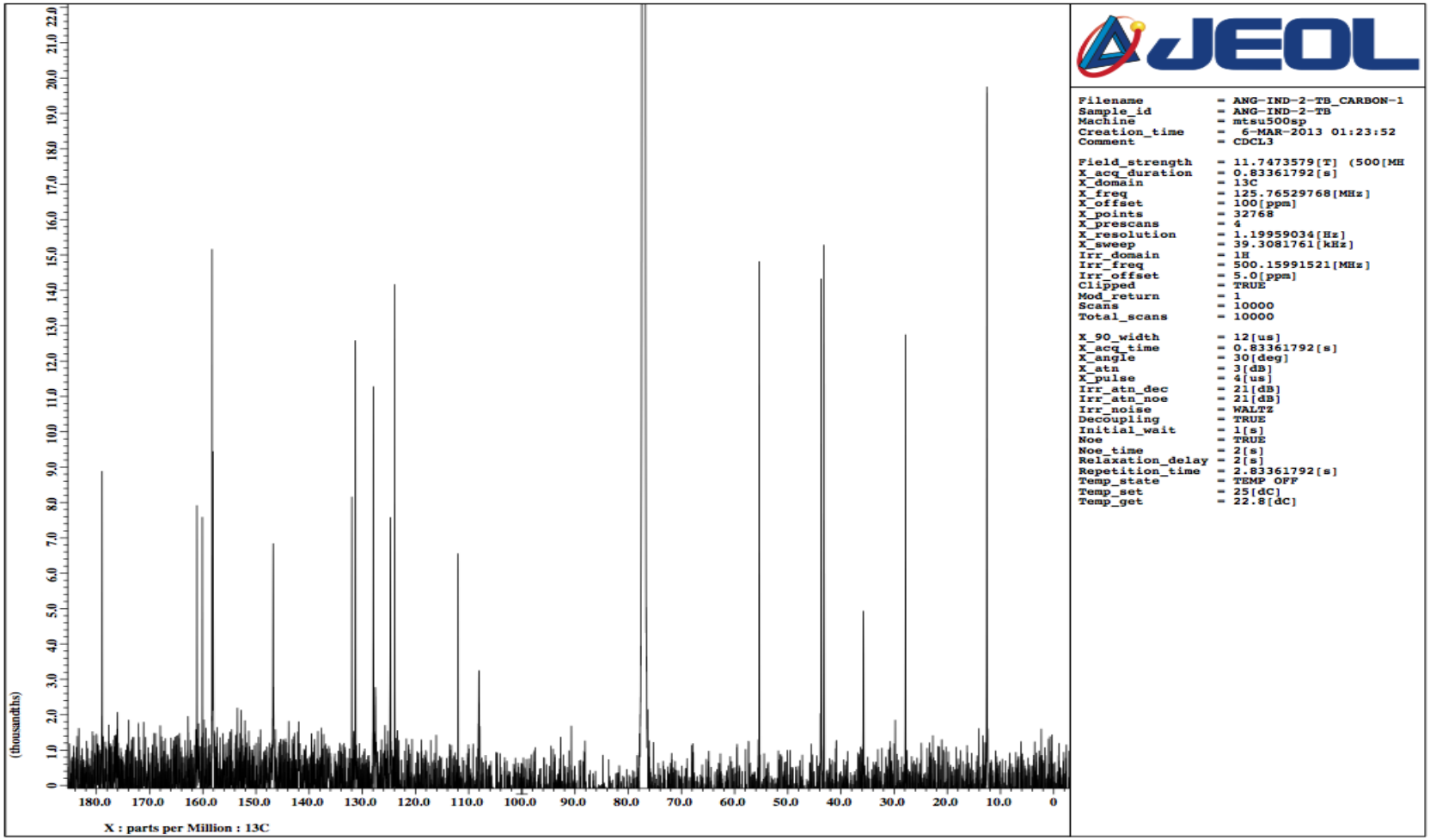

Figure B.11 ^{13}C NMR spectrum of compound **6** in $CDCl_3$.

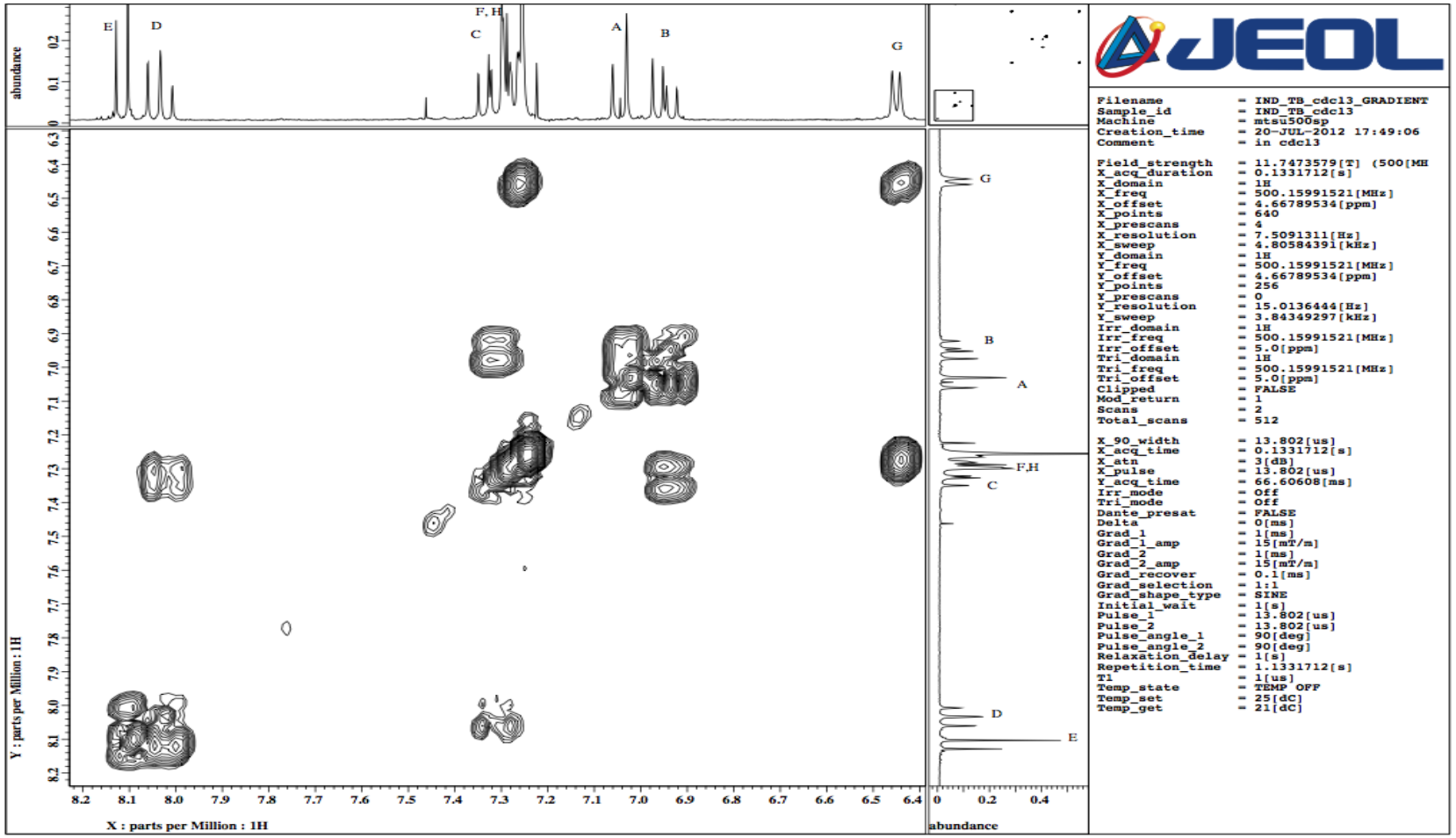

Figure B.12 ^{1}H-^{1}H COSY spectrum for compound **6** in $CDCl_3$.

Table B.5 ^{1}H NMR Coupling Constants for compound **6**.

Solvent	**AB**	**BA**	**BC**	**CB**	**CD**	**DC**	**DE**	**ED**	**FG**	**GF**	**∆J**
CDCl3	14.9	14.9	11.5	11.5	13.7	13.2	13.2	12.6	o	o	1.98
DMSO	14.9	14.9	11.5	11.5	13.8	13.2	13.1	12.6	8.6	8.0	2.03
C_3D_6O	14.9	14.9	10.9	10.9	13.2	13.2	12.6	12.6	8.1	8.0	2.30
CD_3CN	14.9	14.1	10.55	10.3	o	13.8	13.8	12.6	8.6	8.0	2.19

Table B.6 ^{1}H NMR Chemical Shifts for compound **6**.

Solvent	**A**	**B**	**C**	**D**	**E**	**F**	**G**	**H**
$CDCl_3$	7.05	6.94	7.33	8.02	8.13	o	6.37	o
DMSO	7.26	7.17	7.66	7.91	8.03	7.41	6.53	7.48
C_3D_6O	7.25	7.16	7.58	8.02	8.07	7.40	6.51	7.58
CD_3CN	7.12	7.06	7.46	7.95	8.04	7.30	6.41	7.36

Compound **7**: (2*E*, 4*E*)-5-(1-Methyl-1,2,3,4-tetrahydroquinolin-6-yl)penta-2,4-dienyl thiobarbituric acid

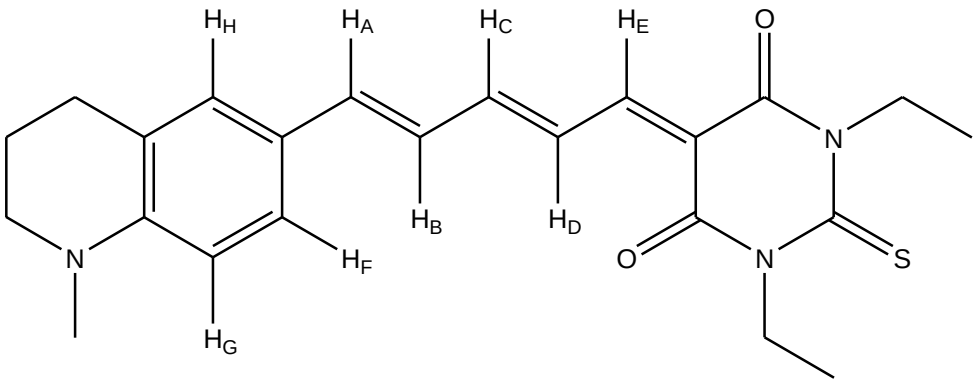

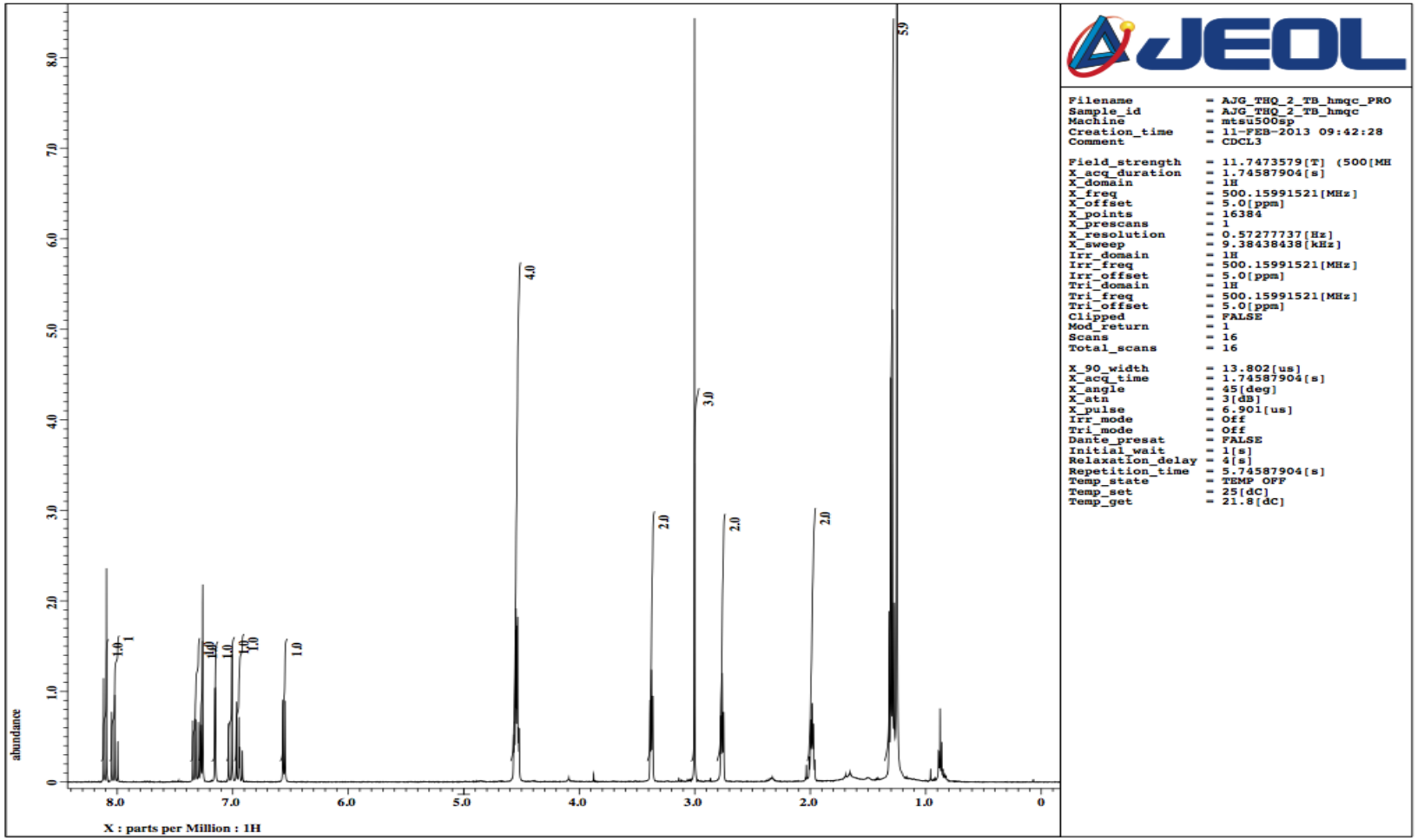

Figure B.13 ^{1}H spectrum of compound **7** in $CDCl_3$.

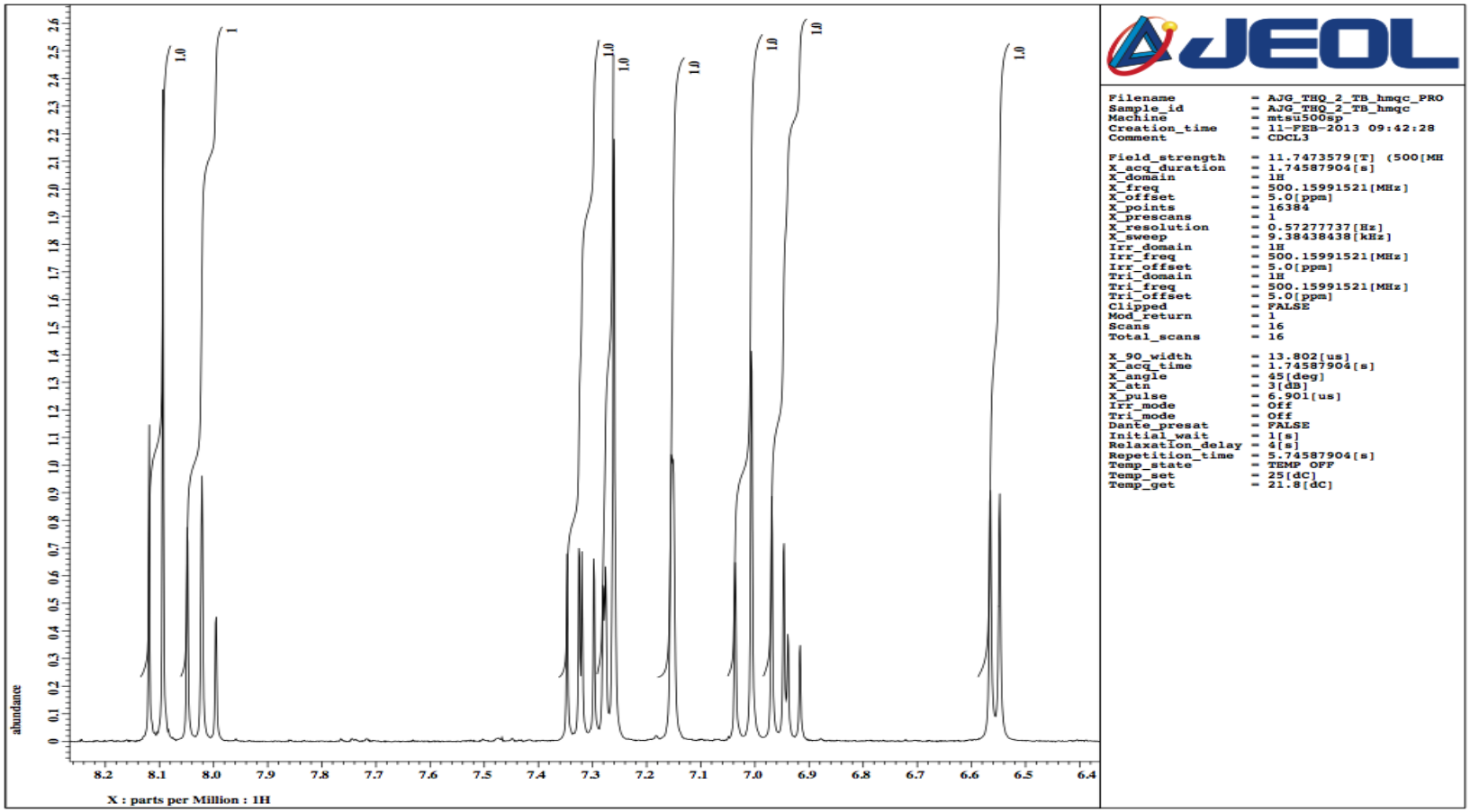

Figure B.14 ^{1}H NMR spectrum zoomed in for compound **7** in $CDCl_3$.

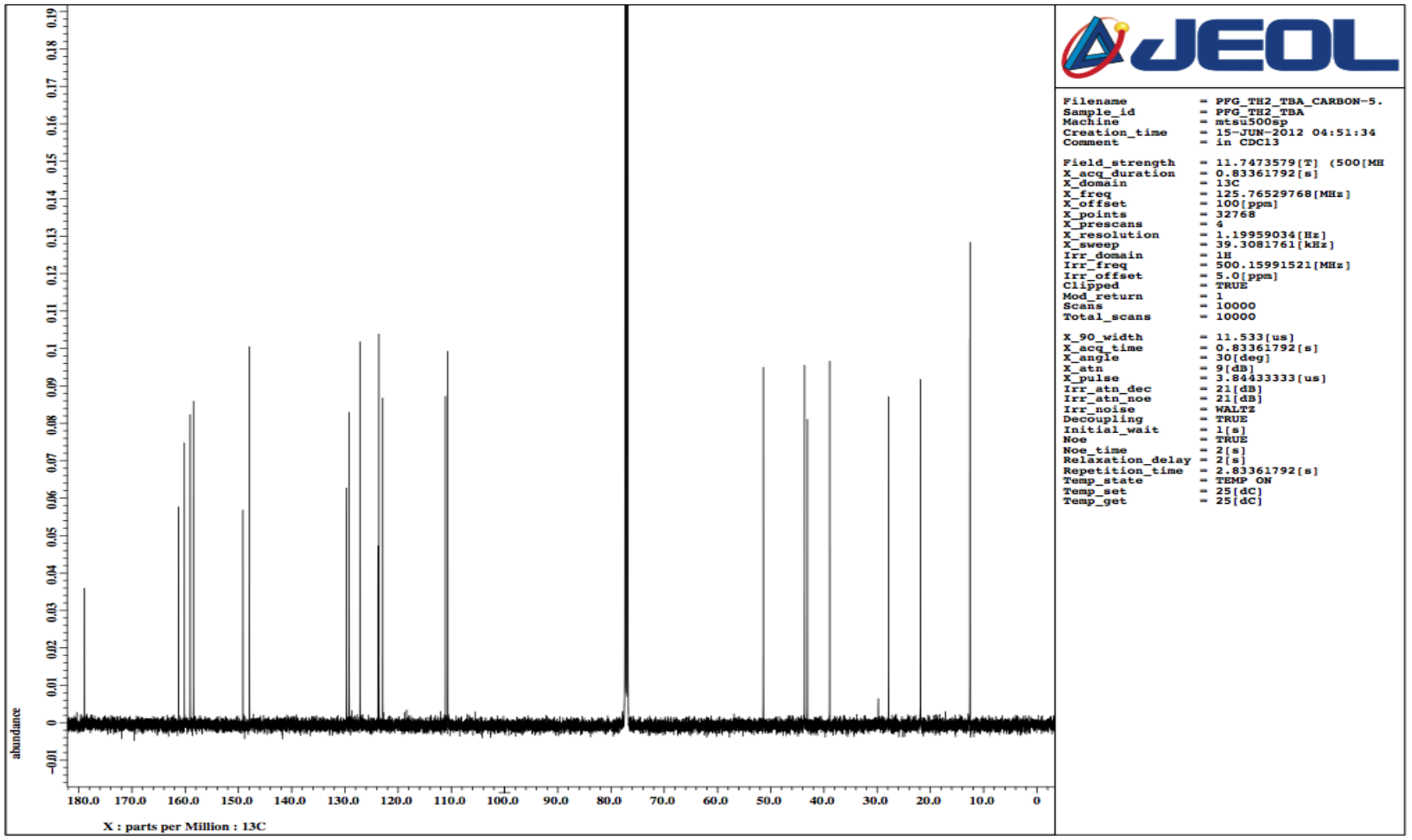

Figure B.15 ^{13}C NMR spectrum for compound **7** in $CDCl_3$.

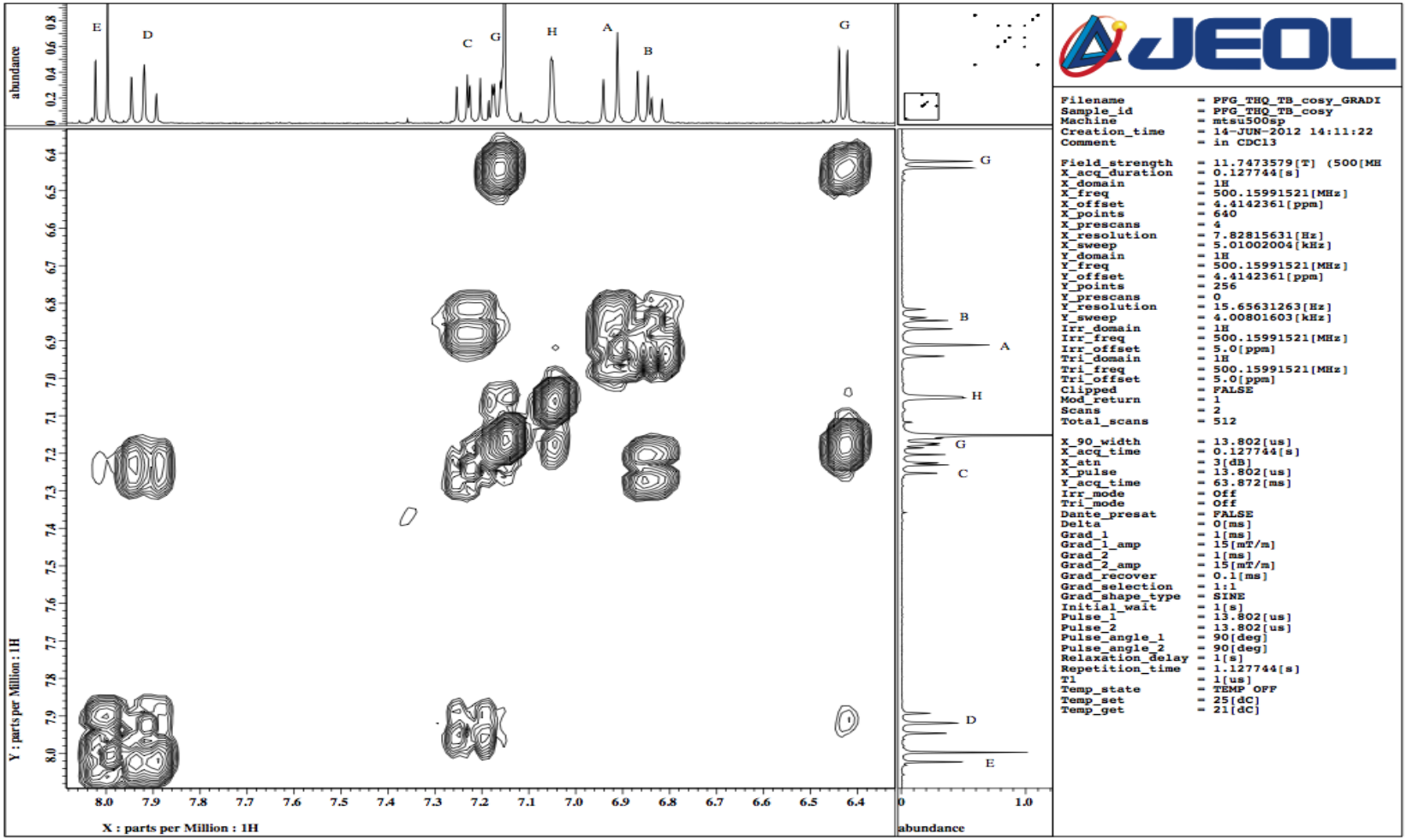

Figure B.16 ^{1}H-^{1}H COSY for compound **7** in $CDCl_3$.

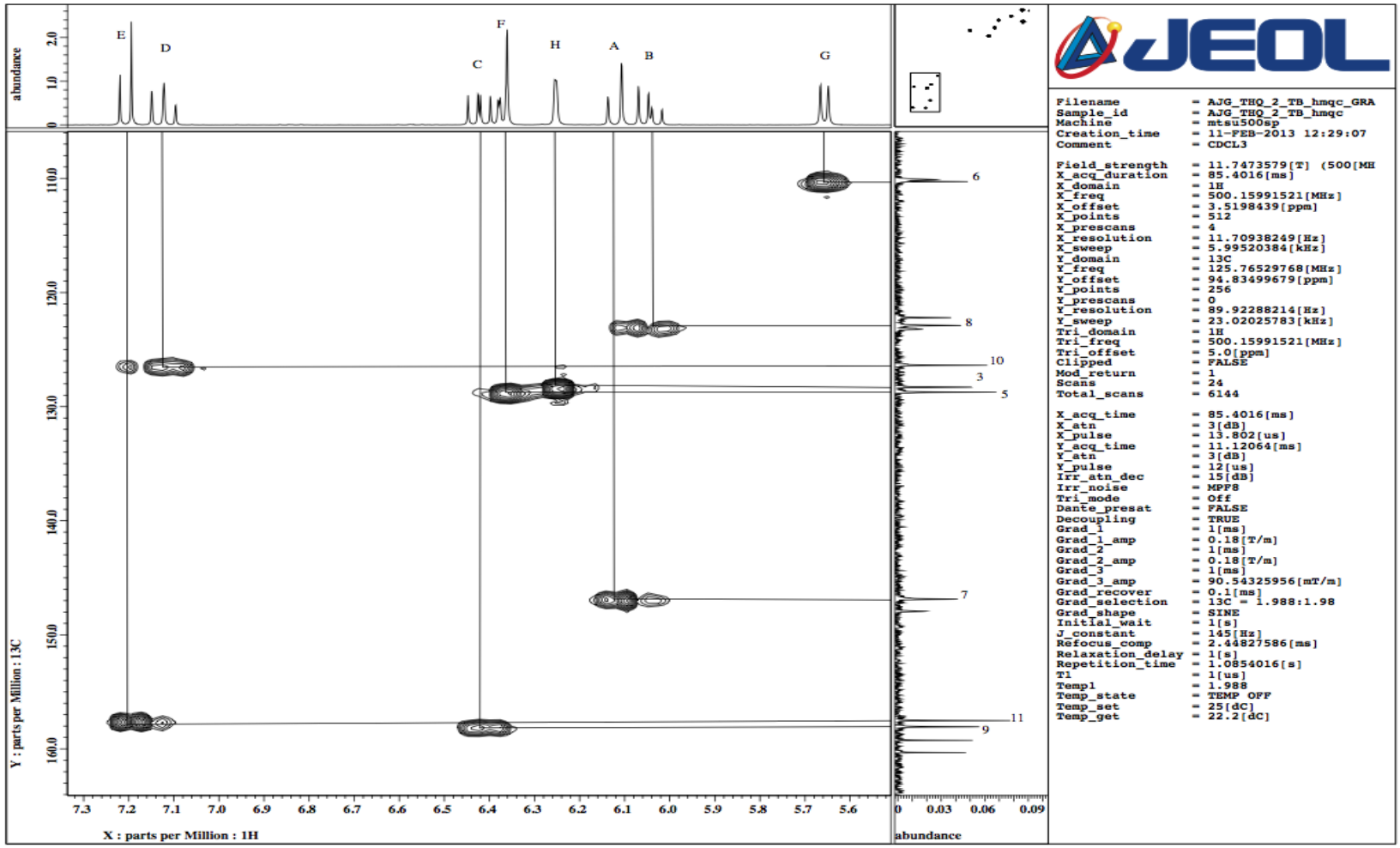

Figure B.17 HMQC for compound **7** in $CDCl_3$.

Table B.7 ^{1}H NMR Coupling Constants for compound **5**.

Solvent	AB	BA	BC	CB	CD	DC	DE	ED	FG	GF	ΔJ
CDCl3	14.9	14.9	11.5	10.9	13.7	13.2	13.2	12.6	o	o	2.13
DMSO	14.9	14.9	10.6	10.9	13.8	13.2	13.2	13.1	o	o	2.25
C_3D_6O	14.9	14.9	10.3	10.9	13.2	12.9	12.9	12.4	o	o	2.35
CD_3CN	o	o	o	10.9	13.7	13.7	12.7	13.1	9.2	8.0	-

Table B.8 ^{1}H NMR Chemical Shifts for compound **5**.

Solvent	A	B	C	D	E	F	G	H
$CDCl_3$	7.03	6.94	7.33	8.02	8.11	7.27	6.37	7.29
DMSO	7.22	7.16	7.58	8.02	8.08	7.42	6.64	7.34
C_3D_6O	7.22	7.16	7.58	8.02	8.08	6.64	7.42	7.34
CD_3CN	o	o	7.50	7.98	8.07	7.11	6.60	7.26

Compound **8**: 5-(4-julolidinyl)-2,4-pentadienyl-*N*,*N*-diethylthiobarbituric acid

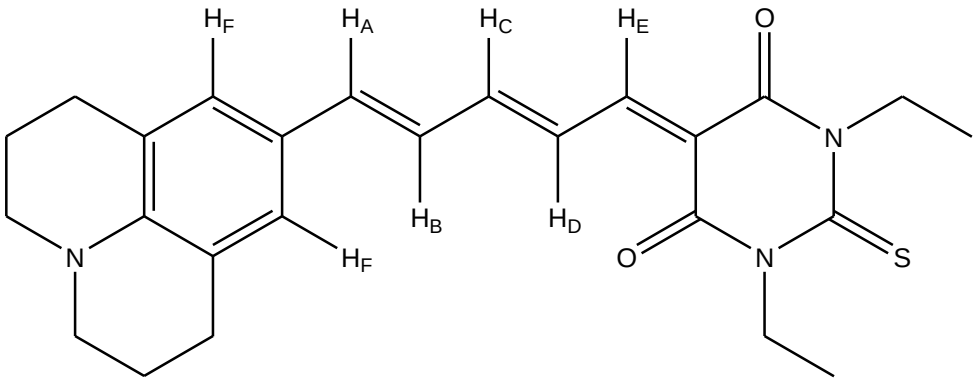

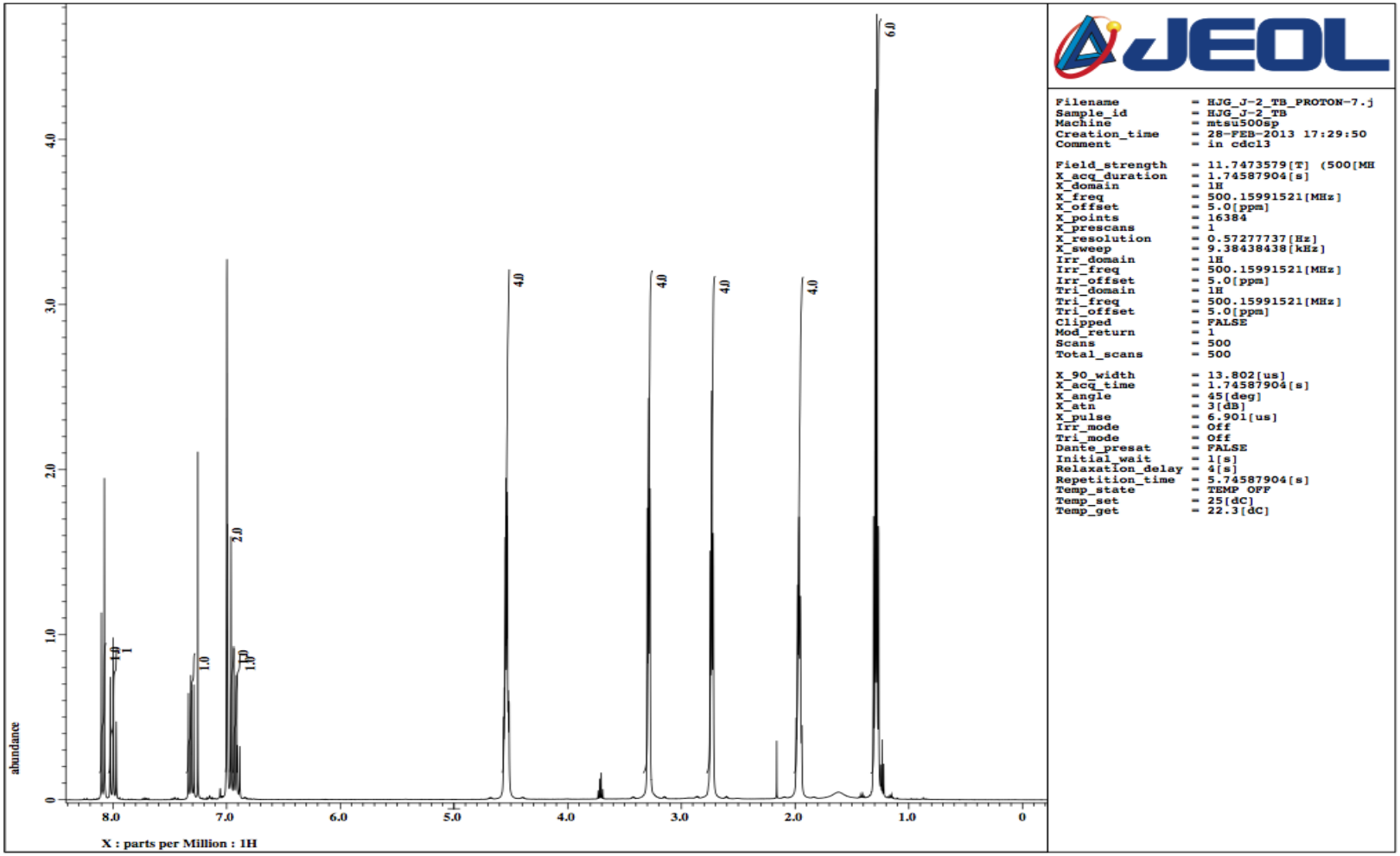

Figure B.18 ^{1}H NMR spectrum for compound **8** in $CDCl_3$.

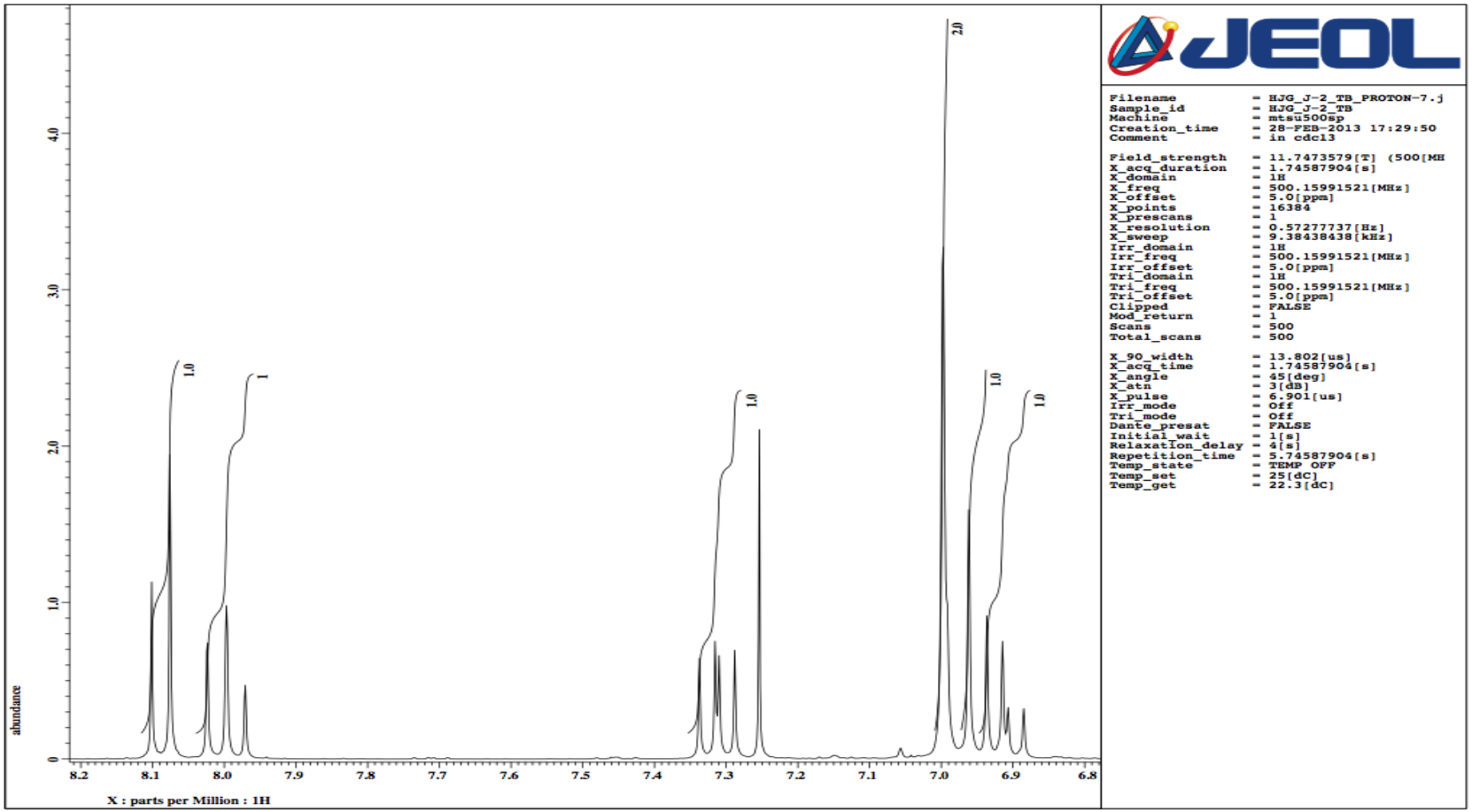

Figure B.19 ^{1}H NMR spectrum zoomed in for compound **8** in $CDCl_3$.

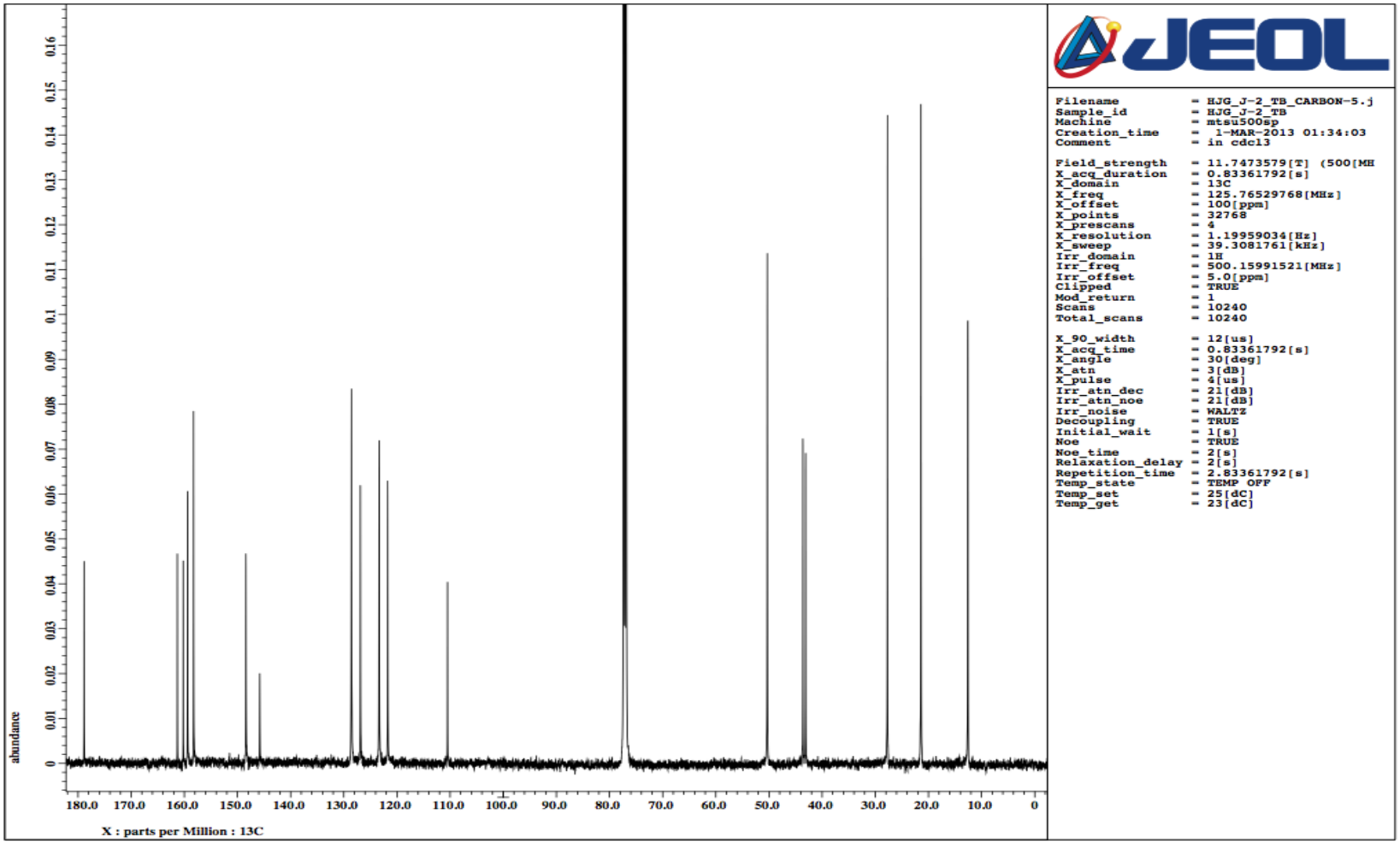

Figure B.20 ^{13}C NMR spectrum for compound **8** in $CDCl_3$.

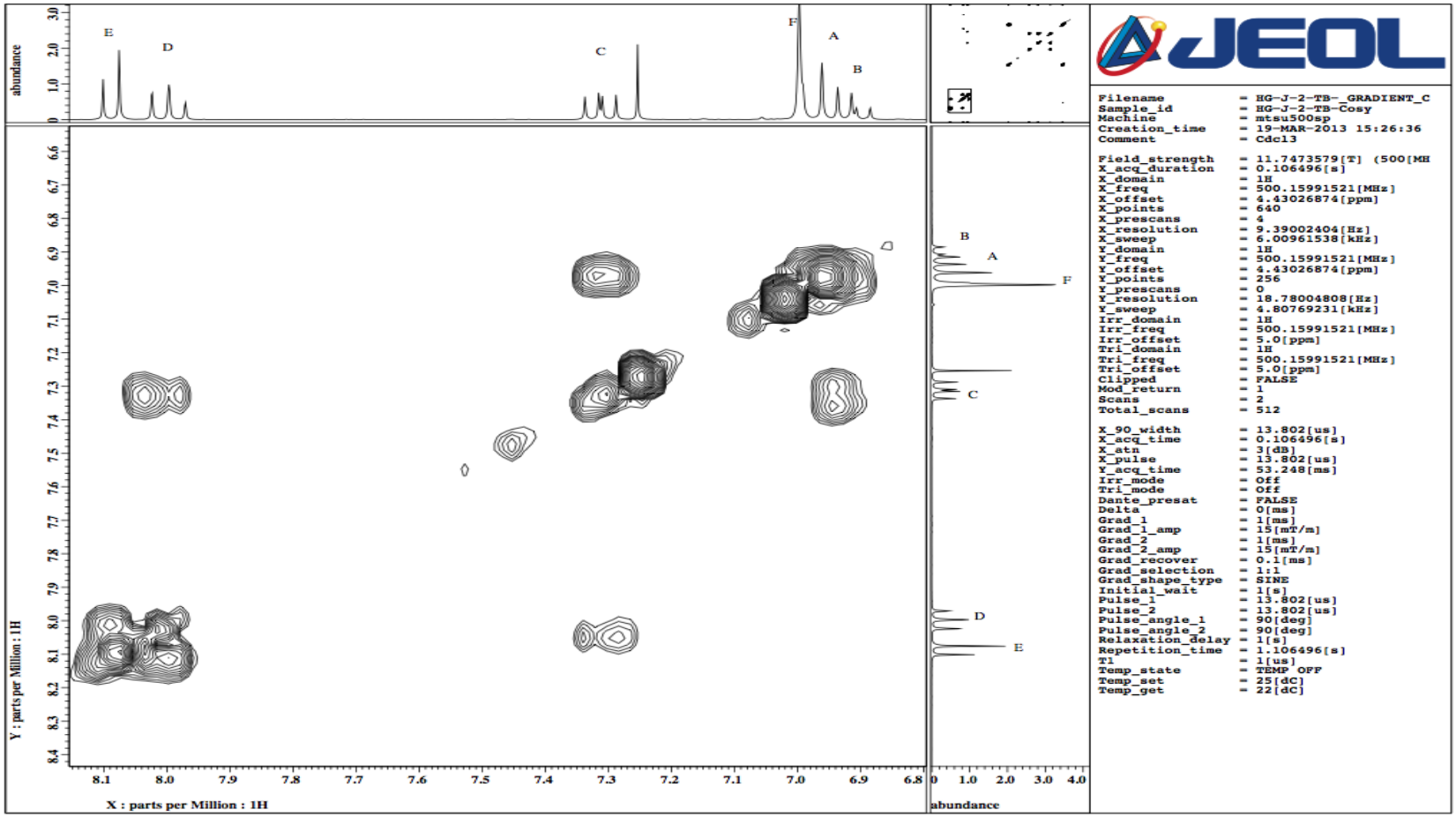

Figure B.21 ^{1}H-^{1}H COSY for compound **8** in $CDCl_3$.

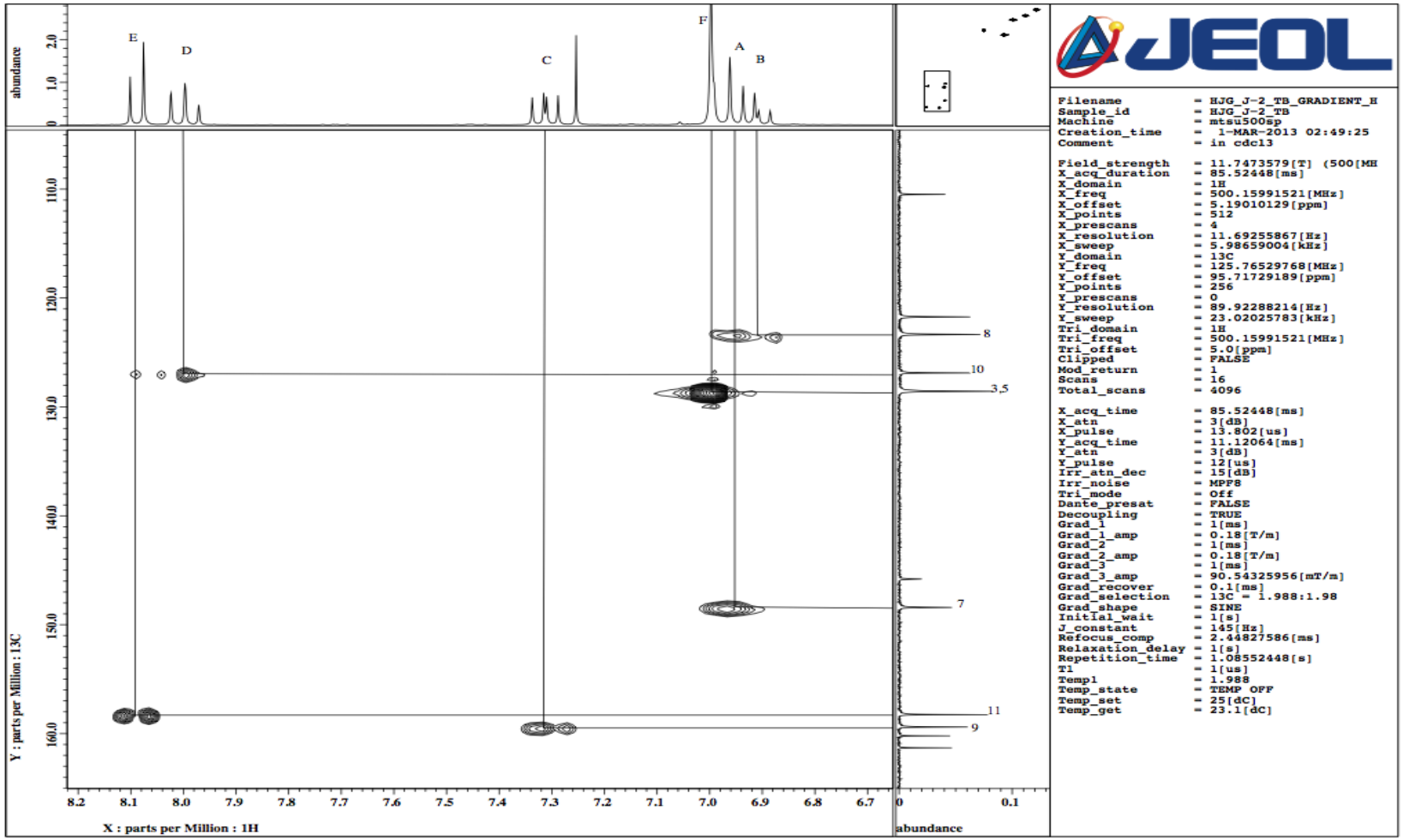

Figure B.22 HMQC for compound **8** in $CDCl_3$.

Table B.9 ^{1}H NMR Coupling Constants for compound **8**.

Solvent	AB	BA	BC	CB	CD	DC	DE	ED	ΔJ
CDCl3	14.9	14.9	10.9	10.9	13.8	13.2	13.2	12.6	2.3
DMSO	o	14.6	11.1	11.2	13.4	13.2	13.2	12.6	1.68
C_3D_6O	14.3	14.9	9.7	10.3	13.2	13.2	12.6	12.6	2.6
CD_3CN	o	o	o	o	o	13.2	13.1	12.6	-

Table B.10 ^{1}H NMR Chemical Shifts for compound **8**.

Solvent	A	B	C	D	E	F
$CDCl_3$	o	o	7.32	8.003	8.09	7.00
DMSO	7.25	o	7.68	7.93	8.03	7.23
C_3D_6O	7.16	o	7.51	7.96	8.03	7.23
CD_3CN	o	o	o	7.97	8.06	7.13

Compound **1:** 2-(3-cyano-4-((1E,3E,5E)-6-(4-(dimethylamino)phenyl)hexa-1,3,5-trienyl)-5,5-dimethylfuran-2(5H)-ylidene)malonitrile

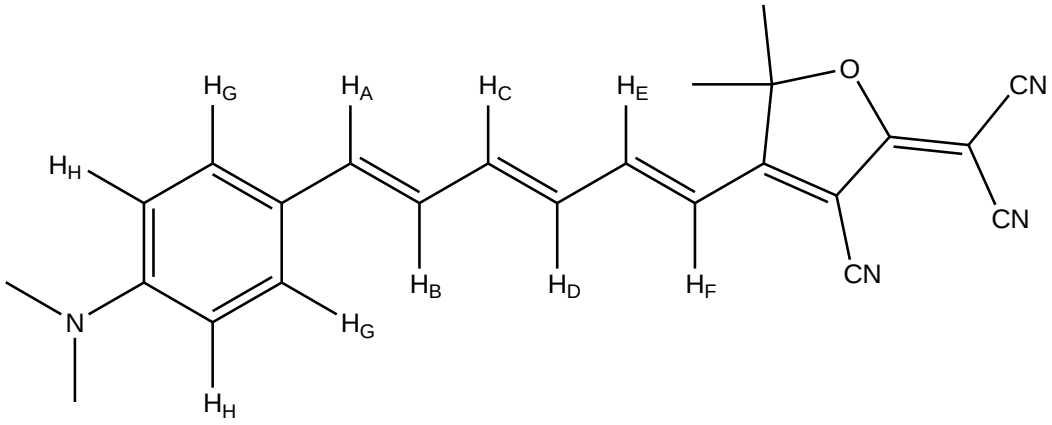

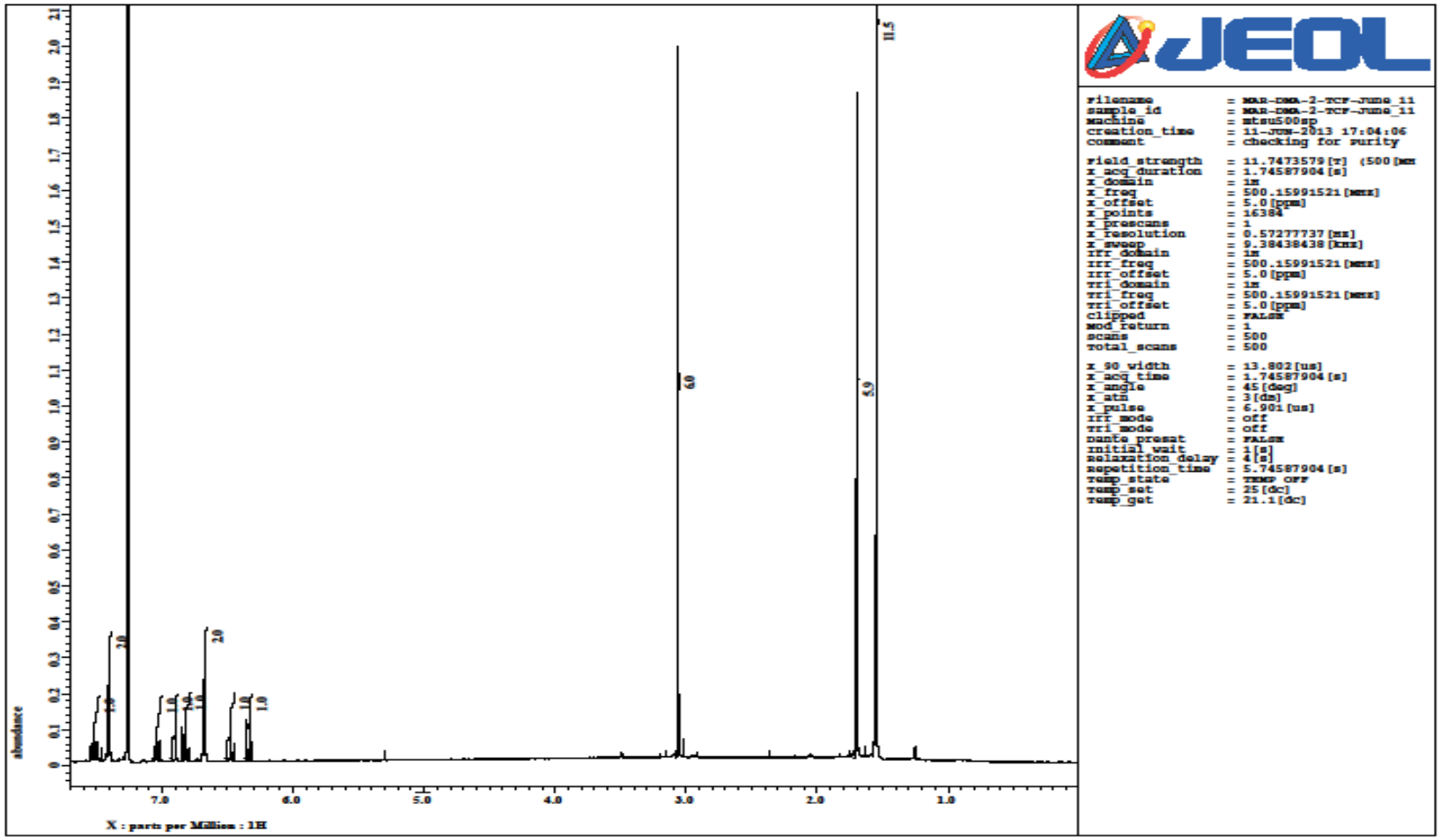

Figure B.22 ^{1}H NMR spectrum for compound **1** in $CDCl_3$.

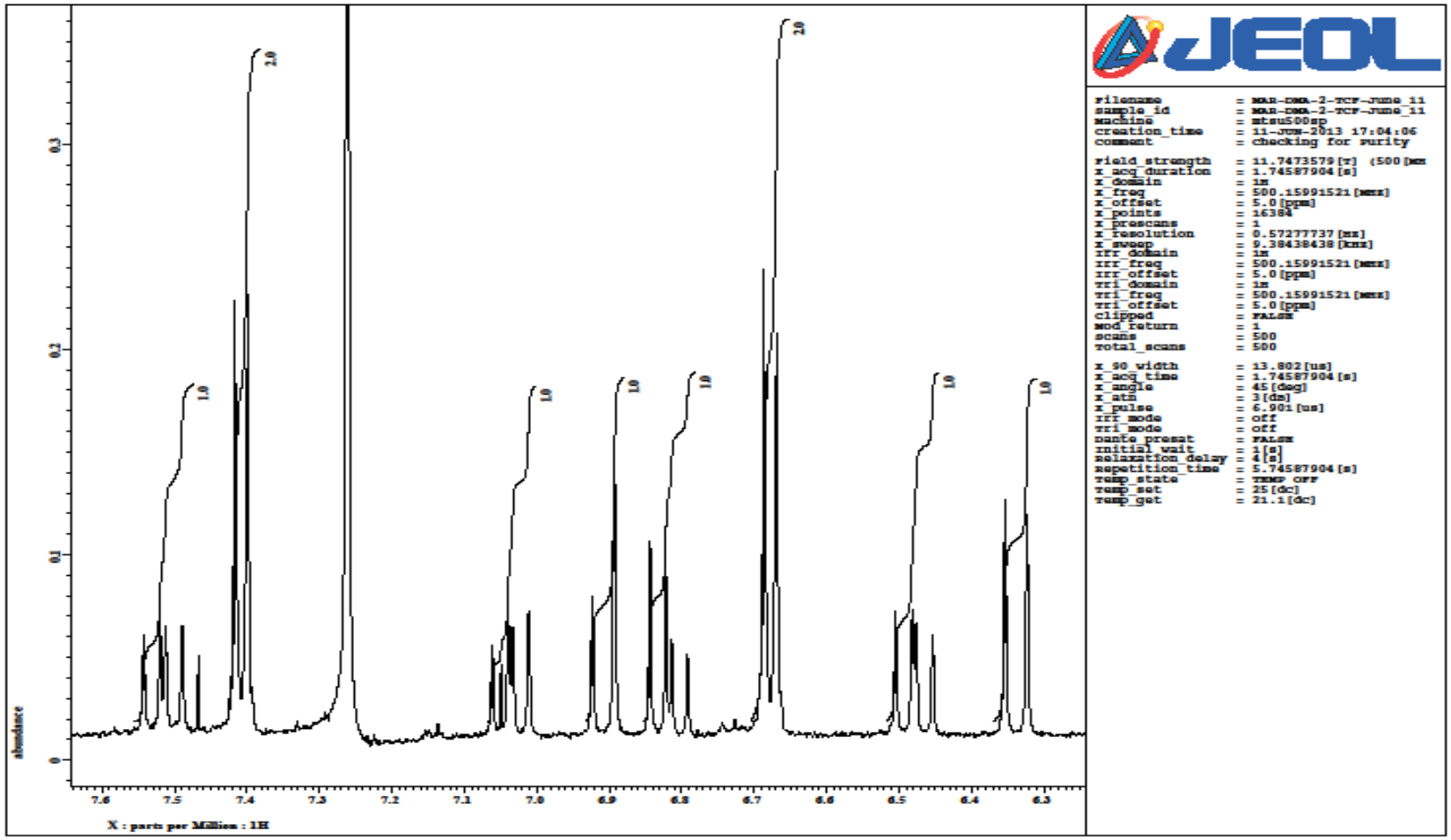

Figure B.23 ^{1}H NMR spectrum zoomed in for compound **1** in $CDCl_3$.

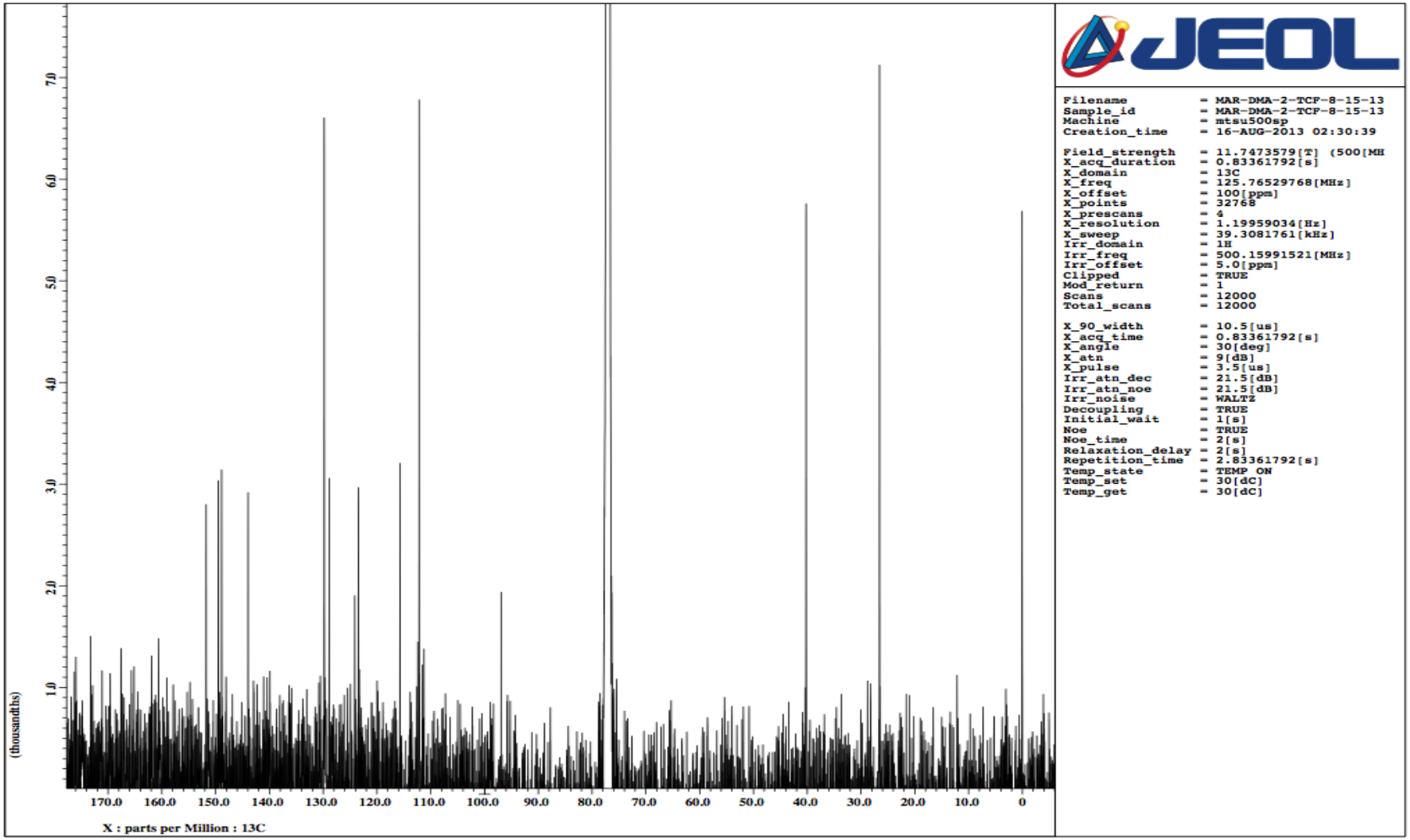

Figure B.23 ^{13}C NMR spectrum for compound **1** in $CDCl_3$.

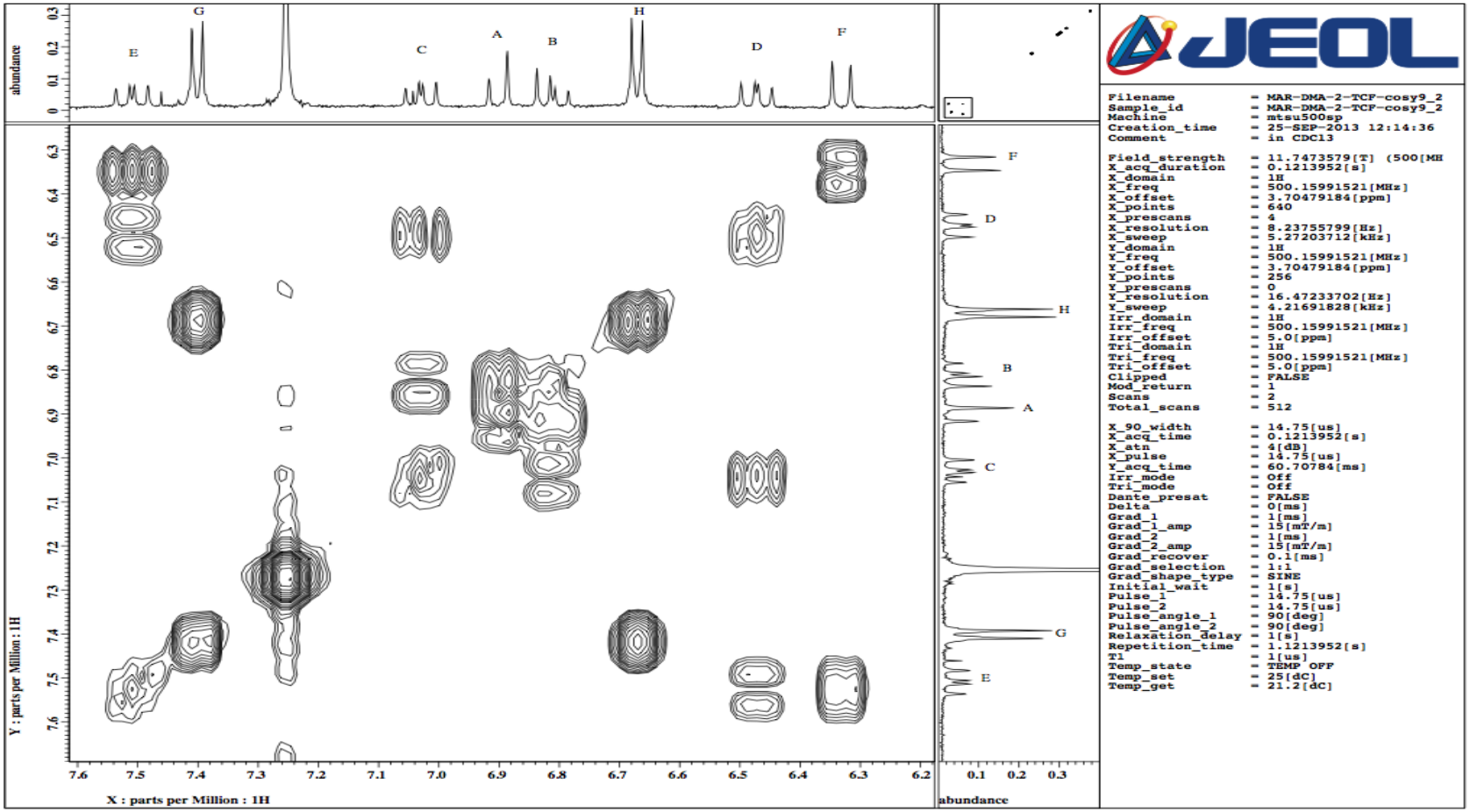

Figure B.24 ^{1}H-^{1}H COSY spectrum for compound **1** in $CDCl_3$.

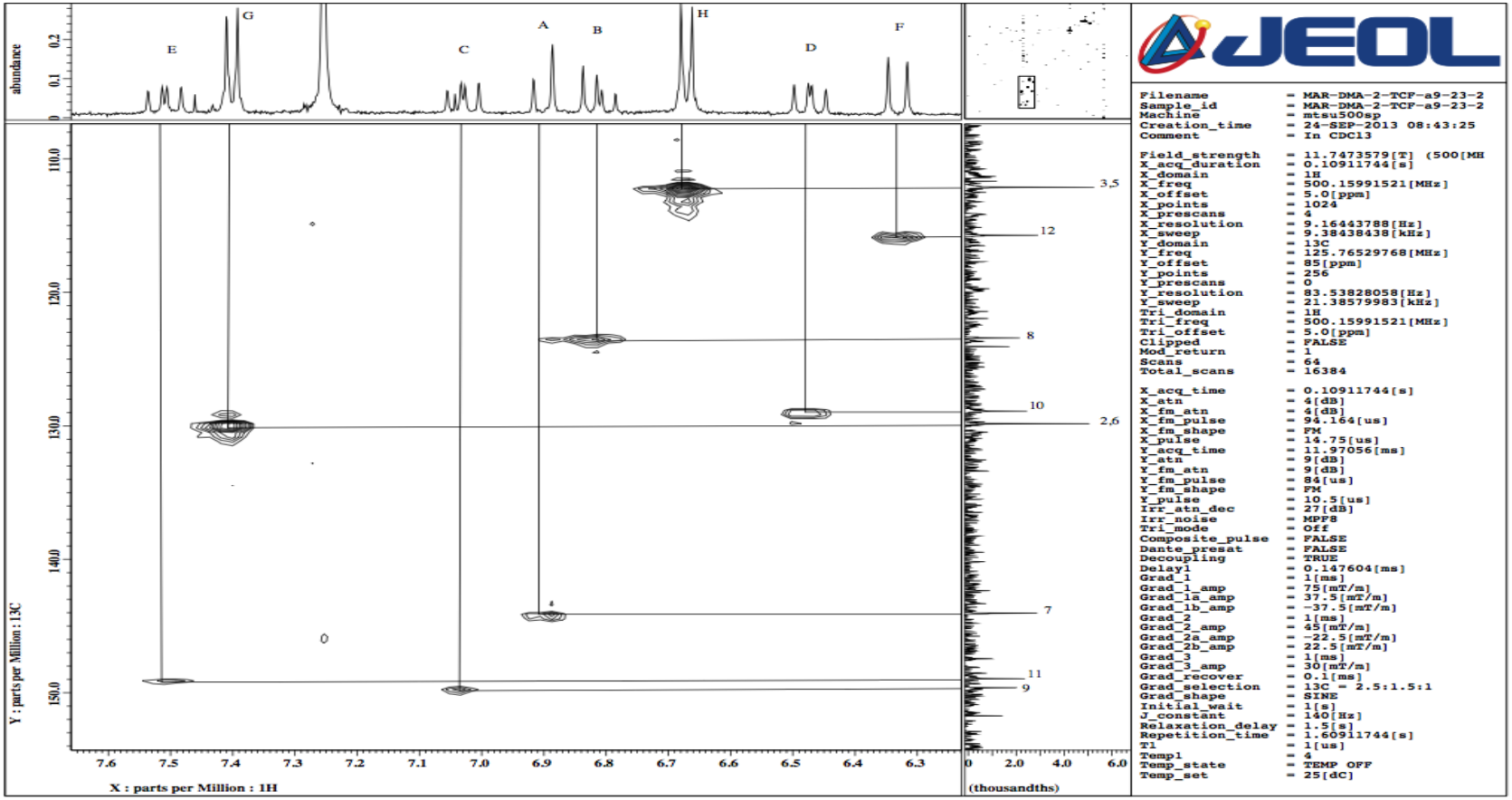

Figure B.25 HSQC spectrum for compound **1** in $CDCl_3$

Table B.11 ^{1}H NMR coupling constants for compound **1**.

Solvent	AB	BA	BC	CB	CD	DC	DE	ED	EF	FE	ΔJ
$CDCl_3$	15.5	14.9	10.9	11.2	14.0	14.3	11.4	11.5	14.9	15.5	3.6
C_3D_6O	o	o	o	o	o	14.9	10.9	11.2	15.2	15.2	-
DMSO	o	o	o	o	o	10.3	10.4	11.4	15.2	15.0	-

Table B.12 ^{1}H NMR Chemical Shifts for compound **1**.

Solvent	A	B	C	D	E	F	G	H
$CDCl_3$	6.91	6.82	7.04	6.48	7.52	6.34	7.41	6.68
C_3D_6O	7.07	o	o	o	7.84	6.66	7.51	6.79
DMSO	o	o	7.34	o	7.78	6.61	7.53	6.77

Compound **2:** 2-(3-cyano-5,5-dimethyl-4-((1E,3E,5E)-6-(1-methylindolin-5-yl)hexa-1,3,5-trienyl)furan-2(5H)-ylidene)malononitrile

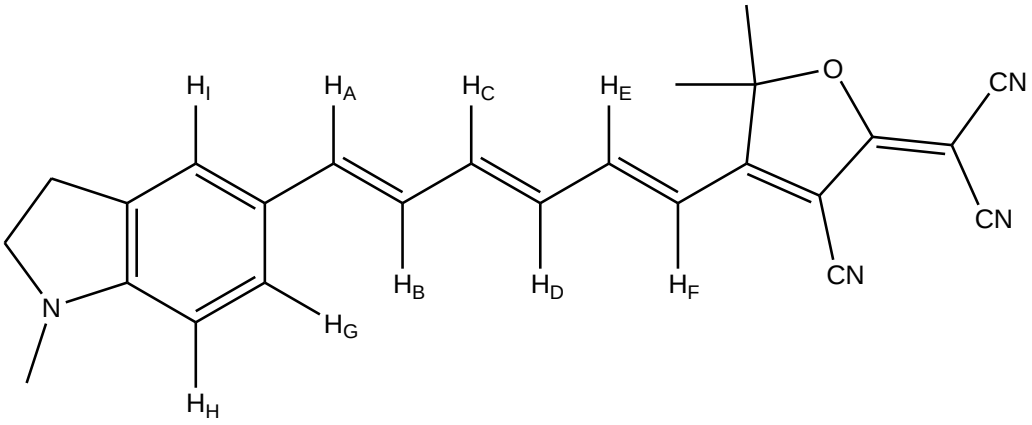

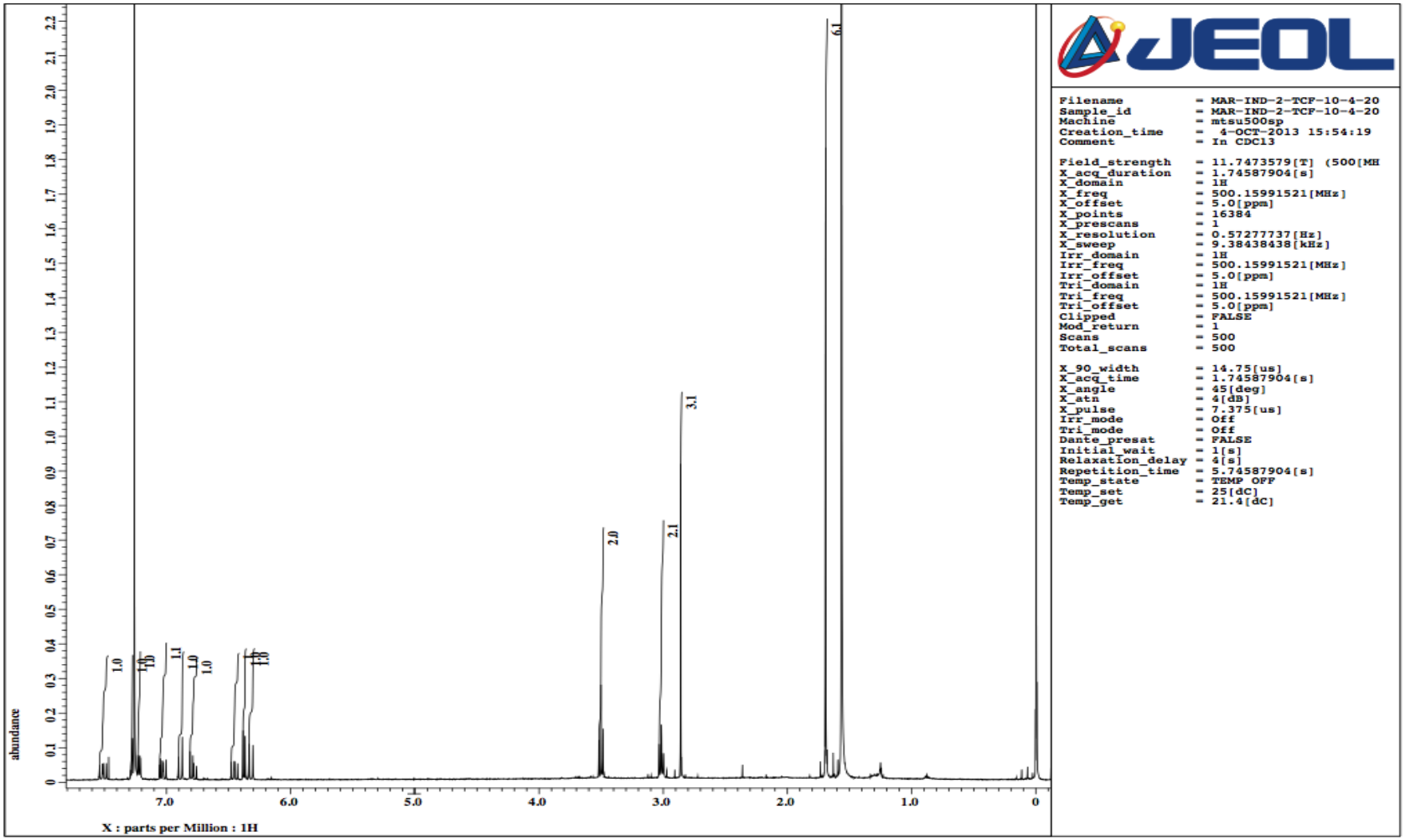

Figure B.26 ^{1}H NMR spectrum for compound **2** in $CDCl_3$.

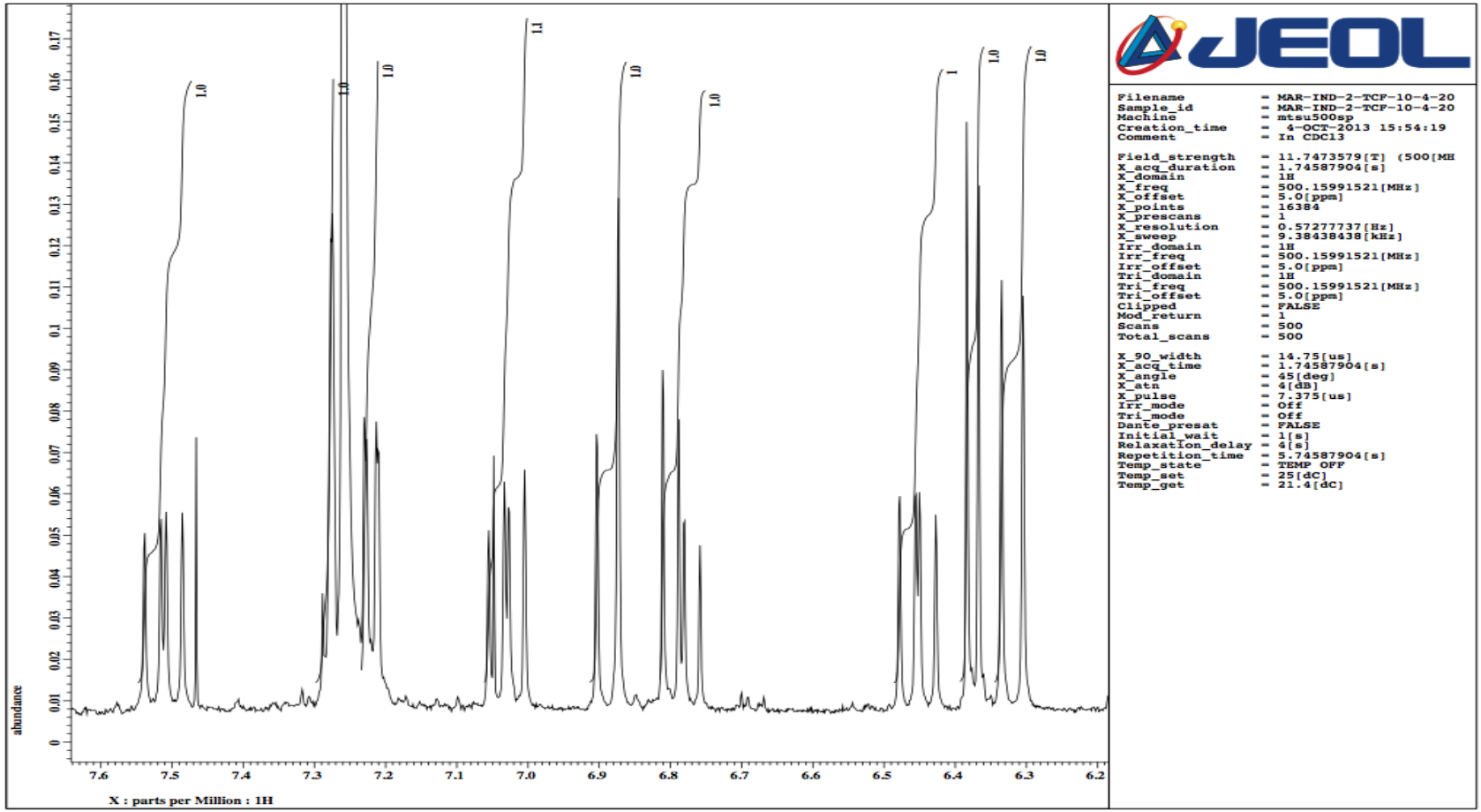

Figure B.27 ^{1}H NMR spectrum focused at vinyl and benzyl region for compound **2** in $CDCl_3$.

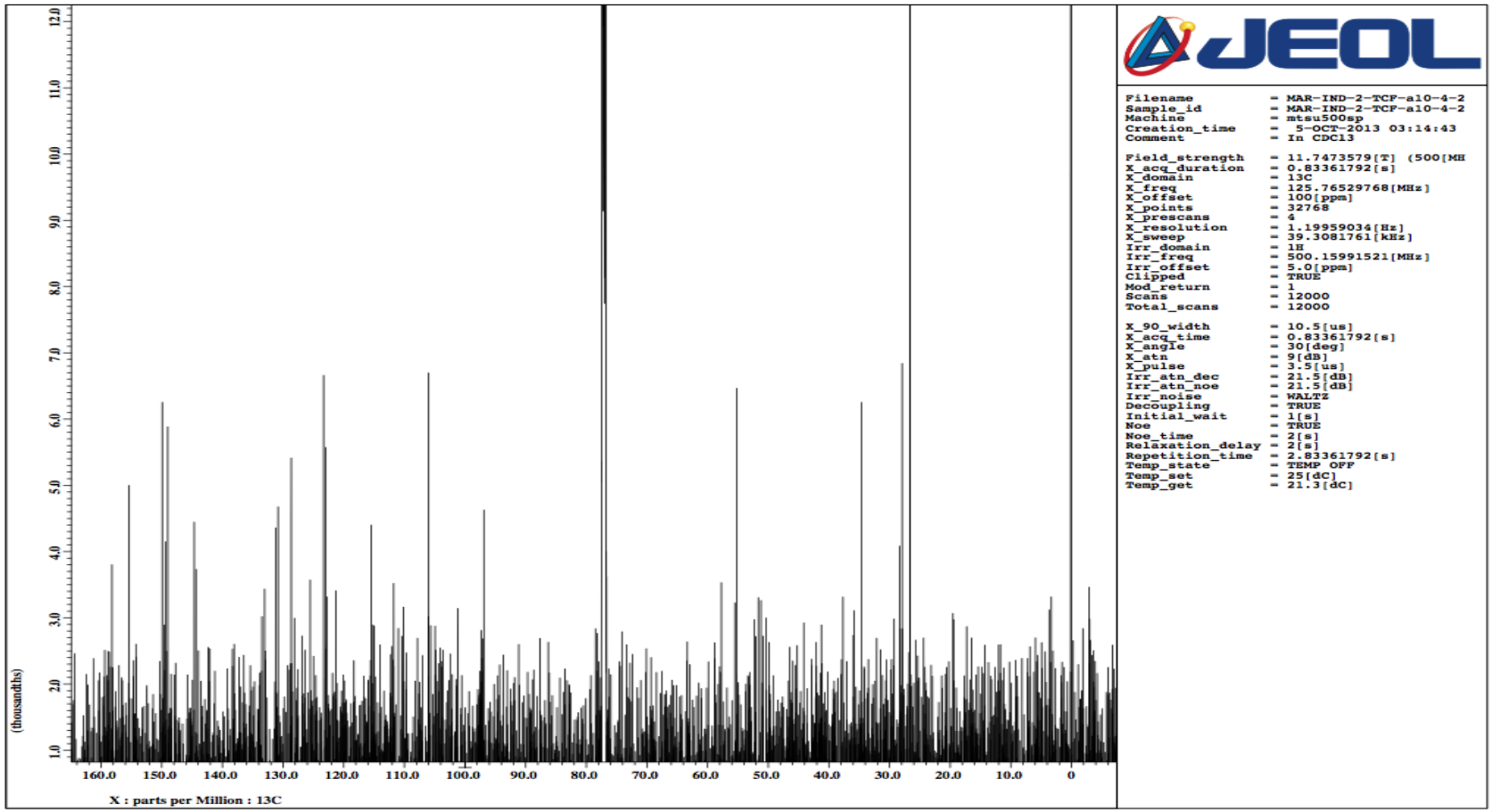

Figure B.28 ^{13}C NMR spectrum for compound **2** in $CDCl_3$.

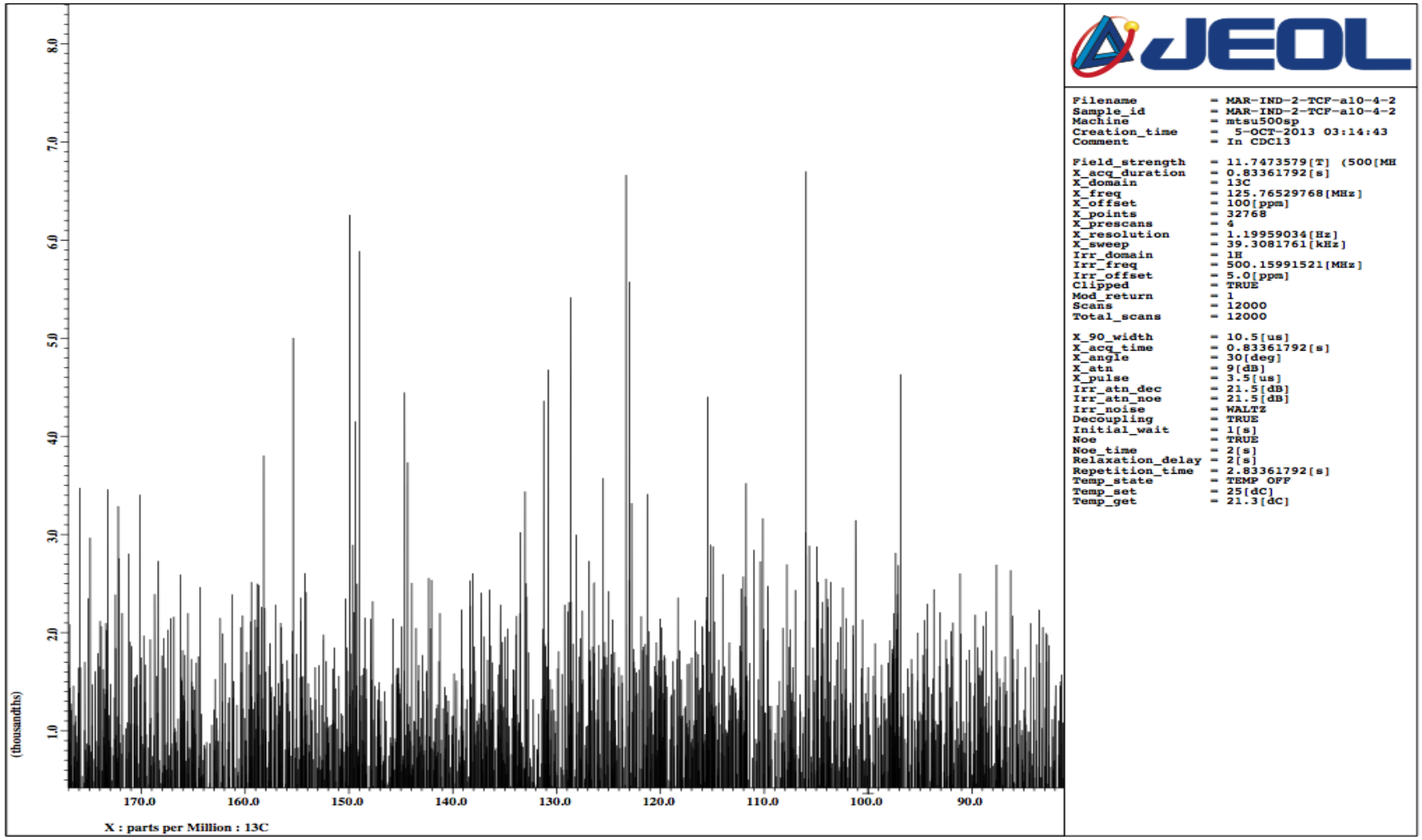

Figure B.29 ^{13}C NMR spectrum for compound **2** in $CDCl_3$. Spectrum zoomed in at 80 – 177 ppm.

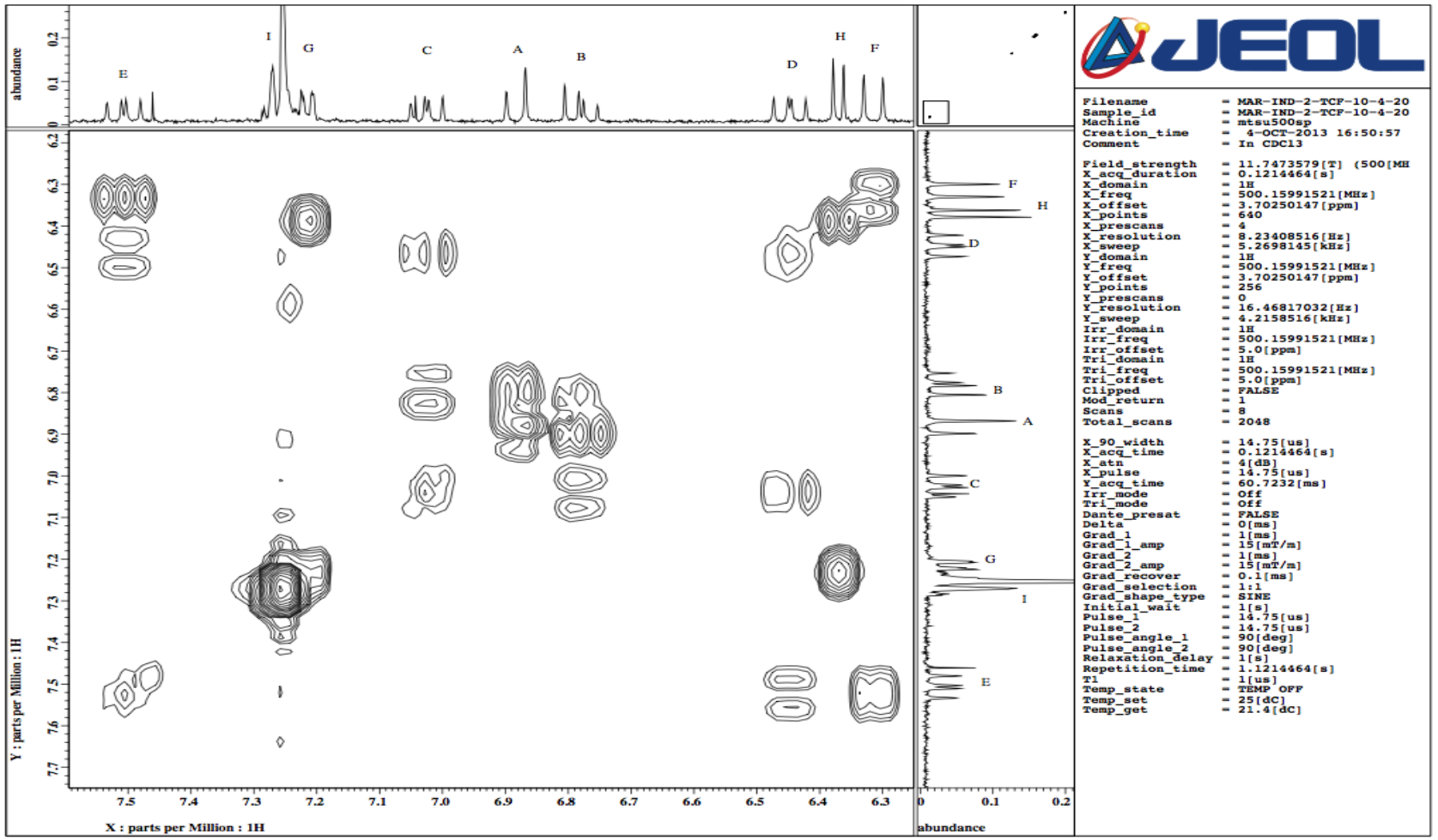

Figure B.30 ^{1}H-^{1}H COSY spectrum for compound **2** in $CDCl_3$.

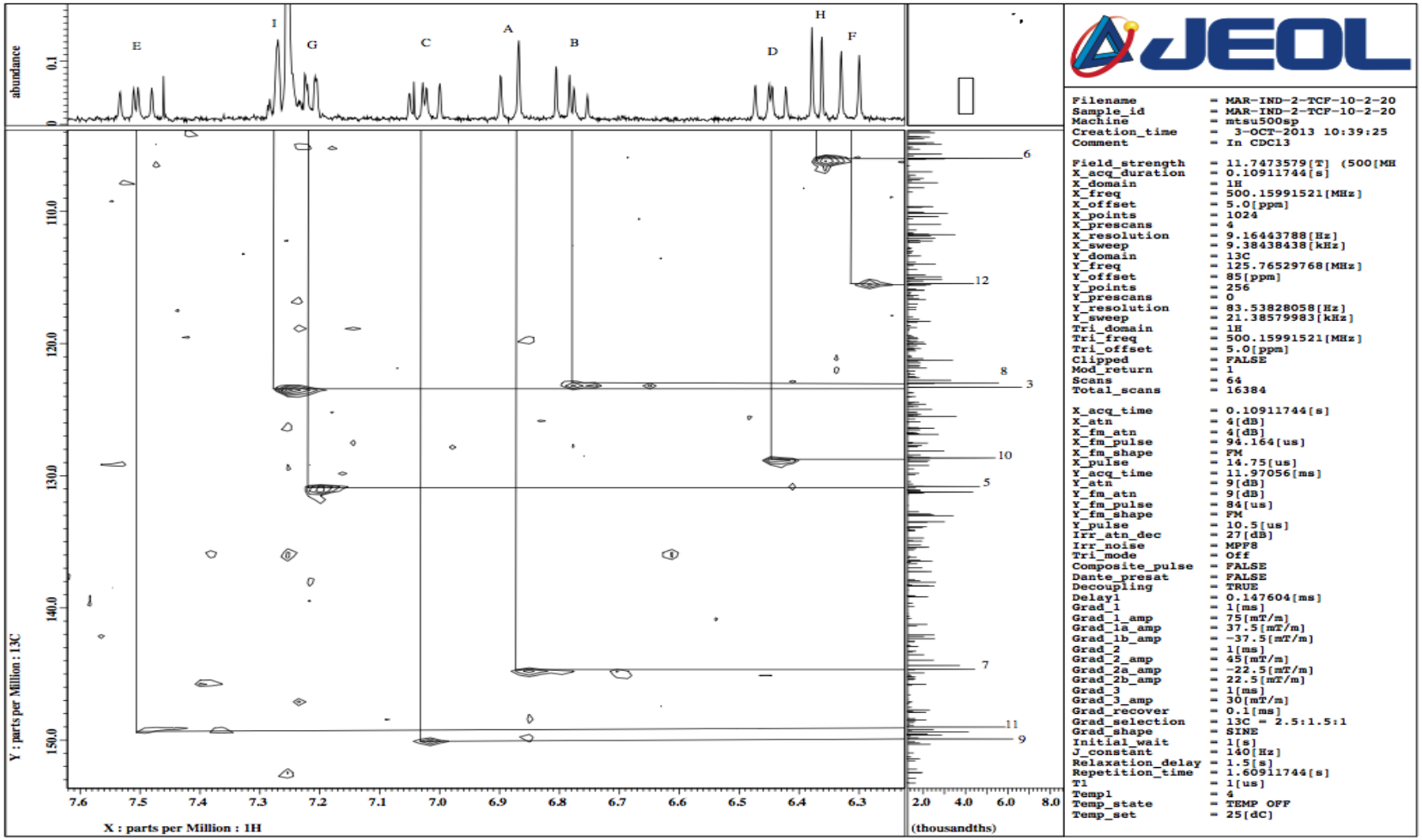

Figure B.31 HSQC of compound **2** in $CDCl_3$.

Compound **3:** 2-(3-cyano-5,5-dimethyl-4-((1E,3E,5E)-6-(1-methyl-1,2,3,4-tetrahydroquinolin-6-yl)hexa-1,3,5-trienyl)furan-2(5H)-ylidene)malononitrile

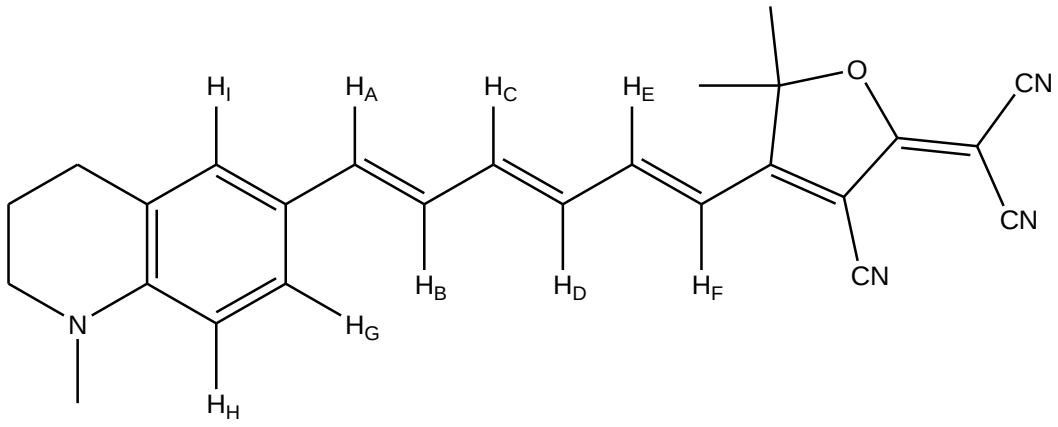

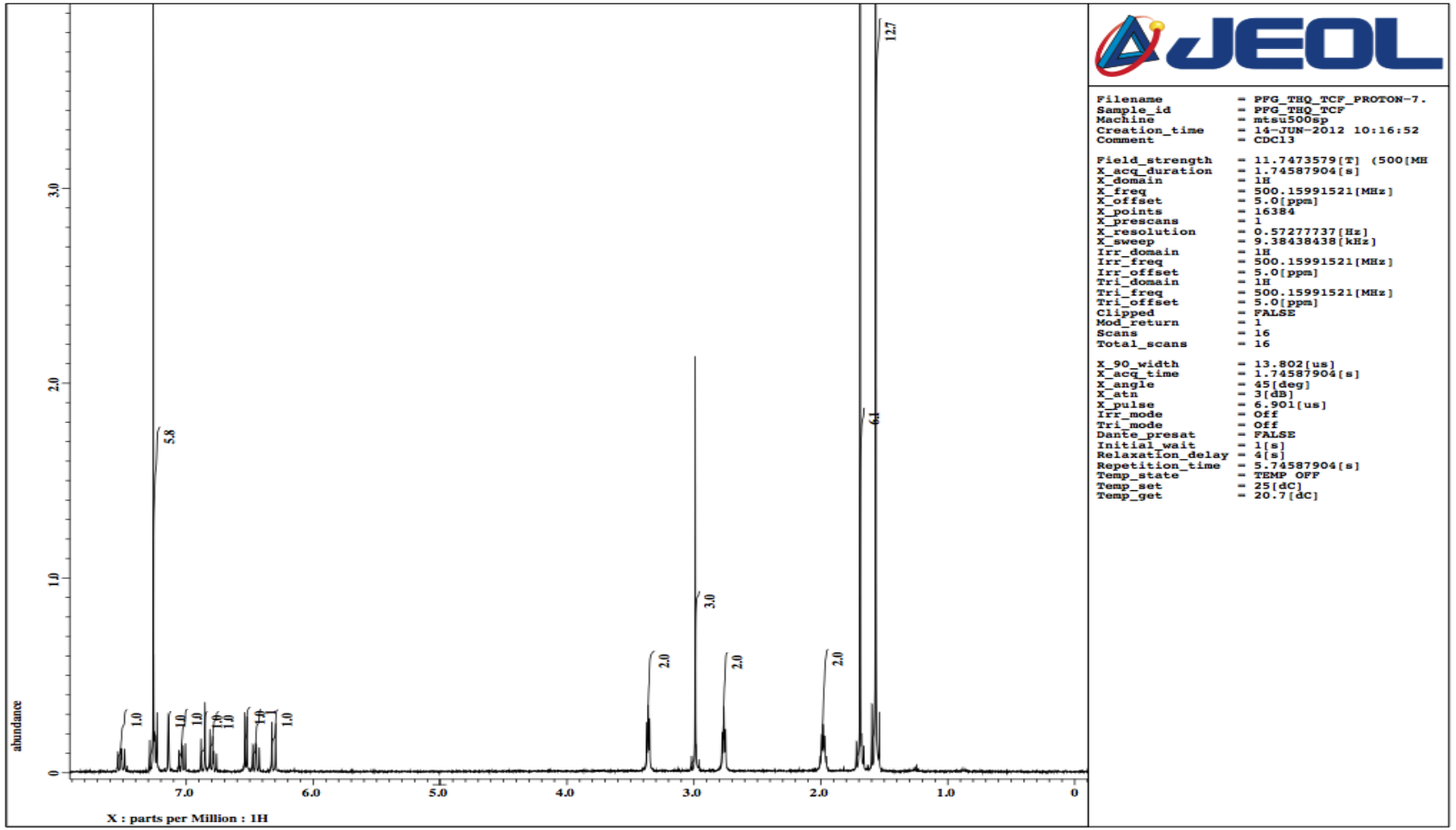

Figure B.32 ^{1}H NMR spectrum for compound **3** in $CDCl_3$.

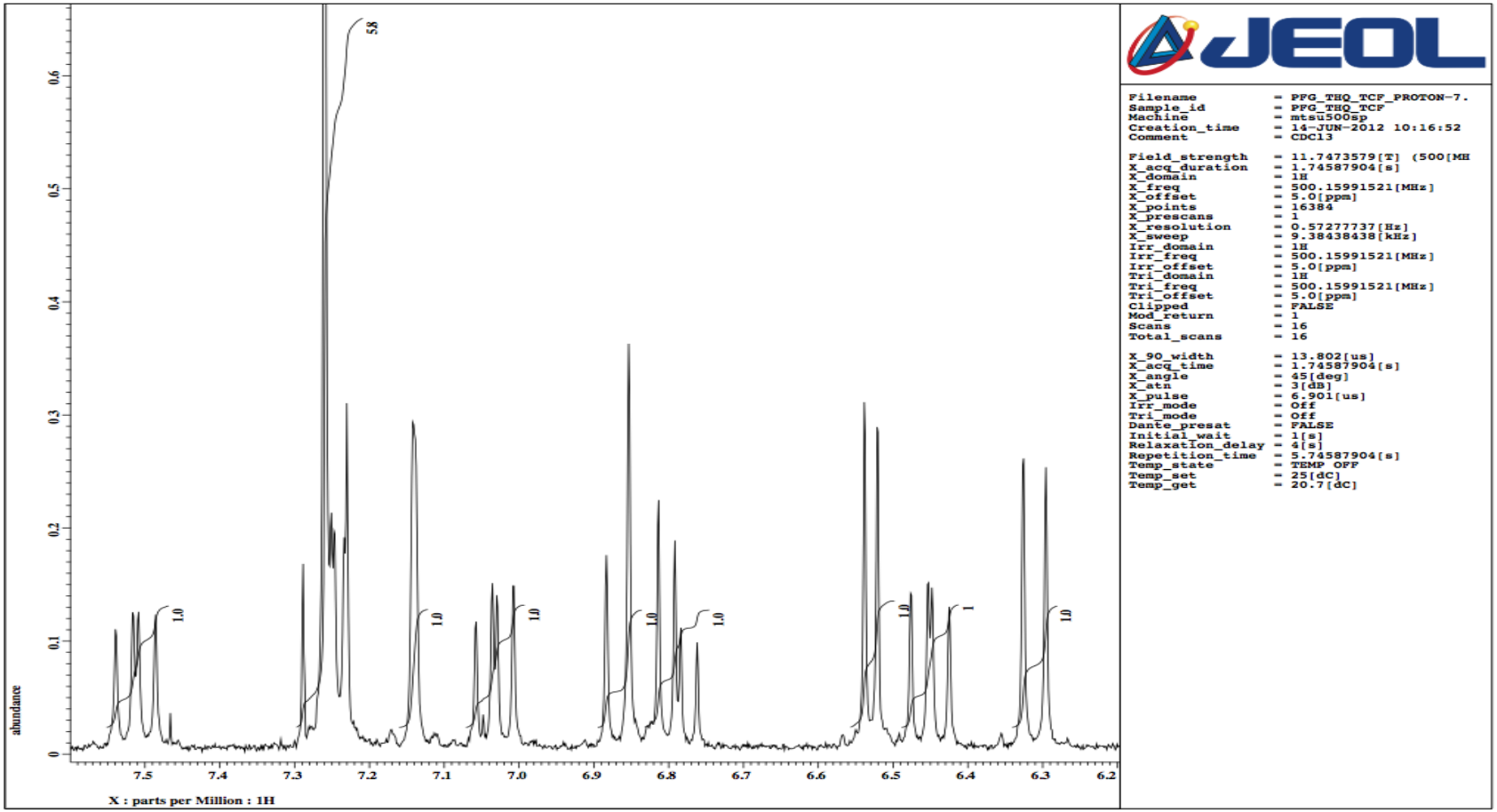

Figure B.33 ^{1}H NMR spectrum focused at vinyl and benzyl region for compound **3** in $CDCl_3$.

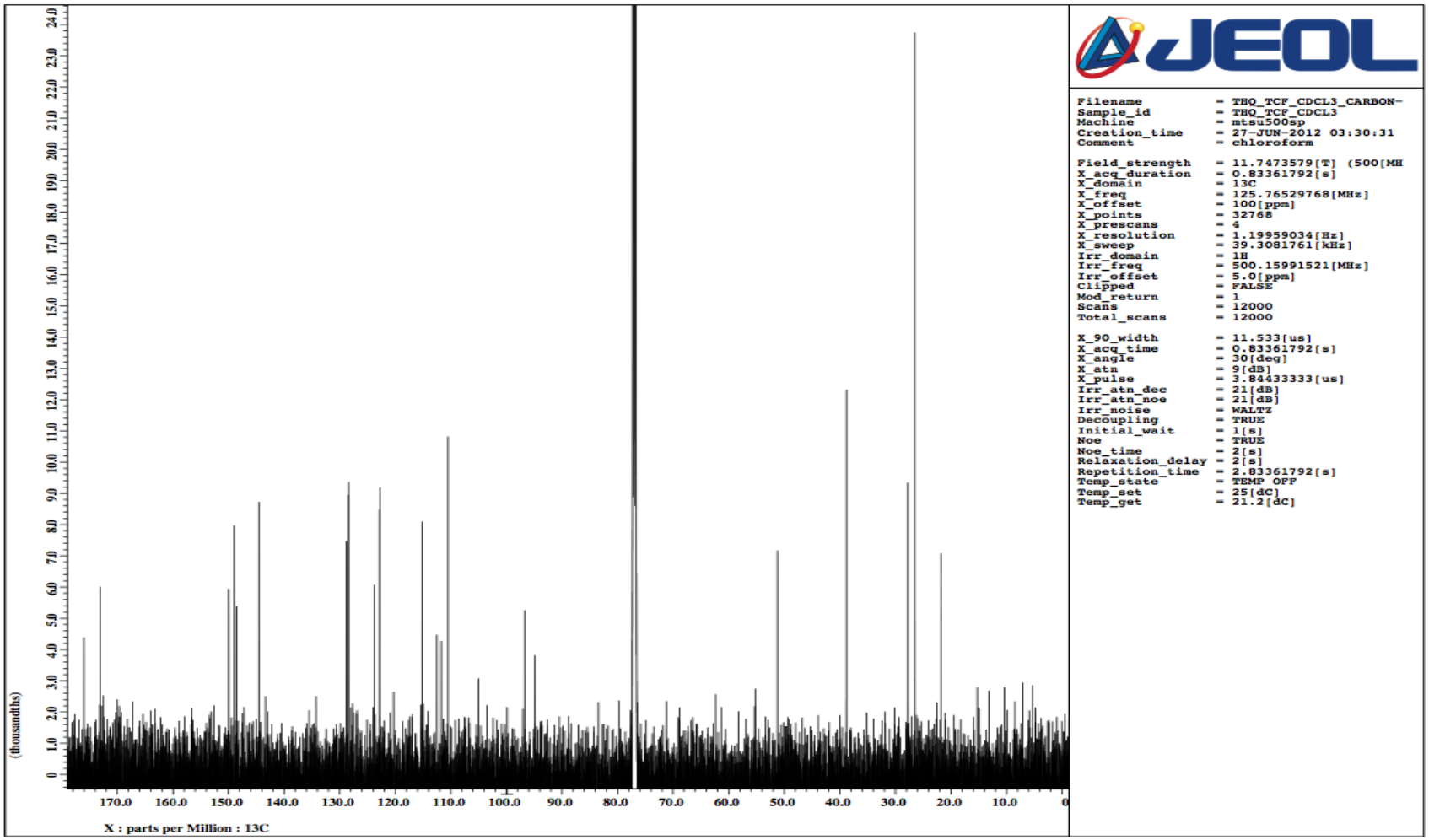

Figure B.34 ^{13}C NMR spectrum of compound **3** in $CDCl_3$.

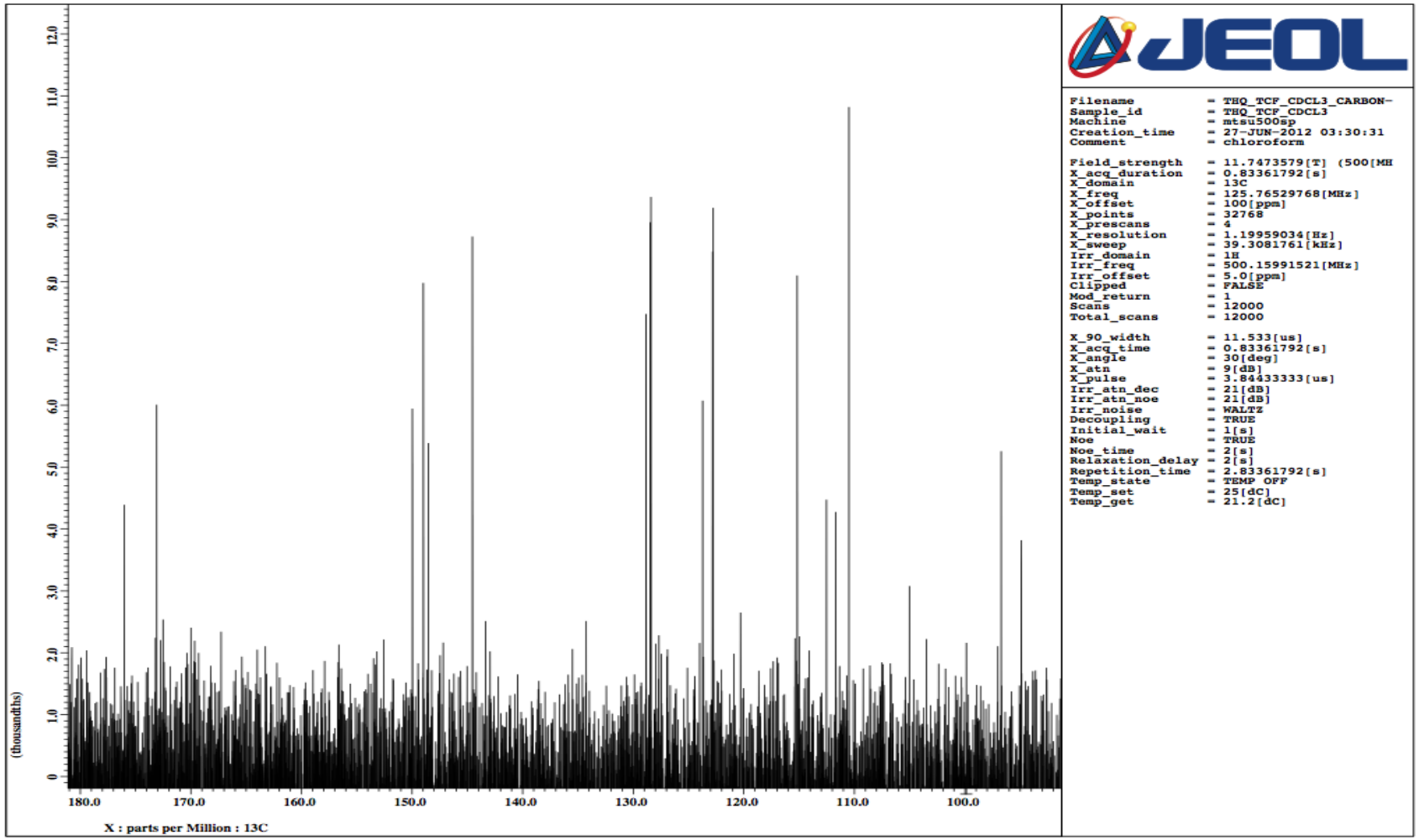

Figure B.35 ^{13}C NMR spectrum of compound **3** in $CDCl_3$. Spectrum zoomed in at 90- 180 ppm.

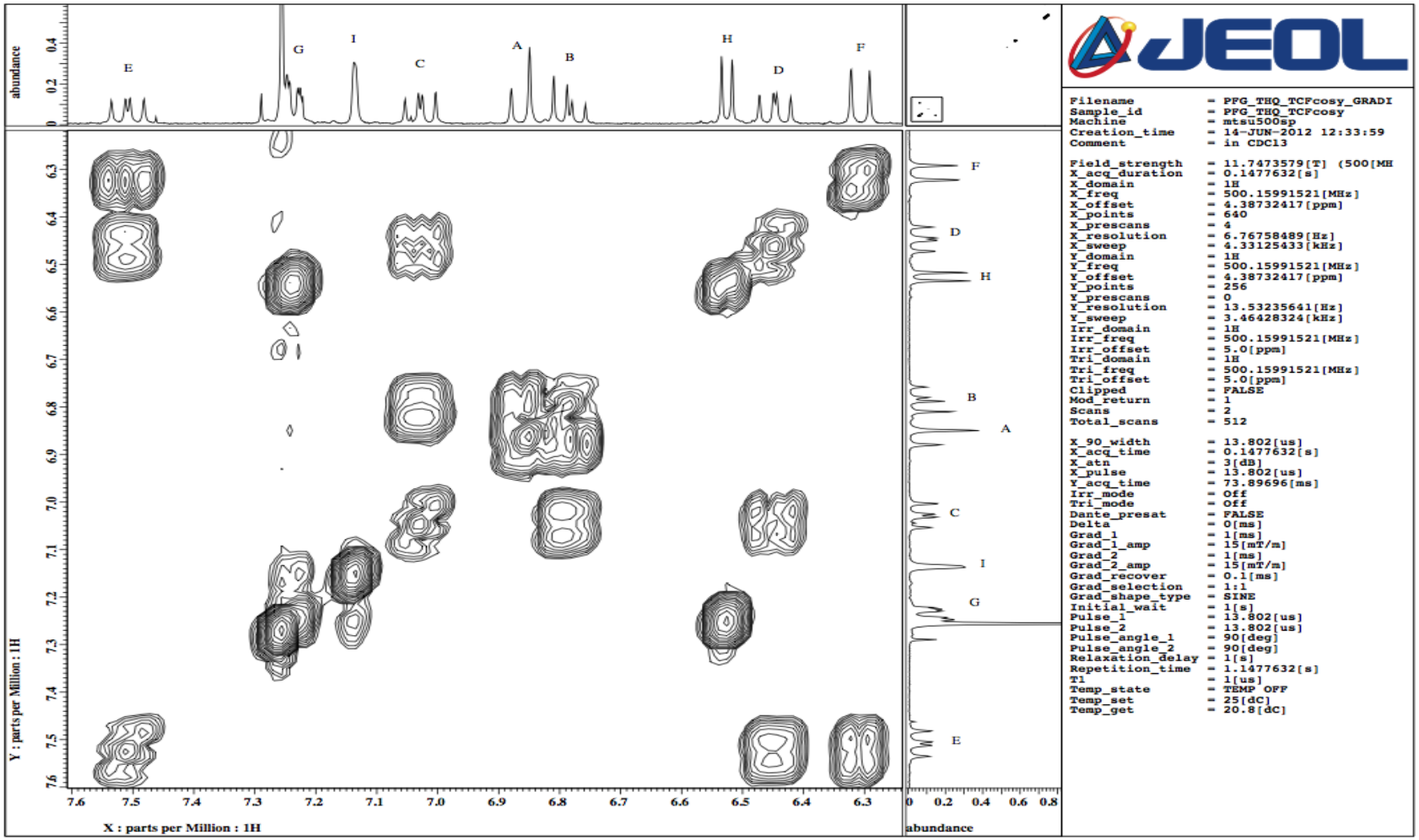

Figure B.36 ^{1}H-^{1}H COSY spectrum for compound **3** in $CDCl_3$.

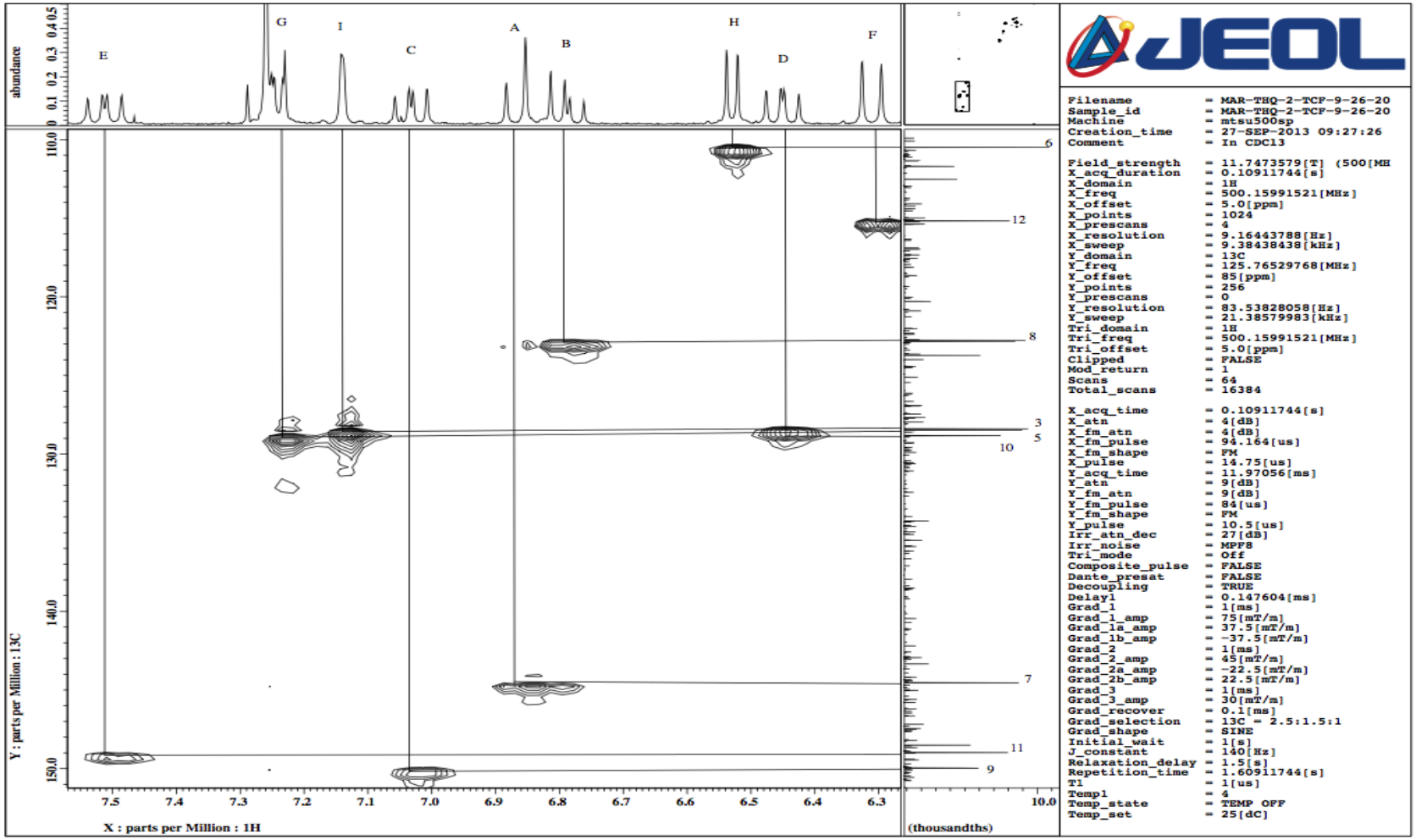

Figure B.37 HSQC spectrum of compound **3** in $CDCl_3$.

Compound **4**: 6-(4-Julolidin-4-yl)-2,4,6-hexatrienyl-tricyanofuran

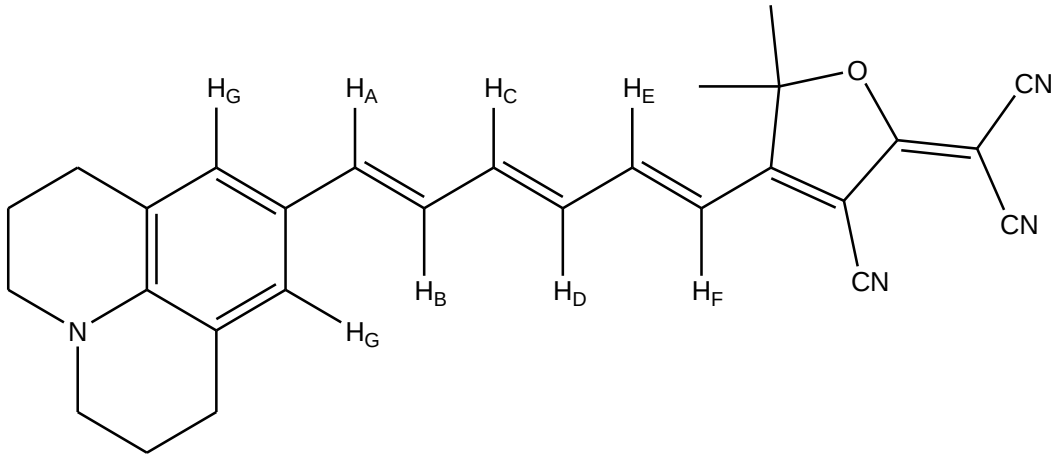

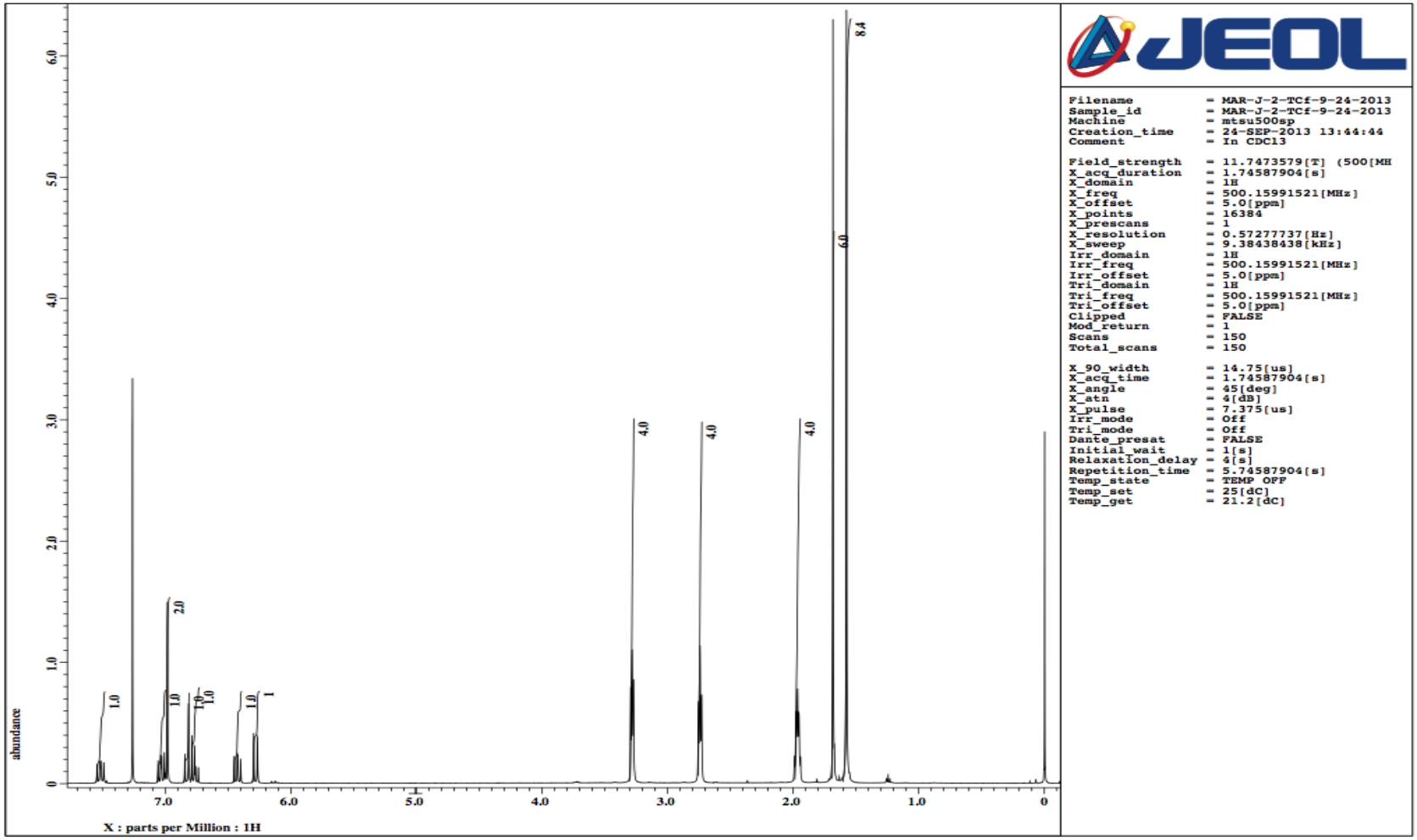

Figure B.38 ^{1}H NMR spectrum for compound **4** in $CDCl_3$.

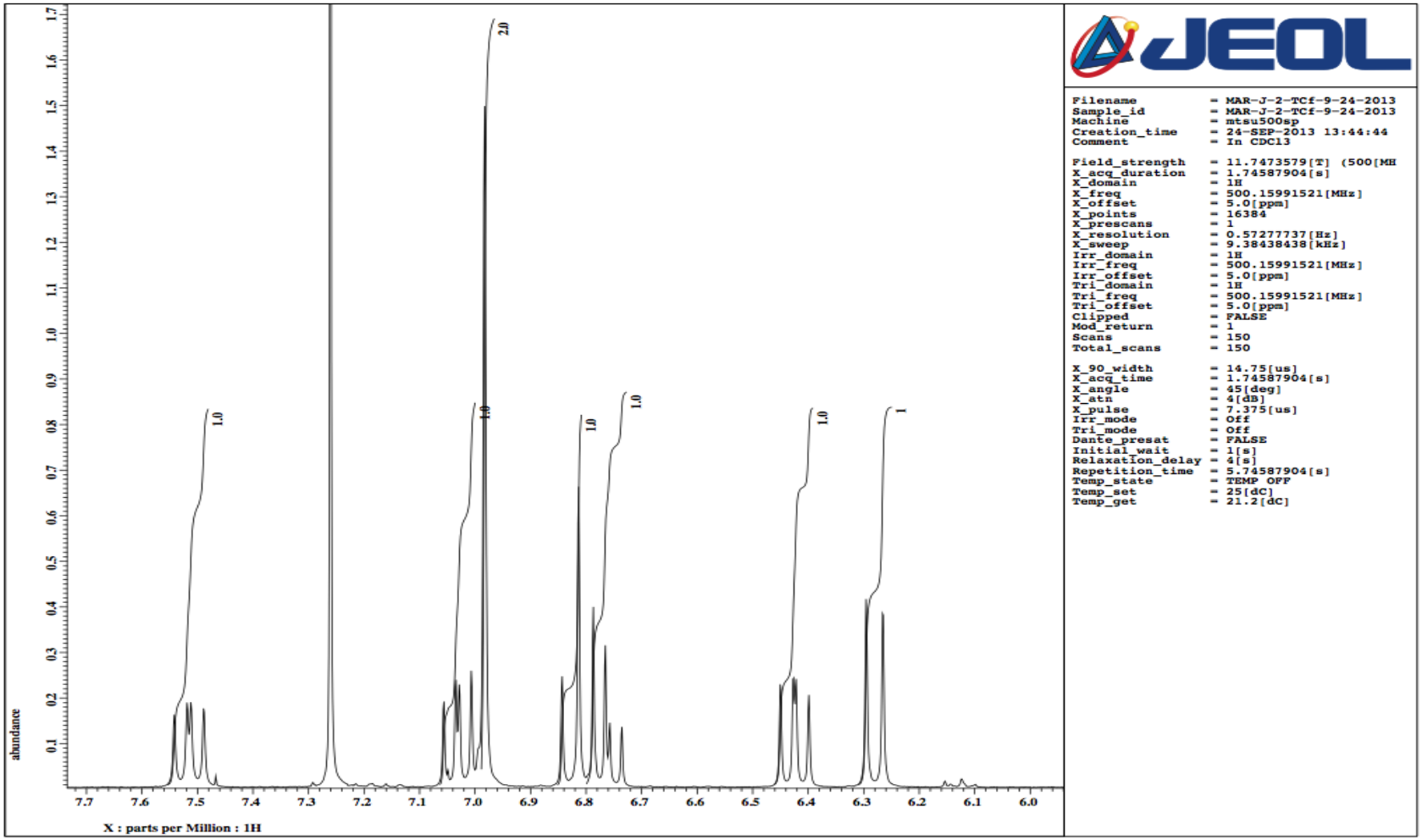

Figure B.39 ^{1}H NMR spectrum focused at vinyl and benzyl region for compound **4** in $CDCl_3$.

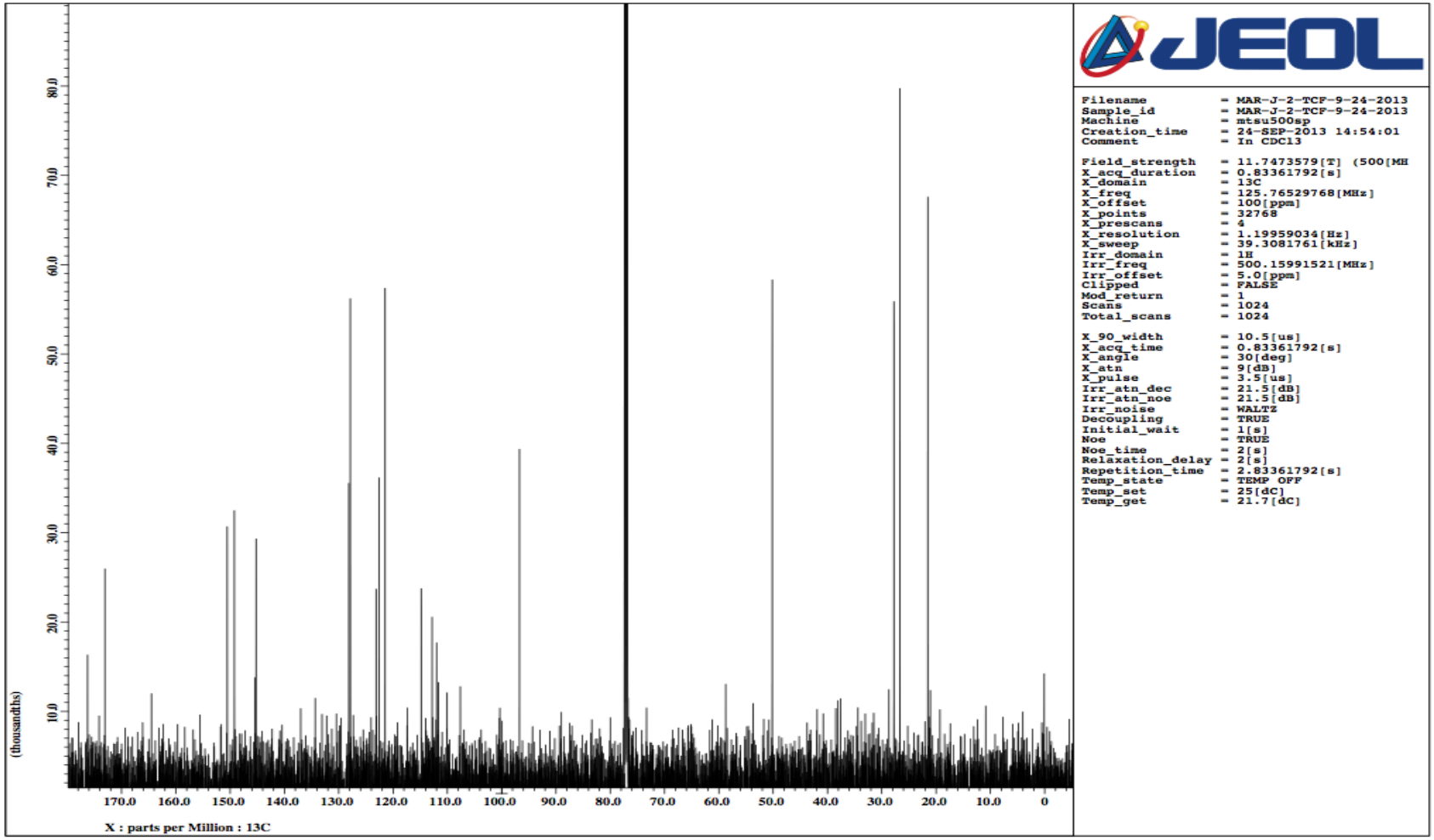

Figure B.40 ^{13}C NMR spectrum for compound **4** in $CDCl_3$.

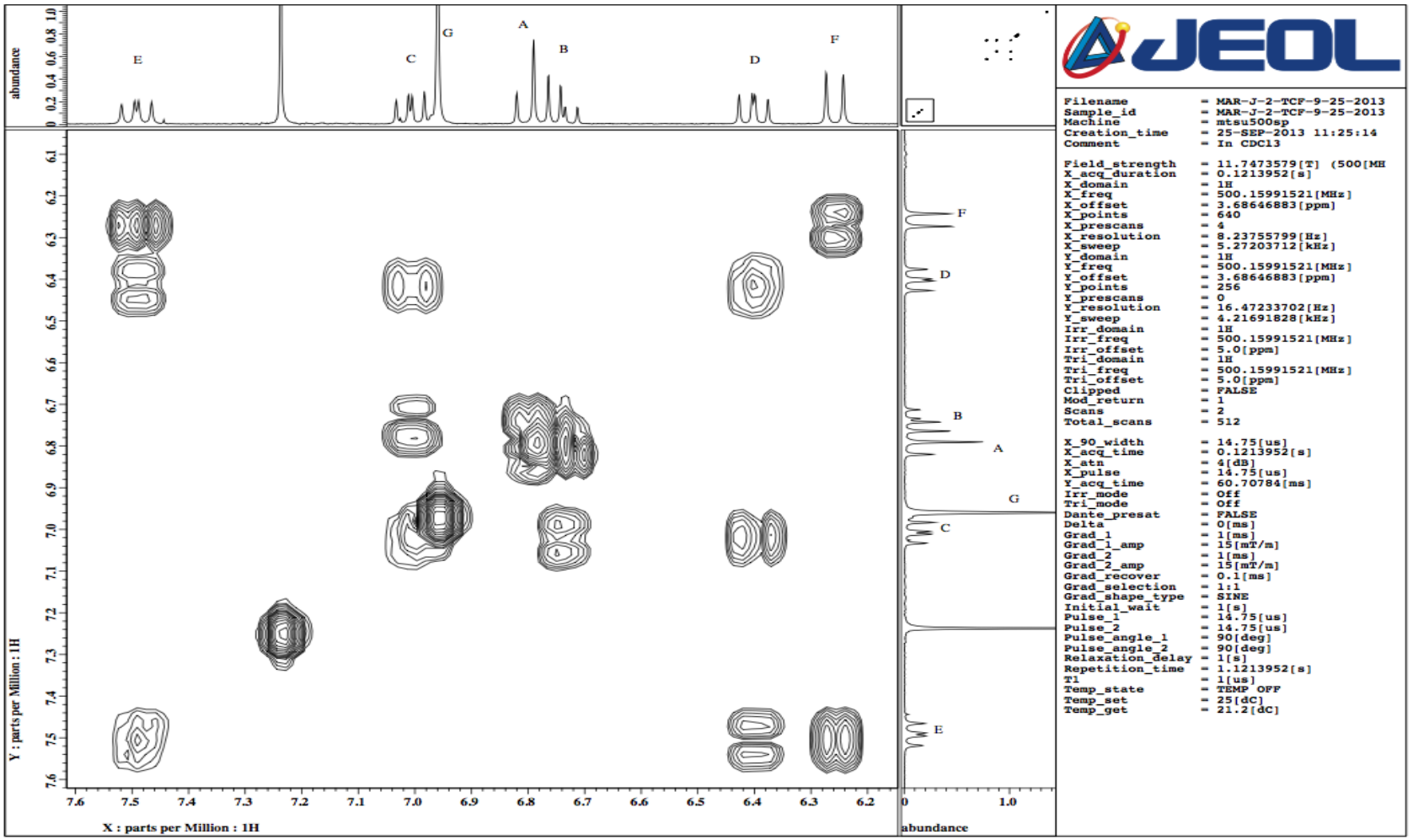

Figure B.41 ^{1}H-^{1}H COSY spectrum for compound **4** in $CDCl_3$.

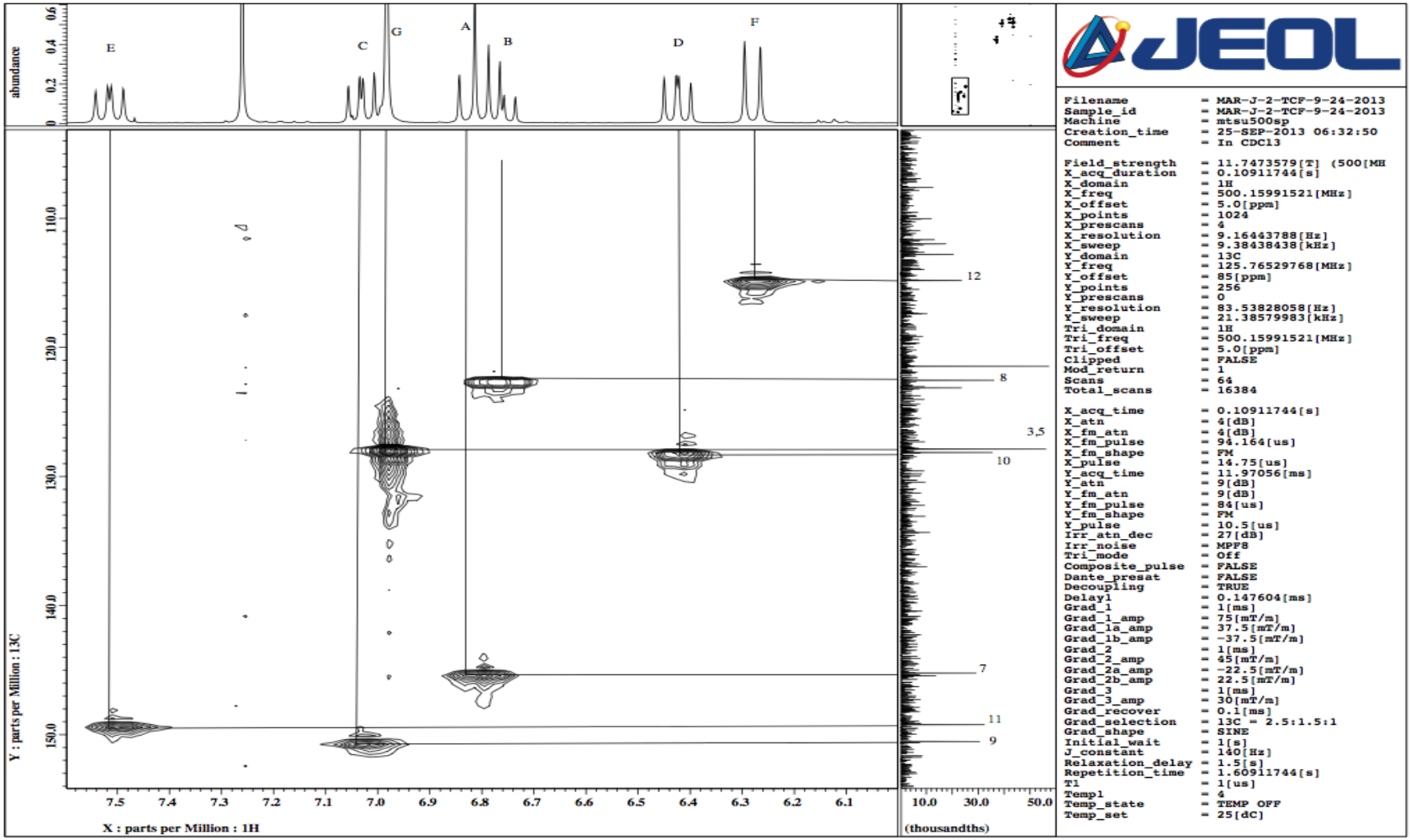

Figure B.42 HSQC spectrum for compound **4** in CDCl

Table B.15 ^{1}H NMR coupling constants for compound **4**.

Solvent	AB	BA	BC	CB	CD	DC	DE	ED	EF	FE	ΔJ
$CDCl_3$	14.9	14.6	10.6	10.9	14.4	13.8	11.5	11.5	14.9	15.5	3.56
C_3D_6O	o	o	o	o	o	13.2	o	12.9	14.7	15.4	n/a
DMSO	o	o	o	o	14.0	14.3	11.5	11.4	14.9	14.9	3.08

Table B.16 ^{1}H NMR Chemical Shifts for compound **4**.

Solvent	A	B	C	D	E	F	G
$CDCl_3$	6.83	6.76	7.03	6.43	7.51	6.28	6.98
C_3D_6O	o	o	7.30	6.73	7.84	6.64	7.06
DMSO	6.98	6.98	7.36	6.67	7.78	6.52	7.11

Table B.17 ^{13}C NMR Chemical Shifts for Compounds **1** - **4**.

Carbon Number	**1**	**2**	**3**	**4**
1	151.74	o	148.39	145.42
2	112.15	105.91	110.44	121.46
3	129.81	130.73	128.85	127.88
4	124.12	o	123.70	123.10
5	129.81	123.27	128.40	127.88
6	112.15	o	122.74	121.46
7	143.95	144.57	144.51	145.23
8	123.42	122.94	122.80	122.55
9	149.50	149.91	148.89	150.53
10	128.89	128.71	128.47	128.15
11	148.87	148.95	148.96	149.23
12	115.72	115.41	115.23	114.78
13	173.25	o	173.09	173.05
14	o	o	111.72	o
15	o	o	115.23	o
16	176.13	o	175.85	176.13

Table B.18 ^{13}C NMR Chemical Shifts for Compounds **5** - **8**.

Carbon Number	**5**	**6**	**7**	**8**
1	152.01	155.74	148.71	145.69
2	112.02	105.76	111.06	121.62
3	130.36	131.16	129.52	128.45
4	123.81	131.76	124.00	o
5	130.36	127.11	129.08	128.45
6	112.02	123.68	122.98	121.62
7	147.16	147.92	147.65	148.30
8	123.96	123.68	123.67	123.23
9	158.54	158.97	158.84	159.28
10	127.42	125.22	127.15	126.76
11	158.43	158.36	158.30	158.14
12	111.57	111.07	110.90	110.36
13	161.04	161.11	161.09	161.19
13’	160.00	160.05	160.02	160.10
14	43.5	43.56	43.54	43.51
14’	43.04	43.02	43.04	42.97
15	12.42	12.45	12.44	12.46
16	178.83	178.79	178.78	178.75